Wall-normal pores for turbulent drag reduction

Experimental investigation into drag performance and flow mechanics

Sahana Jawahar

Wall-normal pores for turbulent drag reduction

Experimental investigation into drag performance and flow mechanics

Master of Science Thesis

by

Sahana Jawahar

in partial fulfilment of the requirements for the degree of

Master of Science
in Aerospace Engineering

at the Delft University of Technology

To be defended on Monday December 12, 2022 at 09:30

Student number:	5029880	
Thesis committee:	Dr. ir. B. W. (Bas) van Oudheusden	Delft University of Technology
	Dr. ir. F. F. J. (Ferry) Schrijer	Delft University of Technology
	Dr. F. (Francesco) Avallone	Delft University of Technology
	Ir. M. (Michiel) van Nesselrooij	Dimple Aerospace B.V.
	Dr. D. (Davide) Modesti	Delft University of Technology

This thesis is confidential and cannot be made public until 12/12/2024
At which point, an electronic version will be available at http://repository.tudelft.nl/.

Delft University of Technology

Faculty of Aerospace Engineering
Department of Aerodynamics, Wind Energy, Flight Performance and Propulsion

The undersigned hereby certify that they have read and recommend to the Faculty of Aerospace Engineering for acceptance the thesis entitled by **Sahana Jawahar** in partial fulfilment of the requirements for the degree of **Master of Science** in **Aerospace Engineering**.

Dated: December 12, 2022

Chair of supervisory committee:

Dr. ir. B. W. (Bas) van Oudheusden

Thesis committee:

Dr. ir. F. F. J. (Ferry) Schrijer

Dr. F. (Francesco) Avallone

Ir. M. (Michiel) van Nesselrooij

Dr. D. (Davide) Modesti

Preface

With this thesis, my time as a master's student at Delft University of Technology comes to an end. The past couple of years has been a wonderful journey with many learning experiences.

Firstly, I would like to thank Michiel van Nesselrooij, my supervisor from Dimple Aerospace. He has been very approachable and his inputs have been very valuable in shaping this thesis. I thank Olaf van Campenhout for his support and enthusiasm which has been very inspiring. I am grateful to Friso Hartog for his help with the PIV experiments and data processing.

I am grateful towards Dr. Bas van Oudheusden and Dr. Ferdinand Schrijer for their academic counsel. Their in-depth knowledge of various concepts in aerodynamics and expertise in experimental work have been valuable for this work. I would also like to thank all the staff and technical engineers both at the High Speed and Low Speed Laboratories who have supported me during my experimental campaigns.

I would like to thank the entire Dimple team for making my thesis experience an enjoyable one. Whether it was conducting wind tunnel experiments together and discussing about our theses or having fun conversations over lunch and coffee breaks, I have learned a lot of things from my fellow students. Finally, I am grateful for my family and friends who have been my greatest pillars of strength.

Sahana Jawahar
Delft, 29th of November 2022

Abstract

Flat surfaces with arrays of wall-normal pores called micro-cavity arrays have shown potential to reduce turbulent skin friction drag. Their designs have been inspired by acoustic liners which are sandwich panels consisting of a honeycomb core, a perforated top plate and a solid back sheet used on aircraft engine nacelles for noise abatement. Research on acoustic liners has paved the way to identify the parameters that are crucial for optimising the design of micro-cavity arrays. Spanwise rectangular grooves, a special case of cavities, have also shown potential to reduce skin friction drag in studies by Tani et al. (1988) and Coustols and Savill (1992). In this research, experimental results show that although pores and grooves are capable of reducing the turbulence energy in the boundary layer, there is a significant drag increase with respect to a smooth reference.

Micro-cavity arrays designed with pore diameter and spacings in the order of the coherent structures reduce turbulence energy in the near-wall region of the turbulent boundary layer (Silvestri et al., 2017a). Through computational and experimental studies conducted by Bhat et al. (2021), Gowree et al. (2019) and Scarano et al. (2021), skin friction drag reductions of 5.6%, 10% and 12% were reported. Several hypotheses for the drag-reducing mechanism have been proposed but a consensus is yet to be reached. This thesis aims to validate the reported drag performance of micro-cavity arrays and grooves through experimental methods used in literature and direct force measurements. Additionally, new designs were explored to determine an optimum drag-reducing micro-cavity array and groove. Twenty test plates were manufactured for this purpose and tested in the wind tunnel. Direct force measurements were performed to study the drag performance and particle image velocimetry measurements and hot-wire anemometry to study the influence of pores on the turbulent boundary layer.

All test plates produced a higher drag than a smooth reference plate, $0.5\,\% < \Delta C_D < 8\,\%$. The drag values did not match with literature but overall trends were found to correlate with existing design guidelines. Flow field measurements showed that some designs reduced the turbulence energy of the boundary layer however this did not match the estimated skin friction coefficient. By applying the Variable Interval Time Averaging (VITA) technique (Blackwelder and Kaplan, 1976), it was found that shifts in turbulence intensities correlated with the occurrence of burst events. Perforated plates with backing cavities were shown to experience a wall-blowing action which is responsible for the drag increase. These results contradict the drag-reducing theory proposed by Bhat et al. (2021) that wall-normal flow interactions damp the turbulence intensities in the near-wall region. The plates with grooves experienced a drag increase while one groove design was shown to reduce the turbulent energy in the boundary layer.

Based on the drag trends obtained in this work and past research on cavity flows, it has been argued that the observed drag increase is caused by pressure forces acting on the inner walls of the pores and grooves. As past research on micro-cavity arrays did not perform direct force measurements, the contribution of pressure drag has not been investigated. Pressure drag is expected to be present and perhaps even dominate over the reported skin friction drag reductions. Further research into the flow mechanics inside the pores is required to validate this argument and find a way of minimising the pressure forces. Wall-normal pores could still be an effective turbulent drag reduction technique if arrays are optimised for skin friction drag reductions that surpass pressure drag.

Table of Contents

List of Figures

List of Tables

Nomenclature

Acronyms and Abbreviations

AE	Aerospace Engineering
BL	Boundary layer
CC	Cross-correlation
CNC	Computer Numerical Control
DEMO	Dienst Elektronische en Mechanische Ontwikkeling
DFM	Direct force measurement
DNS	Direct numerical simulation
FOV	Field of view
HWA	Hot-wire anemometry
IATA	International Air Transport Association
KH	Kelvin-Helmholtz
LSL	Low Speed Laboratory
PIV	Particle image velocimetry
PTU	Programmable timing unit
px	Pixels
rms	Root mean square
RMSE	Root-mean-square error
RPM	Rotations per minute
S	Station (streamwise location) in PIV experiments (e.g. S1 denotes station 1)
TBL	Turbulent boundary layer
TE	Trailing edge
TU Delft	Delft University of Technology
WT	Wind tunnel

Dimensionless Groups

C_D	Drag coefficient based on freestream flow conditions and test plate top area
C_f	Skin friction coefficient
Re	Reynolds number
Re_1	Reynolds number based on unit length (unit Reynolds number)
Re_δ	Reynolds number based on boundary layer thickness
Re_τ	Reynolds number based on wall shear stress (friction Reynolds number)
Re_θ	Reynolds number based on momentum thickness
Re_x	Reynolds number based on streamwise distance from boundary layer starting point

Greek Symbols

Δ	Difference
δ	Boundary layer thickness
δ^*	Displacement thickness
δ_v	Viscous length scale
κ	von Kármán constant
μ	Dynamic viscosity
ν	Kinematic viscosity
ρ	Density
τ	Shear stress
τ_w	Wall shear stress

Latin Symbols

A	Area
B	Turbulent boundary layer wall law intercept constant
D	Diameter
d	depth
F	Force
$f\#$	F-stop
F_p	Pressure force
F_{null}	Null force
H	Height, shape factor
L	Characteristic length scale, length

L_x	Streamwise pore spacing
L_z	Spanwise pore spacing
N	Number of samples
P	Pressure
p_a	Absolute pressure
q	Dynamic pressure
R_{xy}	Reynolds stress
S	Surface area
u, v, w	Velocity in streamwise, wall-normal and spanwise directions
u', v', w'	Velocity fluctuation in streamwise, wall-normal and spanwise directions
U_∞	Freestream velocity
w	Width
x, y, z	Coordinates in streamwise, wall-normal and spanwise directions
x_{TP}	Streamwise distance w.r.t. test plate leading edge

Superscripts

$+$	Expressed in viscous units

1

Introduction

Aerodynamic research is focused on reducing the fuel consumption of aircraft to reduce the CO_2 emissions of the aviation industry. As the amount of fuel consumed by an aircraft is directly related to the amount of drag it has to overcome, the most obvious approach is to reduce this drag. This thesis investigates a passive method to reduce the turbulent drag experienced by an aircraft. This chapter provides an introduction to some basic concepts that are relevant to the current topic of interest. The relevance of turbulent skin friction in the aviation industry is discussed in Section 1.1 and a brief introduction to flow control is presented in Section 1.2. The research objectives and questions of the thesis are presented in Section 1.3 and Section 1.4. Finally, Section 1.5 gives the structure of this report.

1.1. Role of turbulent skin friction in the aviation industry

The aviation industry is one of the fastest-growing in the transportation sector. Air traffic has been estimated to grow at 4.3% per annum with the number of operational passenger and cargo aircraft to double by 2038 (Airbus, 2019). Aircraft substantially depend on fossil fuels for energy consumption and a significant amount of this energy is utilised in overcoming drag. Studies show that transportation is responsible for one-fifth of the global CO_2 emissions with aviation contributing to about 2.5% of the CO_2 emissions. Apart from CO_2 emissions, the overall impact of aviation on climate change and global warming is estimated to be 3.5% (Lee et al., 2021). Although the COVID-19 pandemic heavily impacted air transport causing an estimated net loss of $ 126.4 billion to the industry in 2020 (IATA, 2021a), the positive effect was the reduction in CO_2 emissions. According to the statistics presented in Figure 1.1, there was about a 50% decline in CO_2 emissions in 2020 and an increase of 52 million metric tons the following year as air travel resumed in several places. As travel restrictions were scraped and countries opened their borders to foreign travellers, air travel increased in 2022 and as a result the amount of CO_2 emissions.

Due to the increased concerns about climate change, various countries and organizations are in collaborating to tackle this problem. The International Air Transport Association (IATA) has devised a roadmap to improve aircraft fuel efficiency and reduce 50% of net aviation carbon emissions by 2050 (IATA, 2013). The European Union has an intermediate goal of reducing greenhouse emissions by 55% by 2030. In accordance with this, TU Delft is participating in the "Smart and Sustainable" plan of the Dutch aviation industry that aims to reduce CO_2 emissions by 35% by 2030. As turbulent friction drag accounts for 50% of energy consumption, focusing on novel techniques to overcome this is highly essential. This thesis aims to investigate the potential of a recently proposed passive method to reduce turbulent energy.

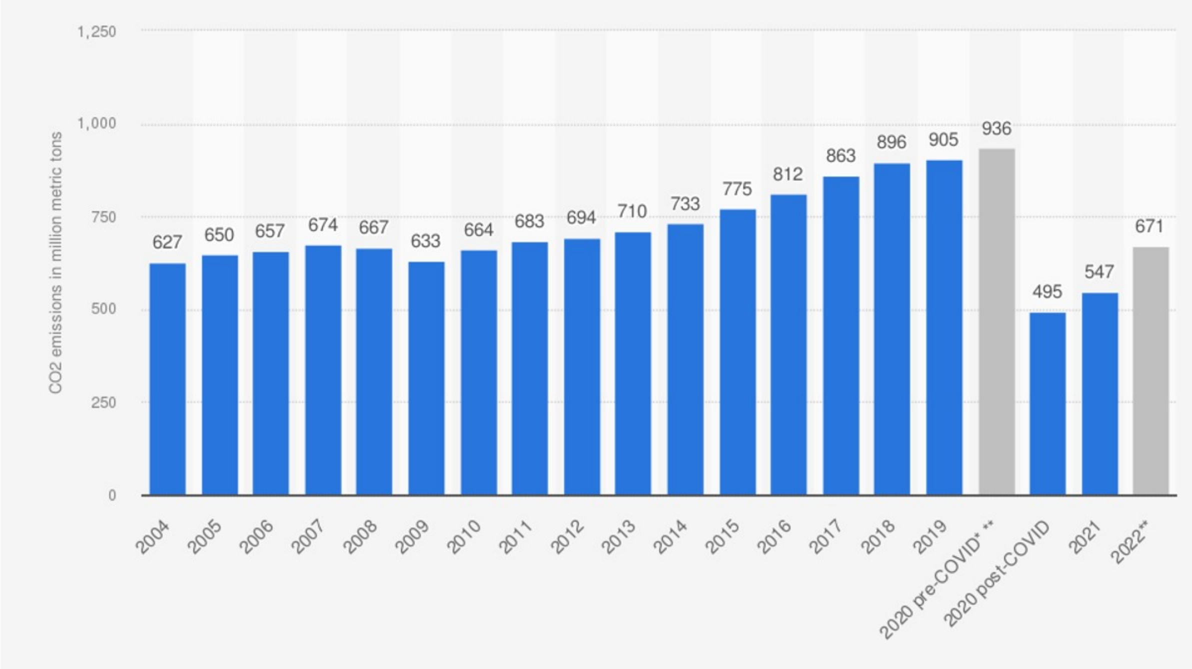

Figure 1.1: Carbon dioxide emissions by global commercial aviation (IATA, 2021b)

1.2. Introduction to flow control

Turbulent drag reduction can be achieved by manipulating the behaviour of the boundary layer of a fluid flow. This is referred to as flow control. The pioneer in flow control was Prandtl (1904), who introduced the concept of boundary layers and experimented with active techniques to control them. He demonstrated the use of suction to delay boundary layer separation on the surface of a cylinder. Research on flow control accelerated in the 20th century owing to military needs during Second World War and Cold War to develop fast and efficient aircraft. Subsequently, the oil crisis in the 70s and concerns about climate change that began in the 90s led to the development of novel techniques to reduce turbulent skin-friction drag.

Gad-el-Hak (2006) categorised the classification of flow control methods into three primary schemes. The first scheme is based on the location of application of control, either at the wall for example roughness, compliance, porosity and temperature or away from the wall using acoustic waves, additives, magnetic or electromagnetic forces and devices that disrupt large eddies. The second scheme is based on the expenditure of energy and is classified into active and passive methods. The final scheme is based on whether the control techniques modify the velocity profile or disrupt the small-scale eddies present in wall-bounded flows.

The classification based on energy expenditure is the most common scheme. Active control requires auxiliary power and a control loop and examples of such methods are synthetic jets, plasma actuators, blowing/suction, wall-heating, oscillating walls and movements of surface elements. These methods are capable of modifying flow in a controlled manner and at specific locations. This is advantageous for the control of turbulent flows which have a chaotic behaviour (Oktay and Kanat, 2017). Computational studies performed by various research groups in the 1990s showed that active systems can reduce about 20-70% of turbulent drag with maximum reduction obtained using tangential blowing (Anders et al., 2004). However, in reality, there are several limitations on the components of the control mechanism such as sensors and actuators that reduces its efficacy.

Passive control, on the other hand, does not require external power for its operation and has a relatively simple construction that is easy to maintain. Some passive techniques include vortex generators, riblets, patterned surfaces like dimples, surface roughness, porous surfaces, Large-eddy breakup devices (LEBUs), wavy walls and compliant coatings. These techniques are being researched for turbulent drag reduction and a review of the drag reduction potential, cost, maintenance and implementation of each technique is provided by Lai (2020). The scope of this thesis is to investigate one such passive technique, the wall-normal pores. An organised arrangement of wall-normal pores with fixed geometrical parameters forms a micro-cavity array. In this work, various configurations of micro-cavity arrays designed based on the outcomes of a literature study that preceded the thesis were experimentally analysed through wind tunnel tests.

1.3. Research objectives

The main research objective of this thesis is:

> "To experimentally investigate the potential of wall-normal pores on the surface of a flat plate to reduce turbulent drag, by conducting direct force measurements, hot-wire measurements and flow visualization on flat plates with pores of different dimensions and configurations placed in turbulent airflow."

To achieve the main objective of the project, the following sub-objectives have been defined:

1. Validate existing results by producing test plates with pore designs available in literature and testing them in the wind tunnel.
2. Explore the design space of micro-perforated plates by conducting a parametric study that includes variations in pore dimensions, spacings, configurations and backing cavity designs.
3. Evaluate the potential of grooves to reduce turbulent drag by recreating drag-reducing groove designs from literature and testing their drag performance.
4. Improve understanding of turbulent flow behaviour over pores by performing flow visualisation measurements.

1.4. Research questions

To fulfil the sub-objectives, the following research questions (RQ) have been formulated:

RQ1: How does the performance of reproduced micro-perforated plates compare with existing results?

- (a) What is the drag performance of micro-perforated plates? How does it compare with the drag values reported in literature?
- (b) How is the turbulent energy in the boundary layer affected in comparison to a smooth flat plate? Does literature report similar changes in turbulent energy?
- (c) Can differences in measured and existing results, if observed, be explained?

RQ2: How do the design parameters related to micro-perforated arrays and backing cavities affect their performance?

- (a) What effect does pore diameter, depth and spanwise and streamwise spacing have on the drag performance of a flat plate? To what extent do these parameters modify the energy content of the turbulent boundary layer and how does it correlate with drag performance?
- (b) Does pore configuration (aligned vs staggered) influence drag performance and turbulent intensity levels?
- (c) Do backing cavities modify the performance of a perforated plate? What effect do the size and alignment of the cavities have on drag behaviour?

RQ3: Can the drag-reducing potential of spanwise grooves with square cross-sections be validated?

- (a) What is the drag performance of spanwise grooves with square cross-sections? How does it compare with existing results?
- (b) Does the drag behaviour correlate with that of perforated plates?
- (c) How do grooves influence the turbulent energy of the flow?

RQ4: Are the current flow characterisation techniques sufficient for determining the mechanism behind drag behaviour?

- (a) To what extent do boundary layer profiles provide information on the working mechanism of pores?
- (b) Does a qualitative analysis of the turbulent structures explain the near-wall flow phenomenon?

1.5. Report overview

This report aims to achieve the objectives presented in Section 1.3 by answering the research questions posed in Section 1.4. Chapter 2 presents the literature review that covers the background of the work done in this thesis. Some fundamental concepts of the turbulent boundary layer is covered followed by an overview of past research performed on micro-perforated plates. Chapter 3 covers the methodology of the experimental campaigns. The rationale for the micro-cavity array designs and steps for the production of the test plates are given. This chapter also covers the setup, plan and processing routines of the direct force measurements and PIV experiments. Chapter 4 presents the results of the experiments. The drag performance of the test plates and the characteristics of the turbulent boundary layer over the cavity arrays are covered. Chapter 5 presents an overarching discussion of the experimental results. Finally, Chapter 6 sums up the conclusions of the thesis and the recommendations for future work. Supporting material can be found in the appendices at the end of the report.

2

Literature Review

2.1. Boundary layer theory

The boundary layer is a thin region of viscous flow formed at a fluid-wall interface in which the tangential velocity changes from zero at the wall to the freestream value in the wall-normal direction. The zero velocity at the wall is imposed by the no-slip condition. The boundary layer is categorised as laminar or turbulent based on flow conditions. The development of a boundary layer over a flat plate in the absence of a pressure gradient is demonstrated in Figure 2.1. At the leading edge of the flat plate, the boundary layer is laminar and after a distance along the streamwise direction (x) transitions to turbulent. Although transition occurs over a finite length, it is assumed that it occurs suddenly at a particular point. The transition point can be determined by the critical Reynolds number, whose exact value depends on several factors like surface roughness, flow disturbances, vibration, sound, pressure gradients, etc. For the flat plate at zero pressure gradient, the critical Reynolds number is estimated to be 5×10^5 (Schlichting and Kestin, 1961).

In the practical world, most flows are predominantly turbulent. White (2006) has described turbulence as a spatially varying mean flow that has been superimposed with self-sustaining three-dimensional random fluctuations with the ability to enhance mixing, dissipation, diffusion and entrainment. High Reynolds number turbulent flows are said to possess a boundary layer character similar to laminar flows where the flow field consists of an outer inviscid flow and a thin region close to the wall consisting of a turbulent boundary layer. In a turbulent boundary layer, exchange of mass, momentum and energy occurs across the several layers contained in it leading to mixing on a macroscopic scale. Therefore, for a turbulent boundary layer, the velocity gradient close to the wall is larger compared to a laminar boundary layer resulting in higher shear stress.

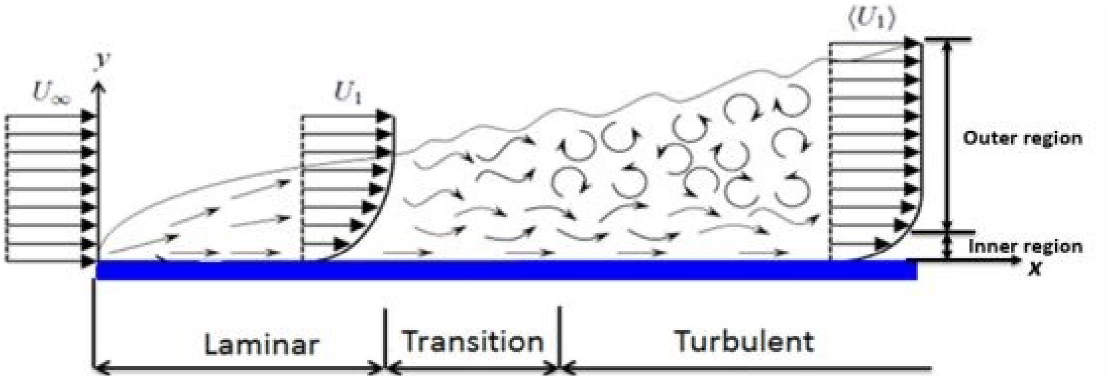

Figure 2.1: Boundary layer development over a flat plate (Alhamdi, 2018)

2.1.1. Characteristics of the boundary layer

Applying the integral conservation laws of mass and momentum to the boundary layer yields the integral-momentum equation. It was first derived by Kármán (1921) and is used to quantify the evolution of the boundary layer. The integral-momentum equation provides a relationship between the boundary layer characteristics, wall shear stress and friction coefficient as shown below,

$$\frac{d\theta}{dx} + (2+H)\frac{\theta}{U_e}\frac{dU_e}{dx} = \frac{\tau_w}{\rho U_e^2} = \frac{C_f}{2} \tag{2.1}$$

where θ is the momentum thickness, H the momentum shape factor, τ_w the wall shear stress and C_f the friction coefficient. The equations for these quantities are given as follows,

$$\theta = \int_0^\infty \frac{\vec{u}}{U_e}\left(1-\frac{\vec{u}}{U_e}\right)dy \tag{2.2}$$

$$H = \frac{\delta^*}{\theta} \tag{2.3}$$

where δ^* is the displacement thickness calculated as

$$\delta^* = \int_0^\infty \left(1-\frac{\vec{u}}{U_e}\right)dy \tag{2.4}$$

When the pressure gradient over the flat plate is considered to be zero, Equation (2.1) is simplified as

$$C_f = 2\frac{d\theta}{dx} \tag{2.5}$$

2.1.2. Structure of the turbulent boundary layer

The turbulent boundary layer primarily consists of two layers: an inner layer close to the wall where viscosity effects dominate, and an outer layer where turbulent effects dominate. An intermediate region called the overlap layer smoothly connects these two layers. In the inner layer, the velocity profile depends on the near-wall conditions like the shear stress, wall-normal distance and fluid properties but not directly on the freestream parameters apart from the net influence of the wall-shear. Conversely, in the outer layer, flow depends on the freestream conditions with the wall conditions merely acting as a source of flow retardation (White, 2006). The scaling parameters that are relevant to the inner region are friction velocity $u_\tau = \sqrt{\frac{\tau}{\rho}}$ and kinematic viscosity ν. Using these parameters the velocity and wall-normal distance are non-dimensionalised as follows,

$$u^+ \equiv \frac{\vec{u}}{u_\tau} \tag{2.6}$$

$$y^+ \equiv \frac{y u_\tau}{\nu} \tag{2.7}$$

The inner layer is further subdivided into three regions:

1. **Viscous sublayer**: $y^+ \leq 5$
   In this very thin region near the wall, the velocity profile is linear, $u^+ = y^+$

2. **Buffer layer**: $5 \leq y^+ \leq 30$
   In this region, the velocity profile is a merge between linear and logarithmic. Most of the turbulence production that occurs in the entire boundary layer is said to occur in the buffer layer (Robinson (1991)).

3. **Logarithmic or overlap layer**: $y^+ \geq 30$
   In the overlap layer, the laws pertaining to the inner and outer layers, defined as the law of the wall and defect law respectively, are both valid. This leads to a logarithmic distribution of the mean streamwise velocity as follows,

   $$u^+ = \frac{1}{\kappa}\ln y^+ + B \tag{2.8}$$

   where $\kappa \approx 0.4$ is the von Karman constant whose value depends on the properties of the overlap layer and B depends on the no-slip boundary condition. For smooth walls B $\approx$ 5.0.

2.2. Coherent Structures

In the earlier days, turbulent flows were considered to be a random phenomenon with chaotic motions. However, in the second half of the 20th century, there were findings of unsteady repetitive structures that led to the discovery of coherent structures. Hussain (1986) has defined coherent structures based on an ensemble average of the turbulent shear flow. According to his definition, a coherent structure is the *"ensemble average of phase-aligned realizations that contain similar organised events"* and the remaining is incoherent turbulence. These coherent structures are not considered to have a specific geometry or temporal periodicity but are described as quasi-regular structures. They influence the mean and fluctuating components of the velocity field thereby contributing significantly to the production of turbulence energy and Reynolds stress (Hunt, 1987). An extensive experimental study including various flow visualisation techniques like smoke, dye and bubbles has been used to study the coherent structures in turbulent flows.

2.2.1. Burst-sweep cycle

Visual studies using bubbles performed by Kline et al. (1967) revealed the presence of streaks that were formed by the streamwise component of vorticity in the viscous sublayer. These streaks are alternating regions of high and low-speed fluid with an average spanwise spacing of 100 viscous lengths (Kline et al., 1967) moving in the direction of the mean flow. The low-speed regions of fluid, known as the low-speed streaks interact with the outer regions leading to a series of events called the burst-sweep cycle as shown in Figure 2.2. Studies using dye injection showed that this cycle occurs randomly over the surface at intermittent intervals.

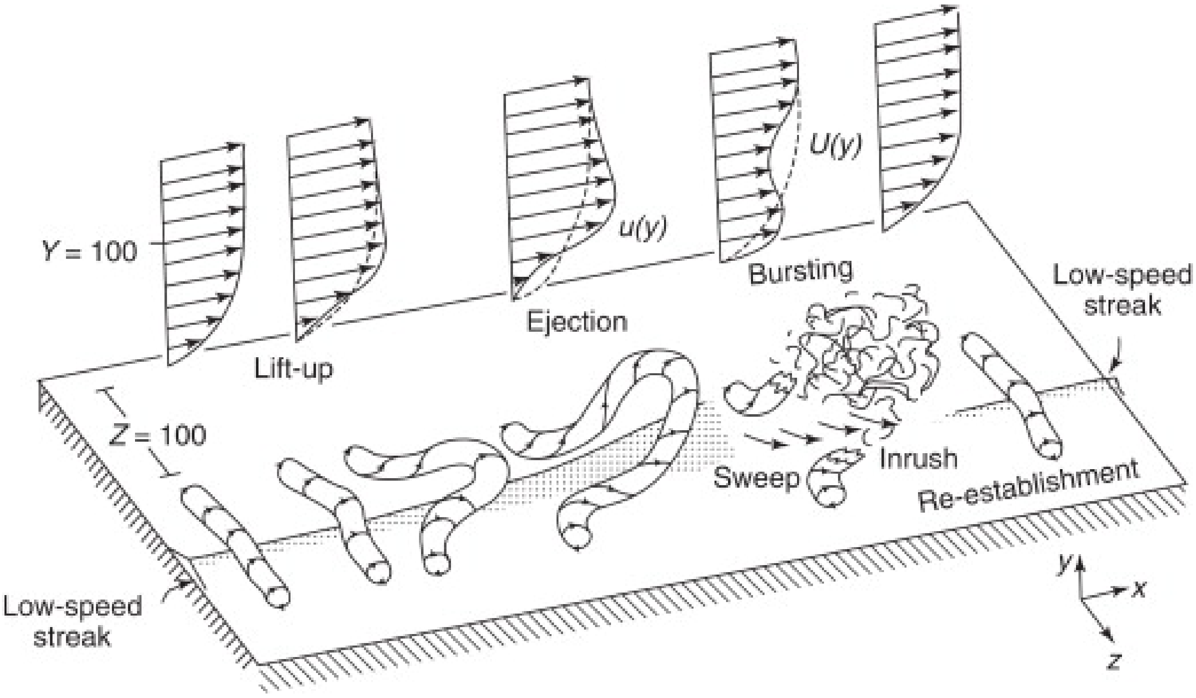

Figure 2.2: Schematic of the burst-sweep cycle (Allen, 2009)

As the low-speed streaks move along the streamwise direction, they are lifted up and form hairpin vortices which eventually break down resulting in turbulence. The transport of the low-speed streaks away from the wall to the outer wake region by means of violent ejections are called bursts. The bursting process plays a significant role in the exchange of momentum between the inner and outer regions of the boundary layer. Kline et al. (1967) identified that in the viscous sublayer the streaks are smooth and as they move outward into the buffer layer at $y^+ \approx 8-12$, oscillations are induced. These oscillations have been observed by Corino and Brodkey (1969) as the beginning of an ejection event that moves outward from the surface of the wall. Ejections violently interact with the outer high momentum fluid resulting in turbulent motion that is disorganised and abrupt. Studies have thus concluded that ejections are highly energetic events that lead to the production of turbulent energy. While Corino and Brodkey (1969) suggests that turbulent energy is generated and dissipated in the region $5 \le y^+ \le 70$, the interaction of the ejection with the higher velocity is said to take place at $7 \leq y^+ \leq 30$. This is the buffer region where Kline et al. (1967) suggested the bursting of the streaks occurs. Bursting is followed by the movement of high momentum fluid from the surface of the boundary layer to the near-wall region by high-speed vortices called sweeps. The sweep event results in the acceleration of fluid near the wall increasing wall shear.

The ejection and sweep events are thus major contributors to shear stress. While Corino and Brodkey (1969) estimated that ejections contribute to 70% of the total shear stress and sweeps the remaining 30%, Wallace et al. (1972) has estimated that both events contribute almost equally to turbulent energy in the generation region. Wallace et al. (1972) and Lu and Willmarth (1973) showed that two more events namely outward and inward interactions, affected the shear stress of the near-wall region. A four-quadrant system was introduced by Lu and Willmarth (1973) to categorise the events. Ejections and sweeps are denoted as Q2 and Q4 events respectively and outward and inward interactions are labelled as Q1 and Q3 events. In the new study, ejections and sweeps are each estimated to contribute 70% of the total stresses and Q1 and Q3 events which result due to the interaction between the sweep and ejection events are estimated to make a negative contribution of 40%. As the occurrence of sweeps and ejections is dependent on each other, modifying one of them will significantly affect the other. Therefore, several research groups are focused on achieving turbulent drag reduction by altering these events.

2.3. Passive flow control using wall-normal pores

Recent studies by Silvestri et al. (2017a) and Gowree et al. (2019) have reported the potential of an array of wall-normal pores to reduce skin friction drag. Although this passive technique is promising the net drag produced by micro-perforated plates is unexplored and will be investigated in this thesis. This section presents an overview of the existing research on passive flow control using wall-normal pores.

Section 2.3.1 briefly discusses about Helmholtz resonators followed by a comprehensive discussion on perforated plates in Section 2.3.2. The drag-defining parameters are explored in detail in Section 2.4 and the several hypotheses for the working mechanisms of wall-normal pores are discussed in Section 2.5. Finally, Section 2.6 gives the concluding remarks on this topic.

2.3.1. Flow control using Helmholtz resonators

The precursors of wall-normal pores are Helmholtz resonators. They are considered passive flow control devices as they reduce turbulent energy production in turbulent boundary layers (Ghanadi et al., 2014a,b, 2015). The resonator consists of a circular orifice backed by a cavity containing a fixed volume of fluid, in this case, air. The behaviour of the shear layer over the orifice is responsible for the excitation of the device. Figure 2.3a shows a diagrammatic representation of how the behaviour of the shear layer influences the flow inside the Helmholtz resonator. The shear layer travelling from the leading edge of the orifice breaks into quasi-periodic vortices as it reaches the trailing edge. On interaction with the trailing edge, these vortices produce pressure waves which propagate back towards the leading edge. When this pressure wave oscillation couples with the fluid in the cavity, a mass and spring-like oscillation occurs resulting in suction and blowing action. Thus, the passively activated resonator changes the near-wall structures in the flow over the orifice and to some distance downstream of the resonator.

Geometrical parameters such as cavity depth and orifice diameter have been shown to have a significant effect on the excitation of the resonator which in turn affects the behaviour of the turbulent boundary layer. Panton and Miller (1975) observed through experiments that a strong excitation of the resonator occurs when the size of the eddies in a turbulent boundary layer is twice that of the orifice diameter. Ghanadi et al. (2014a) performed experiments with 12 different cylindrical Helmholtz resonators and concluded that resonators with the largest cavity depth (L/D=4) produce the largest pressure fluctuations inside the resonator which is very close to resonance. The pressure inside the resonator has also been observed to increase as the boundary layer thickness approaches the orifice diameter. The high-amplitude pressure fluctuations affect the stability of the turbulent boundary layer. Ghanadi et al. (2014b) showed that at a low Reynolds number, two Helmholtz resonators HR2 and HR4 as shown in Figure 2.3b were capable of controlling the turbulent boundary layer.

When the orifice diameter was approximately equal to the thickness of the inner layer $d \approx 0.2\delta$ (HR2), the velocity fluctuations downstream of the orifice reduced by 16%, sweep intensity reduced by 11% and sweep duration by 5%. Additionally, when the orifice length was approximately equal to boundary layer thickness (HR4), a 12% reduction in streamwise velocity fluctuations was observed at the downstream location and a 5% reduction in sweep intensity at y^+=35.

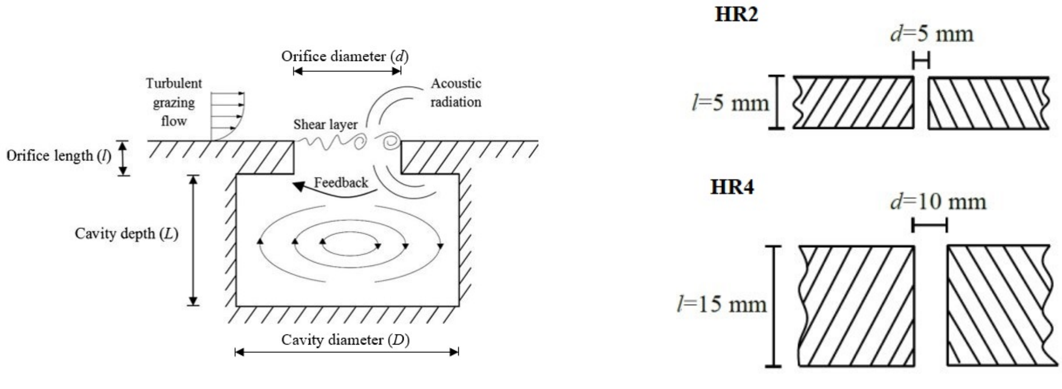

(a) (b)

Figure 2.3: (a) Representation of the working principle of a Helmholtz resonator (Ghanadi et al., 2014a) (b) Resonator orifice configurations that were shown to effectively control the turbulent boundary layer (Silvestri, 2018)

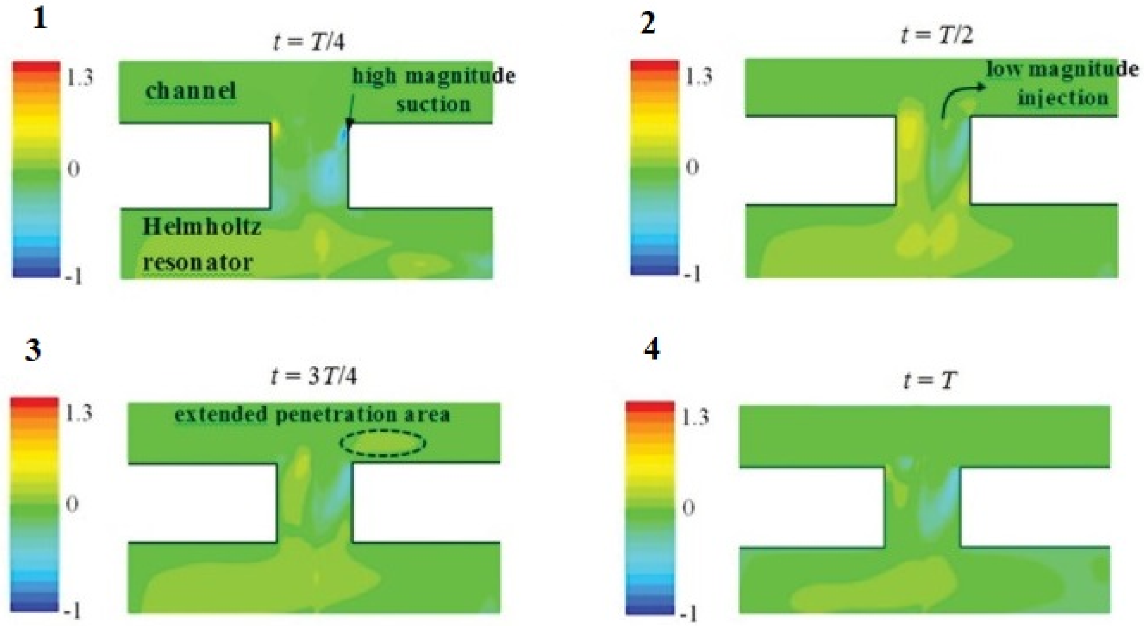

Figure 2.4: Wall-normal velocity fluctuations over the orifice of HR2 (Ghanadi et al., 2015)

Computational analysis of Helmholtz resonators was performed by Ghanadi et al. (2015) using Large-Eddy Simulation (LES). Downstream of the HR4 orifice, a 12% reduction in velocity fluctuations was observed. It was also shown that in the near-wall region, the energy of the turbulent eddies reduces leading to the suppression of boundary layer instabilities. The wall-normal velocity fluctuations in HR2 produce a suction and blowing action at the trailing edge of its orifice, which stabilises the boundary layer and extends up to two orifice diameters downstream of the orifice. This process can be visualised in Figure 2.4. From the experimental and computational analyses, it was concluded that Helmholtz resonators with an orifice length equal to the boundary layer thickness and orifice diameter of approximately half of the boundary layer thickness can be considered passive flow control devices. Furthermore, resonators were also observed to reduce turbulence energy in the near-wall region in the absence of a suction and blowing action. It has been theorized that the sweep events enter the orifice partially or wholly, which results in the dampening of turbulent energy. In this scenario, the Helmholtz resonator acts as a single cavity thus paving the way for the investigation of wall-normal pores as a potential passive flow control technique.

2.3.2. Flow control using perforated plates

Perforated plates have been investigated for decades for their capacity to absorb noise. Acoustic liners consisting of a combination of a perforated plate, honeycomb core and solid back sheet have been used on aircraft engines to reduce tonal noise. However, such liners are known to produce additional drag when compared to a smooth surface which has been tolerated to meet the necessary noise level requirements. A lot of research has therefore been focused on developing a liner that is capable of reducing noise while limiting drag increase as much as possible. Apart from acoustic liners, smooth surfaces with a localised array of micro-cavities have been studied for passive flow control. The following sections present several designs of perforated plates and the influence of design parameters on the surrounding flow.

Acoustic liners

While acoustic liners have been successfully used to reduce noise levels of aircraft propulsion systems, it has been achieved at the cost of drag increase. A conventional acoustic liner as shown in Figure 2.5a consists of a honeycomb core that is sandwiched between a perforated plate and a solid back sheet. Several studies have focused on determining the relationship between various design parameters and drag.

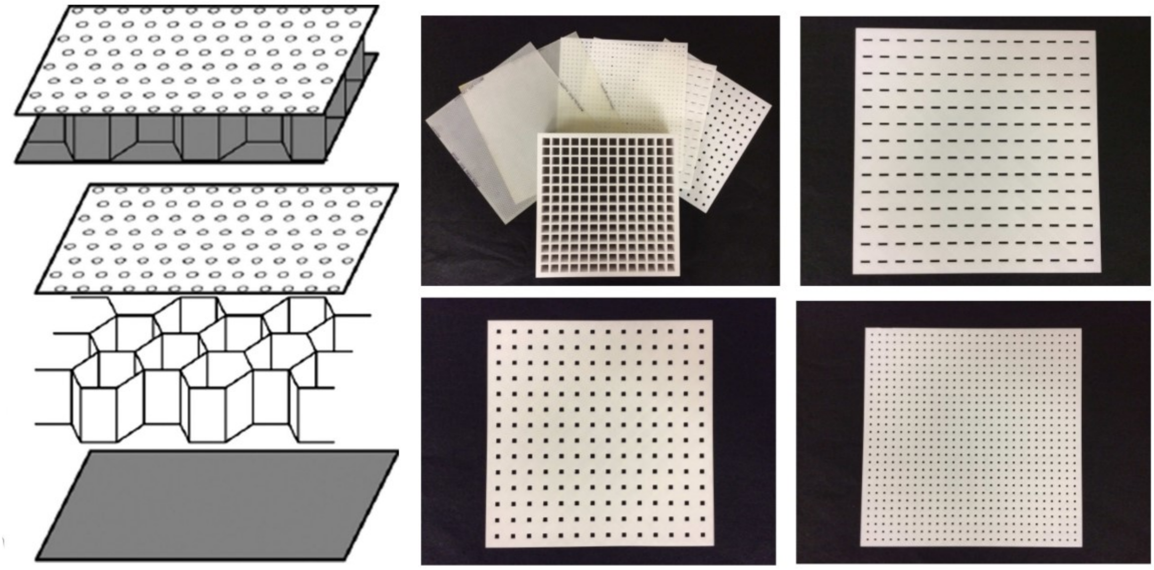
(a) (b)

Figure 2.5: (a) Schematic representation of a conventional acoustic liner (b) 3-D printed designs of perforated top plates with different hole shapes and dimensions (Jasinski and Corke, 2020)

Jasinski and Corke (2020) performed experiments with liners having different perforate designs to measure the drag produced by each design (Figure 2.5b). They observed that liners with perforations spaced less than 100 wall units in the spanwise direction when exposed to acoustic excitation, experienced a large increase in viscous drag. This result was in congruence with the results of Wilkinson (1983), who observed that liners with hole spacing less than 100 wall units showed the largest drag rise. The suggested mechanism for drag rise is the increase in the number of ejection events in the near-wall region in the presence of a large acoustic excitation. A comparison between the number of ejection events measured in the boundary layer over a perforated liner in the absence and presence of an acoustic excitation is shown in Figure 2.6. A dramatic increase in the number of ejections with acoustic excitation can be observed in the near-wall region. Measurements by Jasinski and Corke (2020) demonstrated an unsteady blowing action that emerged from the perforations and interacted with the wall streaks. These localised disturbances increased the frequency of bursts resulting in increased turbulent energy.

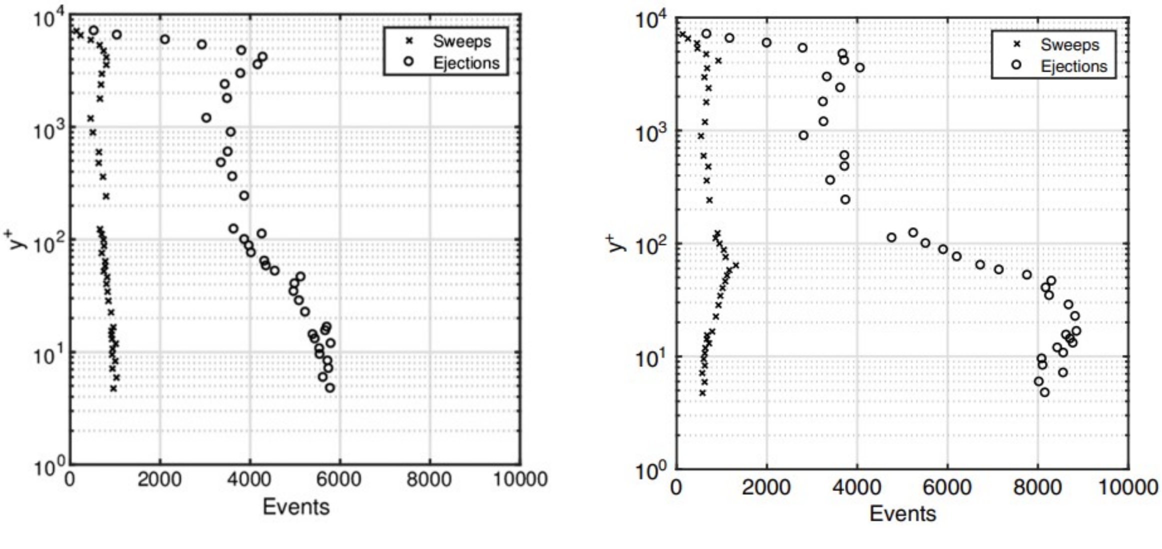

(a)

(b)

Figure 2.6: Number of sweep and ejection events in the boundary layer over a perforated liner (a) without acoustic excitation (b) with acoustic excitation (Jasinski and Corke, 2020)

Table 2.1 summarises the work of some of the other groups that have measured the drag performance of different liner designs. Perforated plates with holes of different dimensions, spacing and configuration have been tested using various measurement techniques and some common trends have been observed. While most researchers worked on liners with staggered holes, Wilkinson (1983) and Wolter (2005) made a comparative study between the inline and staggered configurations and reported that liners having staggered configuration perforations experienced lower drag than the inline configuration. The porosity of the perforated plate has been identified as a significant parameter that influences the drag performance of liners. Wilkinson (1983), Wolter (2005), Drouin et al. (2006) and Gerhold et al. (2016) observed an increase in drag with increasing porosity. Another parameter that is related to porosity is the size of the perforations. It has been reported by different groups that increasing hole diameter increases drag. The relationship between flow speed and drag performance is uncertain as results are inconsistent. Drouin et al. (2006) reported an increase in skin friction coefficient with increasing sound pressure level (SPL) regardless of the porosity or perforate size. This observation is in agreement with the results of Jasinski and Corke (2020). Overall, it has been noted that none of the designs presented here showed a potential to reduce drag however, the parameters that were responsible for reducing drag increase can be taken into account for future designs.

Table 2.1: An overview of designs and performances of acoustic liners

Study	**Pore diameter (mm)**	**Thickness to pore diameter, t/d**	**Percent Open Area, POA (%)**	**Configuration**	**Additional features**	**Measurement equipment**	**Testing conditions**	**Observations**
Boldman and Brinich (1976)	1.27	0.03	8	Staggered	Perforated plate was backed by a structure of hexagonal cells 9.5 cm in diameter by 6.4 cm deep and mounted on a solid plate	Pitot probe	M = 0.17, 0.35,0.62	3% more drag than the smooth wall at Mach 0.17 10% more drag at Mach 0.35 19% more drag at Mach 0.62
Wilkinson (1983)	1.68	0.48	6	Staggered	Honeycomb core with 12.7 mm depth	Drag balance, HWA	Free stream velocities: 10-40 m/s	Staggered configuration has the lowest drag Drag increases with increase in POA For 1,2,3: Drag increases slightly with increase in velocity. For 4, drag increases slightly at velocities below 15m/s and then remains constant up to 40m/s. Largest drag increases are observed for models with hole diameters and spacings less than 100 wall units.
	1.45	0.56	12	Staggered				
	0.28	0.64	4.7	Inline	Honeycomb core with 19.1 mm depth			
	0.46	0.65	13.9	Inline				
Wolter (2005)		0.4 to 1.0	20 to 40	Inline, Axial and Transverse stagger	Face sheet backed by bulk acoustic absorber	Force balance	M = 0.3, 0.5, 0.6, 0.7	Skin friction coefficient is higher for 40% porosity Inline configuration had slightly higher drag than staggered configuration for 40% porosity(only case tested)
Drouin et al. (2006)	0.508, 1.016, 1.27		7 and 9		Perforated panels with solid back sheets	Pitot static probe	M = 0.17, 0.3, 0.5	Mach number has only a small effect on skin friction coefficient Skin friction coefficient increase with increasing POA and increasing hole diameter Skin friction coefficient increases with increasing SPL
Howerton and Jones (2015)	0.5, 0.7, 1	2, 1.43, 1	8	Staggered	Facesheets were 3-D printed from photopolymer resin using a stereolithography (SLA) process, Metallic honeycomb core of depths 38.1 mm and 76.2 mm	Pressure transducers	M = 0.3, 0.5	Friction factor decreases with increasing Mach number Friction factor decreases with decreasing hole diameter Change in cavity depth has minimal effect on friction factor
Gerhold et al. (2016)	1	1	8.7	Staggered	Facesheet placed over a honeycomb core of 19.1 mm depth with a solid back sheet	Pressure probe	M = 0.3, 0.5	25% increase in drag compared to a smooth wall at M=0.3 (case 1) 21% drag increase at M=0.5 (case 1) At constant porosity, drag increases with increasing hole diameter At constant hole diameter, drag increase with increasing porosity At M=0.3, the liner without the core produces less drag than the liner with the honeycomb core however at M=0.5 it was vice-versa.
	1	1	12					
	2.4	0.416	12.8					
	1	1	12		Facesheet placed over a solid back sheet without a core			

Micro-cavity arrays

A micro-cavity array is an organised arrangement of wall-normal pores with fixed geometrical parameters. These include pore diameter, pore depth, spanwise and streamwise pore spacings, and pore alignment. To achieve turbulent boundary layer control, the dimensions of these parameters must correlate with the size of the coherent structures in the inner layer of the turbulent boundary layer. Low-speed streaks that have been formed by streamwise vorticity have an average spanwise spacing of 100 times the viscous length scale (Kline et al., 1967) and length up to 10 times the spanwise spacing (Blackwelder and Eckelmann, 1979). As discussed previously in Section 2.3.2, Wilkinson (1983) and Jasinski and Corke (2020) reported that liners with a spanwise hole spacing of less than 100 wall units experienced the largest drag. Thus, it is imperative that the geometry and spacing of the pores are optimized to effectively disrupt the coherent structures. Lockerby (2021), who studied the use of jet actuators for the control of turbulent boundary layers suggested that the orifice diameter for a circular jet should not be larger than 40 times the viscous length scale.

Based on the above design guidelines, (Silvestri et al., 2017a) developed cavity array 1 comprising of holes of 1.2mm diameter with a spanwise spacing of 3mm and streamwise spacing of 15mm. Two more cavity arrays with larger hole diameters and corresponding spacings were developed as shown in Figure 2.7a. Through experimental investigations, they observed that when the diameter of the pore is less than 30 wall units ($d^+ < 30$), there was no reduction in turbulence energy as the pores were too small to affect the coherent structures. Furthermore, pores with $d^+ > 105$ produced an increase in the turbulence energy due to the breaking of the shear layer while traversing over the pore. The maximum reduction in turbulence and sweep intensities were observed for the cavity array with $d^+ = 60$. Further experimental and computational analyses to investigate the potential of the micro-cavity array to reduce drag were performed with this hole size and corresponding spacings. In contrast to the results of Silvestri et al. (2017a), Scarano et al. (2022a) analysed cavities in a staggered configuration as shown in Figure 2.7b with d^+ ranging from 130 to 250 and spacing L^+ ranging from 587 to 1075 and reported local reductions in skin-friction drag.

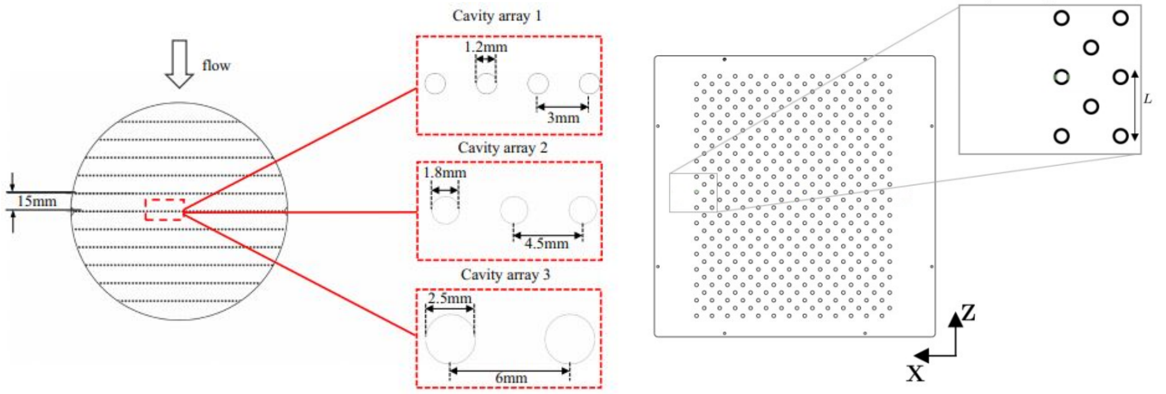

(a) (b)

Figure 2.7: Schematic designs of cavity arrays (a) Aligned cavity arrays of Silvestri et al. (2017a) (b) Staggered cavity array of Scarano et al. (2022a)

Earlier research groups analysed the performance of plates with micro-pores for noise reduction. Kong and Schetz (1982) and Wilkinson (1983) performed experiments on several designs with and without a backing core. Table 2.2 summarises the designs and results of plates with perforations without a backing core along with the findings of recent research groups that have focused on designing perforated plates for drag reduction. The micro-porous plates tested by Kong and Schetz (1982) and Wilkinson (1983) have shown an increase in skin friction drag. The increase in drag could be attributed to the design of the porous plates as they do not follow the guidelines. The remaining analyses were performed by two research groups with both reporting reductions in skin friction drag.

The first research group consisting of Silvestri et al, investigated plates with a localised micro-cavity array with and without a backing cavity. The experimental analyses showed that both cases were capable of reducing the turbulence energy in the turbulent boundary layer, with turbulence energy reduction increasing with increasing backing cavity volume. Bhat et al. (2021) performed a DNS study on the optimised cavity array design with a backing cavity and reported a 5.6% reduction in skin friction drag using the FIK identity (Fukagata et al., 2002).

On the other hand, the second research group consisting of Gowree and Scarano et al performed hot-wire measurements and estimated local reductions in skin friction drag. The amount of skin friction drag reduction for various design and flow conditions is listed in Table 2.2. In addition, flow visualisation studies and numerical analysis using explicit LES were performed by Gowree et al. (2019) and Scarano et al. (2021) respectively to visualise the flow field and the instabilities caused by the arrangement of the holes. A recent study by Scarano et al. (2022a) with hot-wire anemometry and Steoroscopic PIV showed the attenuation of burst intensity and increase in burst frequency in the near-wall region in the vicinity of the cavity array. However, it should be noted that neither of the research groups performed direct force measurements to determine the overall drag produced by perforated plates. Furthermore, the contribution of pressure drag has not been explicitly included.

Table 2.2: An overview of designs and performances of plates with wall-normal pores

Study	Pore diameters (mm)	Streamwise spacing (mm)	Spanwise spacing (mm)	Pore depth (mm)	Configuration	Additional features	Measurement techniques	Testing conditions	Observations
Kong and Schetz (1982)	0.15	0.625	0.625	0.625	Inline	None	Skin friction balance, rake of pitot tubes, HWA	Re_L (based on the length of the first station: 24.1 cm)= 4.96 x 10^6 to 6.11 x 10^6	30% increase in skin friction
Wilkinson (1983)	0.28	0.61	0.61	0.18	Inline	Single backing cavity with variable depth	Drag balance, Pitot tube, HWA	Free stream velocities: 10-40 m/s	Drag increases with increase in cavity depth
	0.46	0.76	0.76	0.3	Inline				
Silvestri et al. (2017a)	1.2 1.8 2.5	15	3 4.5 6	4	Inline	None	HWA	Re= 1195, 1927, 3771	Maximum of 13% Reduction in turbulence intensity(all, Re = 1297) Maximum of 14% reduction in sweep intensity (Array 2, Re = 1297)
Silvestri et al. (2017b)	1.2	15	3	4 2	Inline	Backing cavities with depths: 0, 5, 25, 50 mm	HWA	Re= 1927,2937, 3771	Orifice depth has negligible effect in modifying drag reduction performance Maximum 6.4% reduction in turbulence intensity (50mm , Re = 2939) Maximum 5.7% reduction in sweep intensities(50mm, Re = 3771)
Silvestri et al. (2018)	1.2	15	3	4	Inline	Backing cavities with and without a mesh	HWA	Re= 2939, 3771	Similar behaviour and results of flow control using cavities with and without mesh. Energy of the captured array is not redistributed across the orifices in the cavity array
Gowree et al. (2019)	2 to 5	20	20	3	Staggered	None	HWA, Surface flow visualization, LDA	Free stream velocities: 15, 20, 25 m/s	Maximum skin friction drag reduction of 10% for d/h<=1 when U=15m/s and cavities are sealed. Drag reduction extended over the whole span of the plate
Bhat et al. (2021)	1.2	15	3	4	Inline	Square cavities, Backing cavity of 46mm depth	DNS	Re =1960	5.6% reduction in skin friction drag Contribution due to inhomogeneity and pressure is less than 1%
Hoang et al. (2021)	1.2	15	3	4	Inline	Backing cavity of 50mm depth	HWA	Re= 3771	Reduction in burst amplitudes and durations, increase in burst frequency. Maximum reduction in burst at the near-wall region.
Scarano et al. (2021)	5	22	22	4	Staggered	For numerical analysis only three rows of cavities were used	HWA, Explicit LES	Free-stream velocity: 10, 15, 20 m/s	**Experimental:** 10m/s: skin friction drag reduction of 12% 15m/s: skin friction drag reduction of 7% 20m/s: skin friction drag increase of 13% **Numerical:** Spanwise velocity pattern and flow instability due to the interference of the first cavity with the second one.
Severino et al. (2022)	1	7.5	1.7	3, 6, 9, 12, 15	Inline	None	HWA	Re= 3282, 4651	All tested pore depths showed a reduction in turbulence intensity. Pore depth of 15mm showed the maximum reduction in turbulence intensity, sweep intensity and streamwise turbulent kinetic energy.
Scarano et al. (2022a)	5	22	22	4	Staggered	Bottom surface is sealed	HWA, Stereoscopic PIV	Free-stream velocity: 10, 15, 20 m/s	Increase in burst frequency and attenuation of burst intensity in the region 20<y+<80. Local reduction in skin friction drag with respect to a smooth reference.

2.3.3. Special case: Flow control using grooves

In the previous section, the flow control characteristics of an array of wall-normal pores were discussed. In this section, a special case of cavities which are grooves is explored. Grooves are cavities that are typically aligned in the spanwise or streamwise direction. Studies on spanwise aligned grooves have shown tendencies to both increase and decrease skin friction drag. At low Reynolds number, Tani et al. (1988) reported skin friction drag reduction up to 3% when the grooves were spaced at 10-20 times its width as shown in Figure 2.8a and Coustols and Savill (1992) reported 2% net skin friction reduction for grooves spaced 20 widths apart. Haugen and Dhanak (1966) reported that the ratio of groove depth to boundary layer thickness should be much smaller than 1 to achieve turbulent drag reduction over the groove.

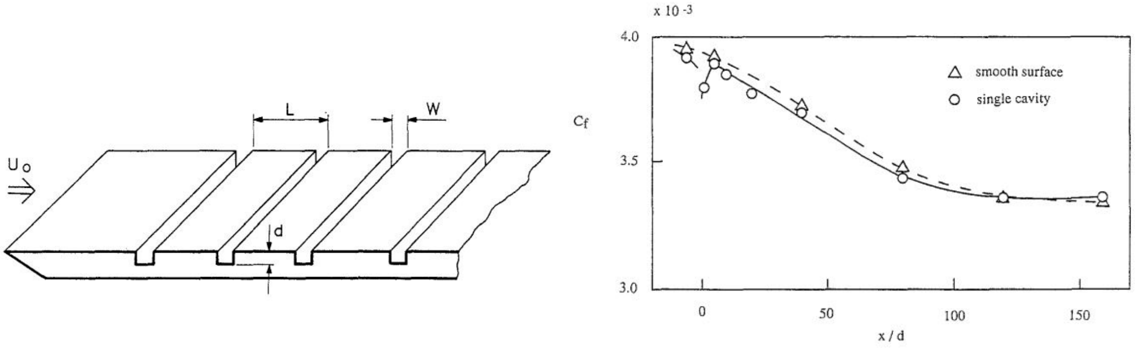

(a) (b)

Figure 2.8: (a) Schematic diagram of grooves (b) Variation of skin friction drag downstream of the cavity (Choi and Fujisawa, 1993)

Choi and Fujisawa (1993) conducted an experimental investigation of a single groove with a groove depth to boundary layer thickness of 0.4 and reported the variation of skin friction coefficient downstream of the cavity as shown in Figure 2.8b. The skin friction coefficient in the presence of a single square cavity was been observed to be less than a smooth surface for a distance of up to 120 x/d after which it increases slightly up to 150 x/d which is the maximum distance considered in this measurement. Considering the pressure to be negligible, the overall reduction in skin friction drag was estimated to be about 1%. However, it was also pointed out that the result should be considered with caution, as the order of error in the calculation of drag parameters is the same as the net drag reduction. The reduction in drag has been believed to be caused by a stable vortex present inside the cavity which absorbs the incoming turbulent flow and reorganises it. Furthermore, turbulence intensity profiles and mean velocity profiles in the near-wall region over the square cavity were observed to be similar to those present over riblets that reduce drag.

On the other hand, Elavarasan et al. (1995) reported a 3.4% drag increase when grooves were spaced 20 widths apart along with Wahidi et al. (2005) who consistently measured drag rise to about 5% for grooves with spacings ranging from 10 to 20 groove widths. Some studies have reported an oscillation in skin friction values downstream of a groove. A flow visualisation analysis conducted by Pearson et al. (1997) over a single groove showed an abrupt increase in skin friction drag at the trailing edge of the groove due to a localised intense favourable pressure gradient. This is followed by a sudden drop in value and then a slow retrieval of the original smooth plate value in an oscillatory manner. Similar observations were made by Sutardi and Ching (1999) and Wahidi et al. (2005). Pearson et al. (1997) also observed modifications in turbulent structures over the cavity as the fluid flowed in and out of the groove. The hypothesis formulated from this study was that the inflow and outflow temporarily stop activity in the near-wall region and the production of quasi-streamwise vortices which reduces the exchange of momentum, thereby leading to the drop in skin friction drag.

2.4. Parameters indicative of drag

To determine the effect of micro-cavities on a turbulent flow, it is useful to analyse the behaviour of certain properties of the boundary layer. Apart from direct drag measurements, estimation of skin friction drag and turbulence energy are achieved via parameters like mean velocity profile, turbulence intensity and sweep intensity. These parameters are elaborated below,

1. **Shift in mean velocity profile**

   Velocity data obtained from pitot tubes, hot-wire and PIV images within the turbulent boundary layer can be used to construct the streamwise boundary layer profiles. Friction velocity corresponding to each boundary layer profile is calculated using the logarithmic law expression as follows,

$$\frac{u^{'}}{u_\tau} = \frac{1}{\kappa} ln\left(\frac{y u_\tau}{\nu}\right) + B \tag{2.9}$$

   This is an iterative process wherein the value of friction velocity is varied until the logarithmic region of the experimental curve fits with the theoretical logarithmic law curve. With the value of friction velocity for each profile, the corresponding skin-friction coefficient can be estimated using the following expression,

$$\frac{u_\tau}{U} = \sqrt{\frac{C_f}{2}} \tag{2.10}$$

   Alternatively, the local skin friction over the cavity arrays can be determined using the Clauser (1956) plot technique with the following expression,

$$\frac{u'}{U} = \sqrt{\frac{C_f}{2}}\left(\frac{1}{\kappa} ln\left(\frac{yU}{\nu}.\sqrt{\frac{C_f}{2}}\right) + B\right) \tag{2.11}$$

   A comparison of mean velocity profiles between a smooth plate and surface-modified plates helps in identifying local skin friction drag behaviour Clauser (1954). Nikuradse et al. (1950) had observed that walls with a certain roughness produced a downward shift in the logarithmic profile with respect to a smooth wall, indicating an increase in local skin friction. Figure 2.9 presents the velocity profiles over perforated plates of various hole diameters that were measured using a hot-wire by Gowree et al. (2019) and Silvestri et al. (2017a) . It is evident from Figure 2.9a that there is a reduction in skin friction drag for the plate with 2mm holes in the viscous sublayer and logarithmic layer and for the plate with the 3mm holes in the logarithmic layer. However, the downward shift of the 4mm and 5mm curves with respect to the smooth reference suggests an increase in skin friction drag. The velocity profiles of the cavity arrays in Figure 2.9b show an upward shift of the logarithmic region with respect to the smooth reference indicating a local skin friction reduction.

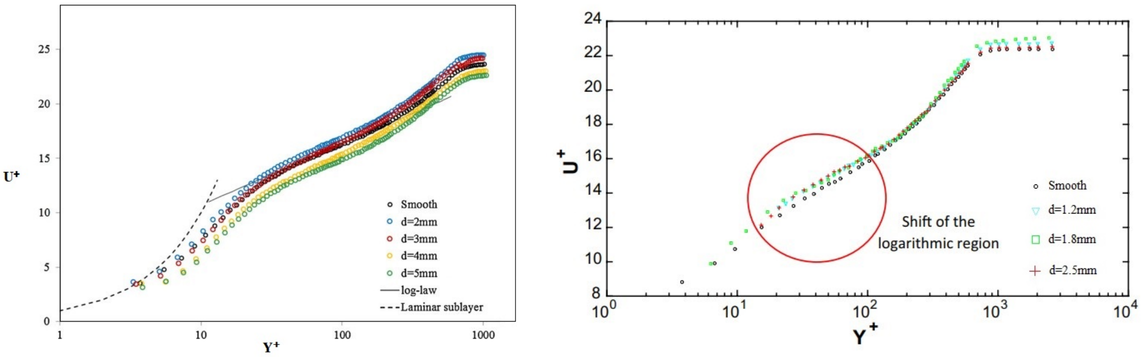

(a)

(b)

Figure 2.9: Velocity profiles measured downstream of the last row of cavities (a) Cavity arrays designed by Gowree et al. (2019) tested at $Re_\theta = 2710$, (b) Cavity arrays designed by Silvestri et al. (2017a) tested at $Re_\theta = 1927$

2. **Change in turbulence intensity**

   Turbulence intensity is the measure of turbulence energy production in the boundary layer. Kim et al. (1971) have stated that the phenomenon of bursting is responsible for the production of turbulence energy in the region $0 < y^+ < 100$ while Corino and Brodkey (1969) have concluded that ejections which occur 18% of the time are major contributors to turbulent energy. They have identified that this generation and dissipation of turbulence energy occurs in region $5 \leq y^+ \leq 70$. Thus, it is essential to analyse the influence of surface modifications on the energy of the turbulent boundary layer. The estimation of turbulence intensity in a three-dimensional flow field is as follows,

$$T.I = \frac{\sqrt{\frac{\overline{u^{2'}}+\overline{v^{2'}}+\overline{w^{2'}}}{3}}}{U} \tag{2.12}$$

where u', v' and w' are the velocity fluctuations in the x, y and z directions respectively.

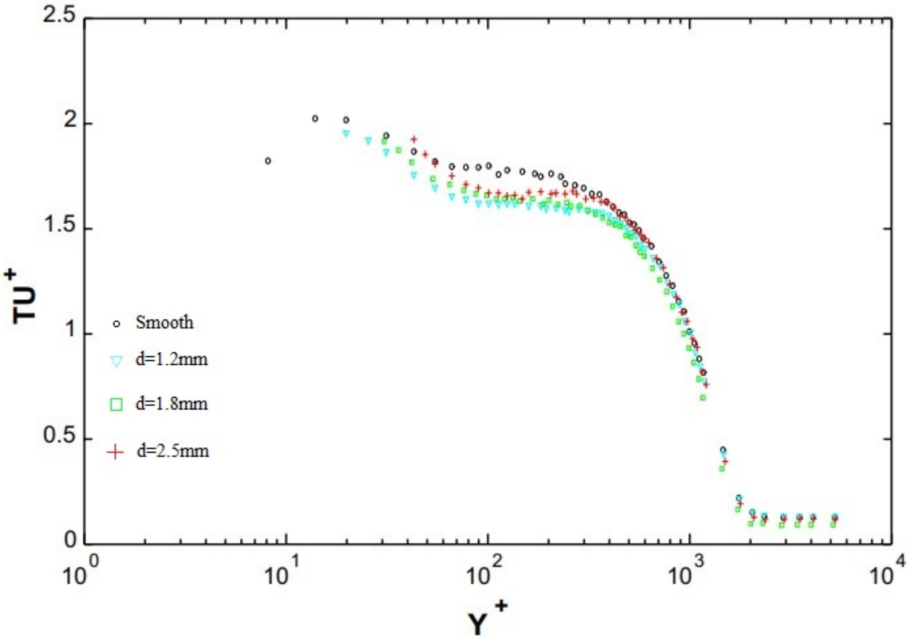

Figure 2.10: Turbulence intensity profile over cavity arrays tested at $Re_\theta = 3771$ (Silvestri et al., 2017a)

Figure 2.10 represents the turbulent intensity profiles calculated using streamwise velocity fluctuations measured by Silvestri et al. (2017a) downstream of cavity arrays of varying hole diameters and spacings (refer Figure 2.7a). It is evident that at the tested Re_θ all cavity arrays show a reduction in turbulence intensities with respect to the smooth reference. As discussed earlier, this indicates a reduction in turbulence energy in the logarithmic region.

Bhat et al. (2021) investigated the modification of streamwise and wall-normal velocity fluctuations in three regions: upstream of the cavity array, over the centre and downstream of the cavity array. It was observed that the reduction of wall-normal velocity fluctuations was larger than streamwise fluctuations because of flow interactions through the cavities. While the reduction of wall-normal fluctuations extended up to the outer layer of the boundary layer, reduction of the streamwise component was restricted to the inner layer. Thus, the overall reduction in turbulence intensity was observed in the buffer and logarithmic layers.

3. **Modification of turbulent events**

Turbulent events such as sweeps and ejections are responsible for the production of turbulence in the near-wall region (Kline et al., 1967; Corino and Brodkey, 1969; Robinson, 1991). A modification of these events could result in lower turbulent energy production, resulting in a decrease in skin friction drag. A method called the Variable Interval Time Averaging (VITA) technique was proposed Blackwelder and

Kaplan (1976) for the detection of sweep and ejection events which correlate with bursts in the turbulent boundary layer. Since bursts are associated with velocity fluctuations (Blackwelder and Eckelmann, 1979), a simple yet powerful criterion was formulated using streamwise velocity fluctuations measured by a hot-wire.

The application of the VITA technique can be used to identify the number, intensity and duration of bursts in the turbulent boundary layer. This technique has been widely used by researchers to characterise the turbulent activity in the presence of wall modifications like riblets (A. Hooshmand and Balint, 1982; Gallagher and Thomas, 1984; Choi, 1989) and pores (Wilkinson, 1983; Silvestri et al., 2017a; Scarano et al., 2022b; Severino et al., 2022). It has been observed that surface modifications that interact with turbulent structures reduce the number of bursts in the near-wall region. An example of this phenomenon studied by Scarano et al. (2022b) over circular cavities is shown in Figure 2.11, where the number of bursts has been shifted upwards for all cases indicating a reduction in near-wall turbulent activity.

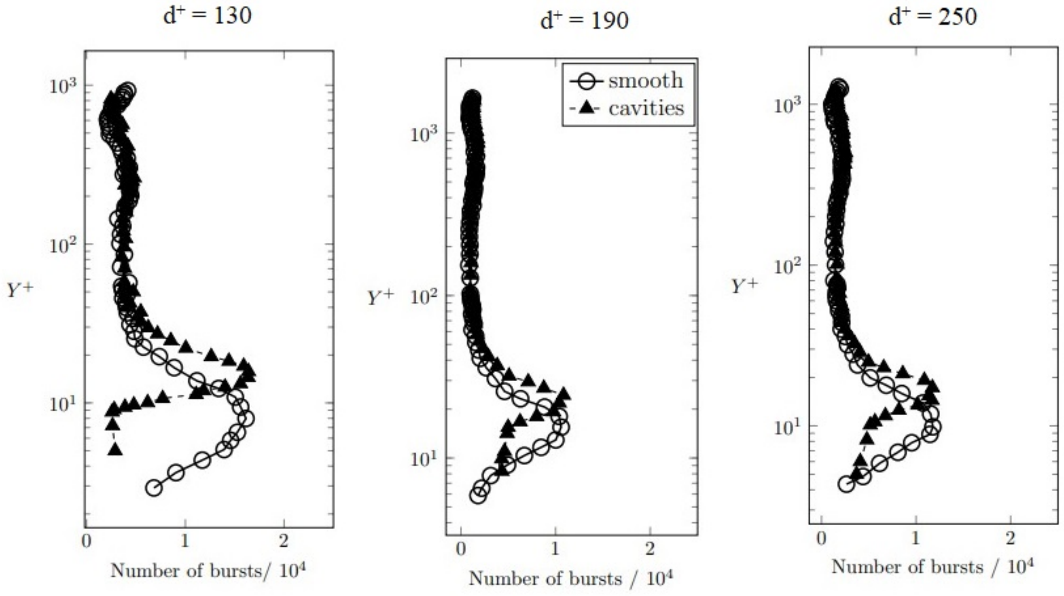

Figure 2.11: Number of bursts measured at the centre of cavity arrays of varying pore diameters in comparison with the smooth reference (Scarano et al., 2022b)

The intensity of bursts is estimated from the peak-to-peak value of the captured events (Silvestri et al., 2017a). Scarano et al. (2022b) reported that the largest relative reduction in burst intensity was present in the region $20 < Y^+ < 80$. A comparison between Silvestri et al. (2017a) and Scarano et al. (2022b) estimations of burst intensities as a function of Y^+ at different wall-normal wall distances is shown in Figure 2.12. Similar trends in intensities with increasing pore diameters have been observed with minor differences in values that can be attributed to the use of different VITA parameters. It is evident that the largest reduction in burst intensity is present in the near-wall region which reduces with increasing pore diameter. The duration of bursts can be estimated from the time interval between the peaks in the VITA analysis. The burst duration profile for a cavity array with pores of $d^+ = 130$ is shown in Figure 2.13. The most prominent reduction in burst duration occurs at $y^+ = 10$, supporting the earlier observations of reduced turbulent activity.

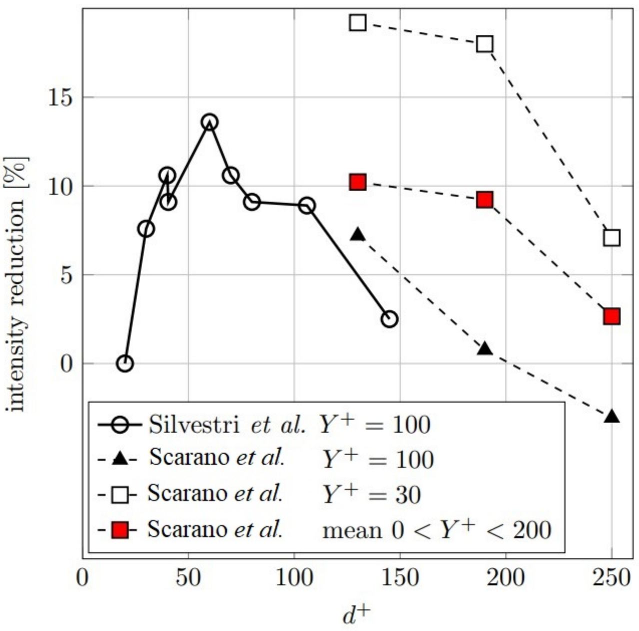

Figure 2.12: Comparison of burst intensity reductions with respect to a smooth reference measured at the trailing edge of cavity arrays as a function of d^+ (Scarano et al., 2022b)

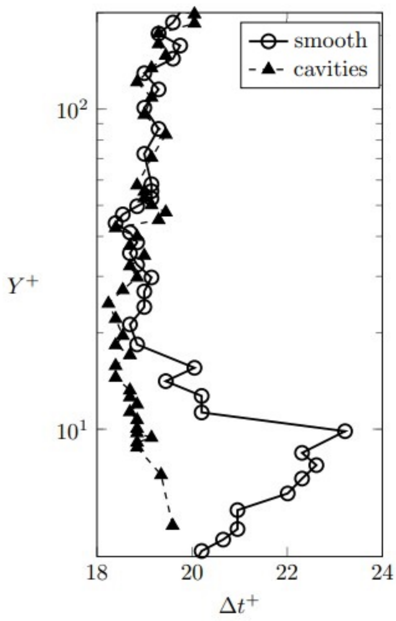

Figure 2.13: Duration of bursts at the centre of a cavity array with pores of d^+=130 compared with the smooth reference (Scarano et al., 2022b)

2.4.1. Estimation of skin-friction

One of the most common methods to estimate skin friction drag is using Clauser (1956)'s technique as discussed earlier. Local changes in skin friction drag are estimated by observing the shift in the velocity profile over the perforated plate with respect to a smooth plate. However, as Clauser's technique has been derived for a smooth plate, the accuracy of results for a perforated plate is questionable. Gowree et al. (2019) reported a quantification of turbulent skin friction from momentum thickness of the turbulent boundary layer. The momentum-integral equation for a zero pressure gradient flow reduces to

$$C_f = 2\frac{d\theta}{dx} \tag{2.13}$$

The above equation was extended to a spanwise periodic mean flow case by Gowree et al. (2019) using the three-dimensional momentum integral equations formulated by Ashill and Smith (1985) for an incompressible, zero pressure gradient flow without a streamline curvature. The skin friction estimate from this method is the value averaged over the length of the plate and not a local skin friction value. The skin friction values obtained from the velocity profiles and momentum-integral equations for three flow conditions as a function of pore diameter to pore depth are shown in Figure 2.14. Key differences are the rate of change of skin friction which can be observed to be steeper in Figure 2.14a and the skin friction curve at 15m/s which shows a reduction for all ratios of d/h in Figure 2.14b. Although there are small differences in drag values at higher flow speeds, the trends are similar in both cases. From this analysis, it is difficult to estimate which method is more accurate as both methods are based on certain assumptions.

Bhat et al. (2021) estimated the skin friction drag over a micro-cavity array with a backing cavity developed by Silvestri et al. (2017b) using the FIK identity (Fukagata et al., 2002) for a fully developed turbulent channel flow using DNS. The FIK identity is given as follows

$$C_f = \frac{12}{Re_b} + 12\int_0^1 2(1-y^*)(-\overline{u^*v^*})dy^* - 12\int_0^1 (1-y^*)^2\left(\frac{\partial\overline{u^*u^*}}{\partial x^*} + \frac{\partial\overline{u^*v^*}}{\partial x^*} - \frac{1}{Re_b}\frac{\partial^2\overline{u^*}}{\partial x^{*2}} + \frac{\partial p^*}{\partial x^*}\right)dy^* \tag{2.14}$$

where Re_b is the bulk Reynolds number calculated as $Re_b = 2U_b\delta/\nu$ and parameters with a * have been normalised with the channel half-width(δ) and two times the bulk velocity ($2U_b$). In the above

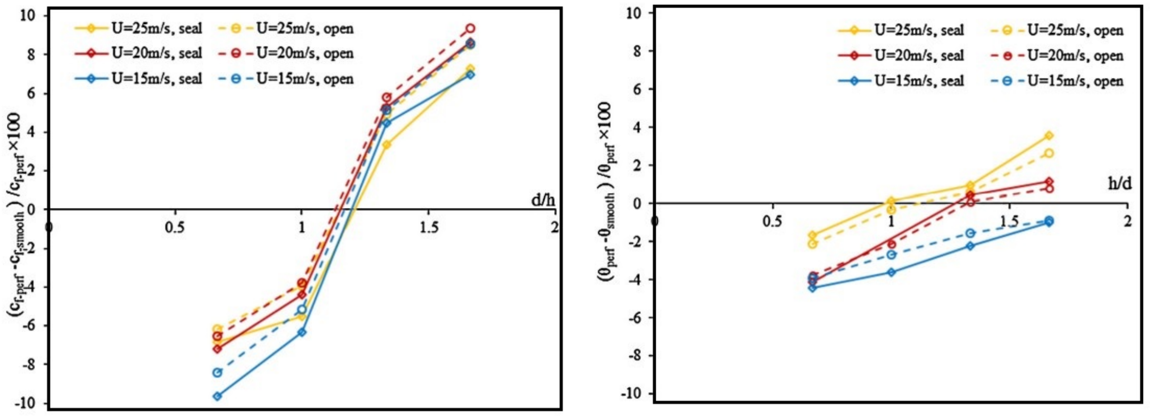

(a)

(b)

Figure 2.14: Skin friction estimation of a perforated plate with respect to a smooth plate as a function of the ratio of pore diameter to pore depth (d/h) (Gowree et al., 2019) (a) Local skin friction coefficients obtained from velocity profiles, (b) Momentum thickness averaged over the length of the plate

equation, the first term represents the laminar contribution, the second term represents the turbulent contribution which is the Reynolds shear stress and the last term represents the inhomogeneity and pressure gradient of the flow. In the DNS study (Bhat et al., 2021), the mean bulk flow was kept constant due to which the laminar contribution was a constant and the flow inhomogeneity and pressure gradient contributions were observed to be minimal. The most significant contribution to the skin friction coefficient was from the Reynolds shear stress. The reductions in wall shear stress and corresponding skin friction coefficient at different streamwise locations and downstream of the cavity array is shown in Figure 2.15. The plotted values have been normalised with the values at the leading of the cavity array. It is evident that reduction of both parameters increases along the streamwise direction with the largest reduction observed at the trailing edge and continues to extend up to a distance downstream of the array beyond which they decline. The overall reduction in skin friction drag estimated from the integral of wall shear stress over the perforated plate area has been reported to be 5.6%.

2.5. Working mechanism of wall-normal pores

As discussed in the previous sections, micro-cavity arrays have been shown to both increase and decrease drag. Along with the measurements of drag, some researchers have attempted to study the mechanism for the perceived drag behaviour using flow visualization techniques while others have suggested hypotheses based on obtained results. The various hypotheses for the observed drag behaviour are discussed in this section.

2.5.1. Hypotheses for drag increase

1. **Wall-blowing phenomena**
   Burden (1969) theorised that localised low-pressure zones are formed over the porous surface resulting in fluid being pushed into the boundary layer. This localised adverse pressure gradient destabilises the boundary layer by creating a "wall-blowing" action. Similarly, local regions of high pressure create a "wall-suction" action which stabilises the boundary layer. However, the destabilising wall blowing action has been observed to last longer thereby leading to a net increase in drag. Moreover, Wilkinson (1983) reported that perforated plates with pore diameters and spacings less than 100 wall units produce large values of skin friction drag. This is due to the interaction of fluid injected through the pores with the low-speed streaks resulting in violent bursting.

2. **Unstable vortices**
   Choi and Fujisawa (1993) suggested that the drag-reducing mechanism for a groove is the presence of a stable vortex inside the cavity which absorbs the incoming flow and reorganises it. On the contrary, it

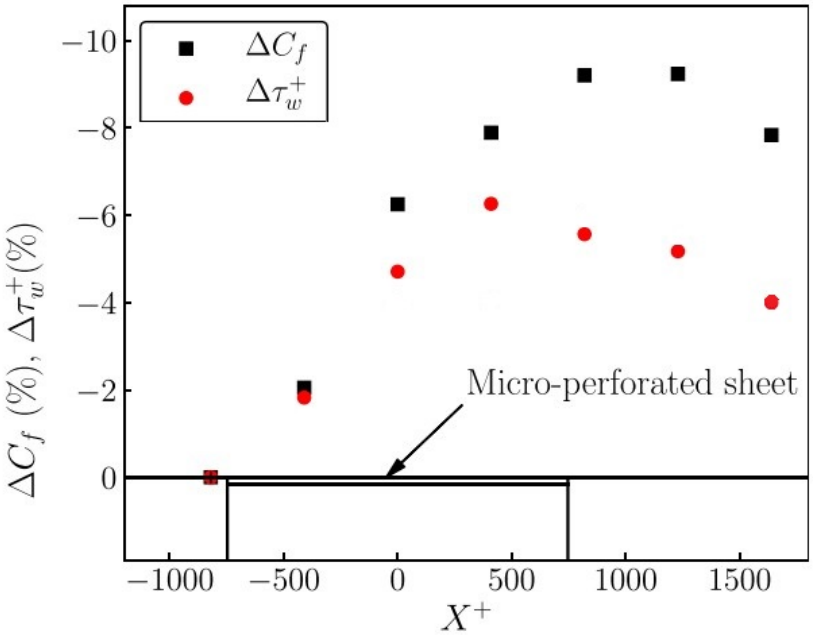

Figure 2.15: Percentage reductions in skin friction coefficient and wall shear stress along the streamwise direction of the cavity array normalised with the values at the leading edge of the array (Bhat et al., 2021)

has been theorised by Wilkinson (1983) that cavities with unstable vortices push fluid out of the cavity leading to increased drag. Kong and Schetz (1982) have also proposed that an increase in skin friction drag could be caused by the normal component of turbulence which penetrates the porous surface. In essence, this mechanism is similar to the wall-blowing action where a fluid ejection causes drag rise.

3. **Pressure forces**
   A common observation reported by several studies is the increase in drag with increasing pore diameter and increasing porosity of the perforated plate (Wilkinson (1983), Gerhold et al. (2016), Drouin et al. (2006)). One of the major contributors to cavity drag is pressure forces on the downstream wall of a cavity due to impingement of the shear layer. Therefore, it is evident that pressure drag contributes to the overall drag produced by a perforated plate and its effects should not be neglected.

2.5.2. Hypotheses for drag reduction

1. **Capturing of turbulent structures**
   Experimental studies by Silvestri et al. (2017a) have shown that micro-cavities were capable of reducing the turbulent energy of the boundary layer. The initial hypothesis was that cavities capture sweep events leading to the disruption of the bursting process. To determine what happens to the sweep events that enter the cavities, Silvestri et al. (2017b) studied the effect of a backing cavity below the cavity array. From this study, it was theorised that turbulent energy of the captured events are damped by friction losses in the cavity array and backing cavity thus weakening the structure of the events.

2. **Redistribution of turbulent energy**
   Another hypothesis suggested by Silvestri et al. (2017b) experiments with a backing cavity is the redistribution of turbulent energy of a single sweep event across all the cavities in the array through the backing cavity. This reduces the overall energy of the event and consequently, the ejection event that arises from the sweep has low energy. Overall, the turbulence in the near-wall region decreases. The authors also suggest that the backing cavity volume plays an important role in the reduction of turbulent intensities, with smaller volumes having a higher flow impedance which decreases with increasing volumes resulting in a non-linear reduction in turbulence energy. However, a later study by (Silvestri et al., 2018), showed that the redistribution theory was invalid as turbulent energy reduction was observed irrespective of the connection between the cavities.

3. **Wall-normal interactions**
   A DNS study by Bhat et al. (2021) showed that the strength of coherent structures in the log layer over the porous array was reduced which resulted in the reduction of Reynolds shear stresses. The hypothesis formulated from this observation is that the wall-normal velocity fluctuations are dampened by the wall-normal interactions of the near-wall flow with the pores. This interaction has been observed to be localised to the area of the pores thereby resulting in localised reduction in shear stresses.

4. **Spanwise flow oscillations**
   Flow visualisations on a spanwise plane along with LDA measurements by Gowree et al. (2019) revealed a non-uniform flow with transverse velocity components which the authors claimed to resemble the flow over riblets. This was further evaluated in a recent study by Scarano et al. (2022b) where the authors hypothesize that the mechanism for skin friction drag reduction by pores is similar to that of dimples proposed by van Nesselrooij et al. (2016). It has been suggested that staggered pores passively create spanwise wall oscillations which disrupt the near-wall cycle, thus reducing the Reynolds shear stresses.

2.6. Concluding remarks

This chapter aimed to present and discuss existing research on passive flow control by wall-normal pores. The precursor to wall-normal pores were Helmholtz resonators, which have shown a tendency to reduce the turbulent energy in the near-wall region of the boundary layer even in the absence of resonance. Current designs of acoustic liners are successful at reducing the noise produced by aircraft propulsion systems but this has been achieved at the cost of additional drag. However, research on acoustic liners has paved the way to identify the parameters that are crucial for optimizing the design of perforated plates.

Micro-cavity arrays designed with pore diameter and spacings in the order of the coherent structures have been shown to reduce the turbulence energy in the near-wall region of the turbulent boundary layer. Bhat et al. (2021), Gowree et al. (2019) and Scarano et al. (2021) have performed computational and experimental analyses on flat plates with micro-cavity arrays and reported that certain designs experienced a reduction in skin friction drag. However, these studies do not report the contribution of pressure drag. Moreover, the experimental results on the skin friction drag performance of pores have been obtained indirectly through hot-wire measurements. Direct measurement of the overall drag of micro-cavity arrays has not been performed. Another ambiguous aspect is the the mechanism responsible for the perceived skin friction reduction. Several hypotheses have been proposed by various research groups based on their observations but a consensus is yet to be reached.

Conflicting results relating to the drag performance of grooves suggest that optimally designed grooves are capable of reducing skin friction drag under certain conditions. However, it is uncertain if the contribution of pressure drag will overtake the achieved skin friction drag reduction. This investigation showed that the spacing between grooves is a significant parameter that influences drag. Further investigations on how this design parameter affects the drag of micro-cavity arrays should be performed for optimising its design.

Thus, this thesis aims to address these gaps and inconsistencies in literature. Validation of existing micro-cavity designs will be performed to replicate current findings and determine the effects of pressure drag along with a flow characterisation study to understand the flow mechanism in the near-wall region in the presence of cavities.

3

Experimental Methodology

This chapter presents the methodology for the experimental campaigns. First the design and production of the test plates are presented followed by the experimental setup, plan and data-processing steps. Direct force measurements (DFM) were performed for characterising the drag performance and flow field measurements for investigating the working mechanism of the various designs .

3.1. Parameters influencing the design of micro-cavity arrays

As discussed in the previous chapter, a micro-cavity array is an organised arrangement of wall-normal pores with fixed geometrical parameters. The geometrical parameters include pore diameter, pore depth, spanwise and streamwise pore spacings, and pore alignment. For effective boundary layer control, the dimensions of these parameters must adhere to certain design guidelines derived from various studies. The guidelines related to each parameter are given below,

Pore diameter

The size of the pore is an essential parameter that governs the interaction of the coherent structures with the pores. For turbulent boundary layer control, Lockerby (2021) suggested that the diameter (D) of a circular orifice must not exceed 40 times the viscous length scale ($D^+ < 40$). Silvestri et al. (2017a) tested this guideline by performing an experimental analysis of micro-cavity arrays with pore diameters in viscous units ranging from 20 to 145 and reported that the maximum reduction in turbulence energy occurred at $D^+ = 60$. The study also suggested that the optimal range of pore diameter for reducing turbulent energy is 30 to 145. However, Gowree et al. (2019) reported that micro-cavity arrays with pores diameters ranging from 130 to 250 experienced local reduction in skin friction drag. The discrepancy in these results could be attributed to the pore arrangement as the former worked with aligned configurations and the latter with staggered configurations.

Pore spacings

The distance between neighbouring pores in the streamwise and spanwise directions should correlate with the spacing of the coherent structures in the near-wall region for effective interaction. The idea is to interrupt the low-speed streaks through flow disturbance provided by the pores. Targeting the streaks would attenuate the bursting process which produces turbulence. As low-speed streaks have an average spanwise spacing of 100 viscous units (Kline et al., 1967), the spanwise distance between pores is required to be more than or equal to 100 viscous units (Lockerby, 2021). The streamwise length of low-speed streaks is up to 10 times its spanwise spacing (Blackwelder and Eckelmann, 1979), therefore the streamwise spacing between pores should be less than the length of streaks to break it apart.

Pore depth

The depth of the pore is another important factor that determines the extent to which the pore disrupts the near-wall turbulent energy. Gowree et al. (2019) studied the effect of varying the diameter to depth (d) ratio of pores. It should be noted that in this study the diameter of the pore was varied by keeping the pore depth constant. It was reported that for arrays with D/d le 1, a skin friction drag reduction of up to 10% was observed using Clauser's technique while for arrays with D/d > 1, there was a sharp rise in skin friction drag. A recent study by Severino et al. (2022) investigated the effect of pore depth by varying the pore depth with a constant pore diameter. In this investigation, the ratio D/d for all designs was less than one with its value ranging from 0.067 to 0.33. It was observed that with increasing pore depth (within the bounds of the investigated depths), the reduction in streamwise turbulent energy increased. As a similar trend in turbulence attenuation was observed by different research groups when the ratio D/d < 1, this can be accepted as a reliable design guideline.

Pore alignment

The alignment of pores with respect to the incoming flow is a design parameter without any specific guidelines. Several studies have analysed micro-cavity arrays with aligned configuration (Silvestri et al., 2017a,b; Bhat et al., 2021; Severino et al., 2022) and staggered configuration (Gowree et al., 2019; Scarano et al., 2021, 2022b) and both configurations have shown potential to reduce turbulent energy.

Porosity

Porosity is defined as the ratio of volume of the fluid to the volume of the solid. This design parameter is commonly used for the design of acoustic liners. Although, no specific guidelines were identified for the design of drag-reducing pores, some studies on liners have reported that drag increases with increasing porosity (Wilkinson, 1983; Drouin et al., 2006; Gerhold et al., 2016). For the aligned and staggered configuration of pores, the porosity is calculated as follow;

$$\sigma_a = \frac{\pi D^2}{4L_x L_z}; \qquad \sigma_s = \frac{\pi D^2}{2L_x L_z} \tag{3.1}$$

where, D is the pore diameter and L_x, L_z are the streamwise and spanwise spacings.

The ranges of the above parameters investigated by the two research groups involved in the study of micro-cavity arrays are listed in Table 3.1.

Table 3.1: Geometrical parameters for the design of micro-cavity arrays

Geometrical parameter	**Silvestri et al. (2017a)**	**Scarano et al. (2022b)**
Configuration	Aligned	Staggered
Pore diameter (d^+)	30 to 145	130 to 250
Spanwise spacing (L_z^+)	>100	587 to 1075
Streamwise spacing (L_x^+)	<1000	587 to 1075
Pore diameter to depth ratio	0.07 to 0.33	≤ 1

3.2. Test environment

For designing micro-cavities as per the guidelines, prior knowledge of the testing environment is required. All the experiments were performed in the M-Tunnel located in the Low-Speed Laboratory at the Delft University of Technology. It has a test section of 400 × 400 mm and a maximum freestream velocity of 35 m/s. Drag measurements were performed using a force balance called 'The Hill' developed by Dimple Aerospace B.V. This device measures drag at freestream velocities ranging from 5 to 35 m/s. A fresh turbulent boundary layer starts at 0.6m upstream of the leading edge of a test plate placed in the balance.

Using empirical relations, the friction velocity (u_τ) and corresponding viscous length scale (δ_v) over a smooth flat plate in a zero pressure gradient turbulent boundary layer at standard atmospheric conditions is estimated. This is shown in Figure 3.1 with x_{TP} denoting the streamwise location along the smooth plate. Here, $x_{TP} = 0$ is located 0.6m behind the start of the TBL to simulate the conditions over a plate placed in the Hill. It is evident from the figures that both u_τ and δ_v are nearly constant along the plate but vary significantly with U_∞. Thus, the dimensions of the micro-cavity array parameters can be scaled for a chosen value of U_∞ with its corresponding δ_v.

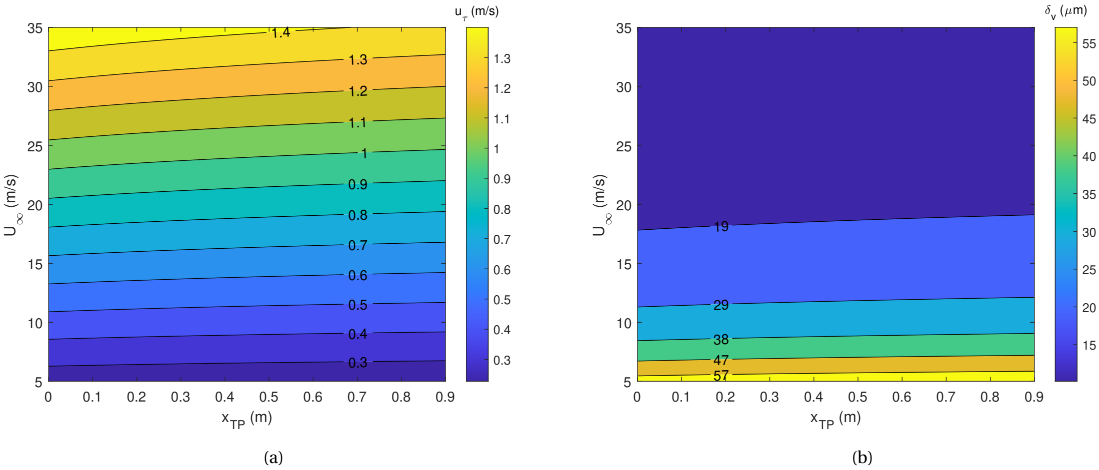

(a)

(b)

Figure 3.1: Theoretical values of TBL parameters over a smooth plate (a) Friction velocity, u_τ (b) Viscous length scale, δ_ν (Hartog, 2021)

3.3. Selection of designs

The designs that were selected for investigation in this thesis are listed in the design matrix (Table 3.2). While some designs were replicated from literature for validation, several new ones were introduced by altering one or more parameters. The new designs were selected to investigate parametric trends in the performance of pores and grooves for the determination of an optimised design. From left to right, the columns of the design matrix describe the design names (explained in the following subsections), description of the design, size of the design element (pores in diameter (D), backing cavities and grooves in widths (w)), streamwise (L_x) and spanwise (L_z) spacing between neighbouring elements, element depth (d), porosity (σ) and pattern of arrangement on the test plate. A schematic of micro-cavity arrays with the aligned and staggered pore arrangements is shown in Figure 3.2.

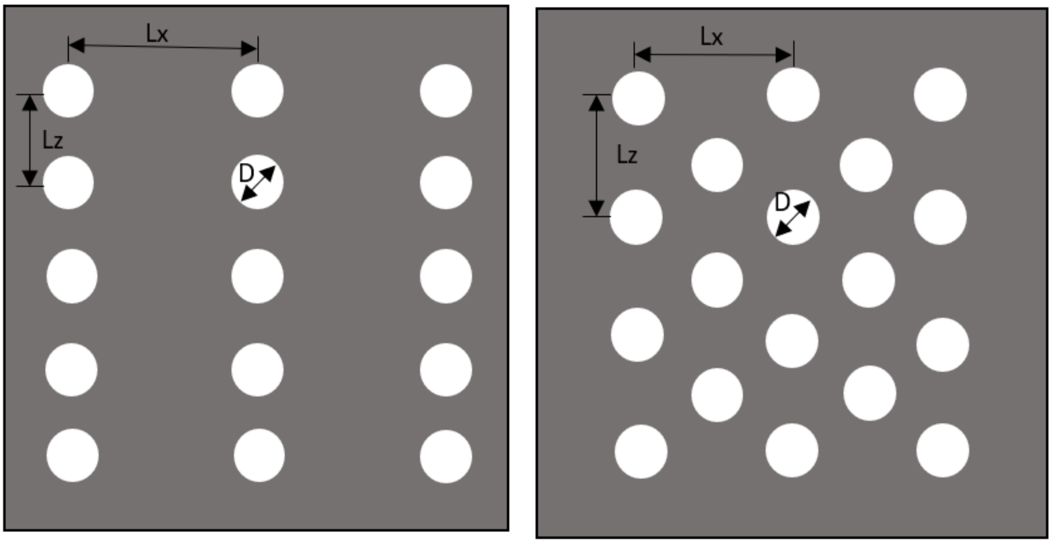

(a)

(b)

Figure 3.2: Schematic of micro-cavity arrays (a) Aligned configuration (b) Staggered configuration

Table 3.2: Design matrix of test plates

Name	Description	D or w (mm)	L_x (mm)	L_z (mm)	d (mm)	σ (-)	Configuration
			Silvestri's pore designs				
PS-C	Replica	1.2	15	3	2	0.025	aligned
PS-S	Small D	1.2	15	3	5	0.025	aligned
PS-M	Medium D	1.8	15	4.5	5	0.038	aligned
PS-L	Large D	2.5	15	6	5	0.055	aligned
			New pore designs				
PN-B	Baseline	0.8	10.2	2	5	0.025	aligned
PN-DL	Large D	1.2	10.2	2	5	0.055	aligned
PN-XS	Small Lx	0.8	3	2	5	0.084	aligned
PN-XM	Medium Lx	0.8	5.1	2	5	0.05	aligned
PN-ZL	Large Lz	0.8	10.2	3.1	5	0.016	aligned
PN-dS	Small d	0.8	10.2	2	2	0.01	aligned
PN-ST	Configuration change	0.8	10.2	10.2	5	0.01	staggered
			New backing cavity designs				
PC-X	Streamwise aligned	36.4	-	1.6	3	-	streamwise
PC-Z	Spanwise aligned	45.8	5.2	-	3	-	spanwise
PC-R	Rectangular	36.4 * 45.8	5.2	1.6	3	-	rectangular
			Permeable trailing edge designs				
PA-S	Small spacing	0.8	2.5	2.5	5	0.161	staggered
PA-M	Medium spacing	0.8	3	3	5	0.112	staggered
PA-L	Large spacing and width	0.8	5	5	5	0.04	staggered
			New groove designs				
G-S	Small spacing	1	10.2	-	1	-	spanwise
G-M	Medium spacing	1	20	-	1	-	spanwise
G-L	Large spacing	3	60	-	3	-	spanwise

Silvestri's pore designs: PS ("Porous, Silvestri")

PS-C is a replica of the design analysed by Silvestri et al. (2017b) as shown in Figure 3.3. The dimensions of the cavity array and its position with respect to the start of the boundary layer were replicated. Due to size restrictions with the drag measurement equipment, the backing cavity was designed with a depth of 3mm. Additionally, care was taken to obtain the exact number of pores to match its overall porosity. Designs PS-S, PS-M and PS-L were selected from the design optimisation study performed by Silvestri et al. (2017a) to validate the reported results.

New pore designs: PN ("Porous, New")

A design (PN-B) with pore dimensions and spacings matching in viscous units with the optimised design of Silvestri et al. (2017a) was chosen for the validation of reported results. This design also served as the baseline for the parametric study. The remaining designs in this category were developed by changing one parameter at a time with respect to the baseline design. The modified parameter in each plate design is highlighted in blue. The values of the parameters were varied within the ranges stipulated by the design guidelines. A design with a larger pore diameter was chosen to evaluate the contribution of pressure drag. To study the effect of pore spacing on the turbulent structures a few designs with modified streamwise and spanwise spacings were introduced. The pore depth was reduced to test the hypothesis that the pores capture sweep events. Finally, to understand the effect of pore configuration, a staggered arrangement was included.

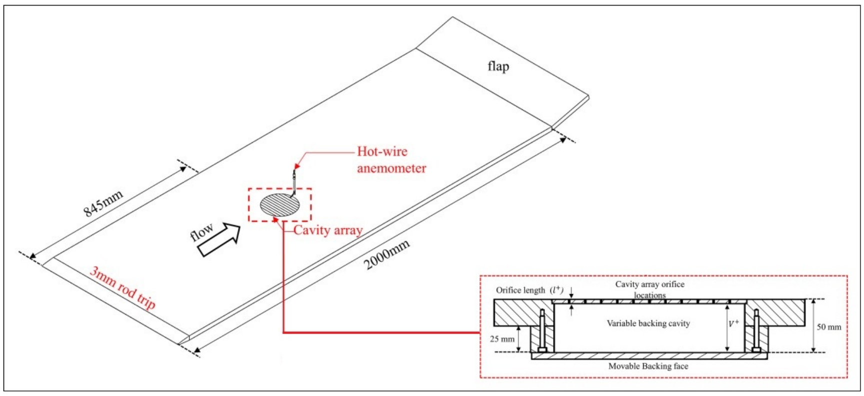

Figure 3.3: Schematic of the experimental setup of Silvestri et al. (2017b)

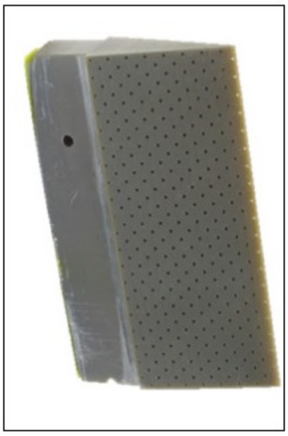

Figure 3.4: Permeable trailing edge design of Rubio Carpio et al. (2020)

New backing cavity designs: PC ("Porous, Cavity")

A backing cavity is a region of enclosed space beneath a micro-cavity array. The influence of a backing cavity on the near-wall turbulent energy was investigated by Silvestri et al. (2017b). The authors reported that turbulence energy reduced non-linearly with increasing cavity volume. To extend understanding of the working mechanism of backing cavities, three designs were chosen. These were streamwise aligned, spanwise aligned and rectangular cavities. Similar to PS-C, all the backing cavities had a depth of 3mm. The backing cavities were not sealed, however, when placed in the force balance the bottom was flushed with the surface forming a closed cavity. These backing cavities connect multiple pores based on their size. The streamwise aligned design connects the largest number of pores while the rectangular cavities connect fewer pores.

Permeable trailing edge designs: PA ("Porous, Acoustic")

Designs PA-S, PA-M and PA-L were inspired from an acoustic study performed by Rubio Carpio et al. (2020) on permeable inserts attached to the trailing edge of a NACA 0018 airfoil (Figure 3.4). Experiments conducted in an aeroacoustic wind tunnel showed noise attenuation by the inserts compared to a solid trailing edge. Therefore, these designs were chosen to investigate their drag characteristics.

New groove designs: G ("Groove")

As discussed in Section 2.3.3, studies on grooves have reported inconsistent results concerning drag performance. These inconsistencies were observed irrespective of similarities in designs and testing conditions. The G-L design in this study was based on the drag-reducing grooves of Tani et al. (1988). The motivation for the G-S and G-M designs was to investigate the potential for a correlation between pores and grooves. The ambiguous parameter in the design of grooves was the spacing. While Tani et al. (1988) and Coustols and Savill (1992) have observed drag reduction when grooves were spaced at twenty times their width, Elavarasan et al. (1995) and Wahidi et al. (2005) have reported an increase in drag. To further investigate this parameter, a new design (G-M) with groove dimensions corresponding to the baseline of the micro-cavity arrays with spacing increased to twenty times its width was included.

3.4. Design Process

Following the selection of designs, the next step was the creation of test plate geometries using a CAD software. The software used for this purpose was CATIA V5, a computer-aided design software by Dassault Systèmes. All geometries were designed according to the dimensional requirements of the drag measurement device, the Hill. The device accepts test plates measuring 881.3 mm × 366.3 mm × 5 mm. As the selected material of the test plates was acrylic, the plate dimensions were reduced by 0.2 mm on all sides. From prior experience, it was observed that acrylic plates expanded during warmer months owing to the high thermal coefficient of the material. As the plates were to be designed and produced during winter and tested during spring, the final designs measured 880.9 mm × 365.9 mm × 5 mm.

Two-part plate designs

Some test plates were designed in two parts consisting of a porous or grooved top surface attached to a backing cavity or a smooth bottom surface. Table 3.3 presents a list of the top and bottom surfaces along with a reference to their CATIA design. For designs in which the pores or grooves were less than 5mm in depth, smooth flat plates were designed as the bottom surface. For the backing cavity designs, the baseline design PS-B was chosen as top surface. The length and width of the bottom plates were smaller by 1mm to allow sufficient room during assembly.

Table 3.3: Description of two-part plate designs

Top surface	**Bottom surface**	**CATIA design**
PS-C	Single backing cavity	Figure 3.5
PN-B	PC-X	Figure 3.6a
PN-B	PC-Z	Figure 3.6b
PN-B	PC-R	Figure 3.6c
G-S	4mm thick smooth flat plate	Figure 3.7
G-M	4mm thick smooth flat plate	Figure 3.8a
G-L	2mm thick smooth flat plate	Figure 3.8b

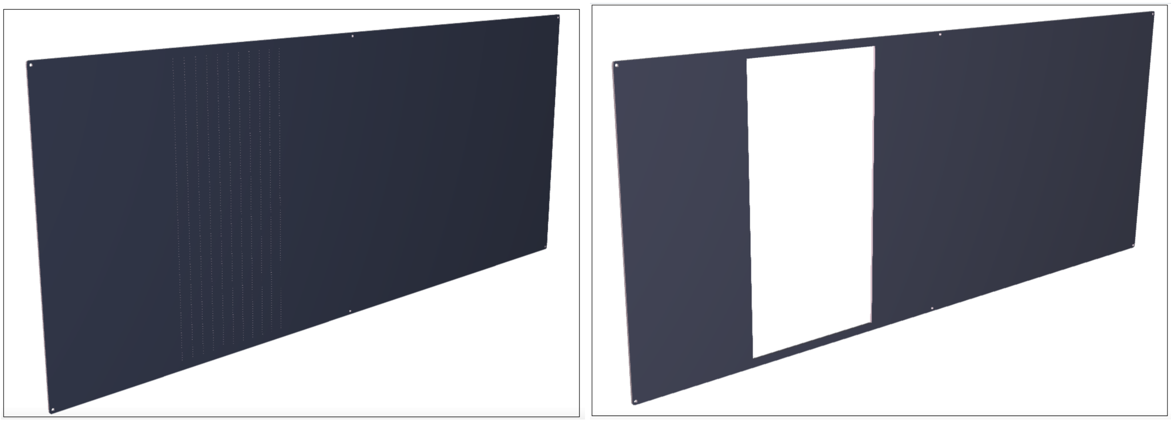
(a) (b)

Figure 3.5: CATIA design of the PS-C design (a) Top plate (b) Bottom plate

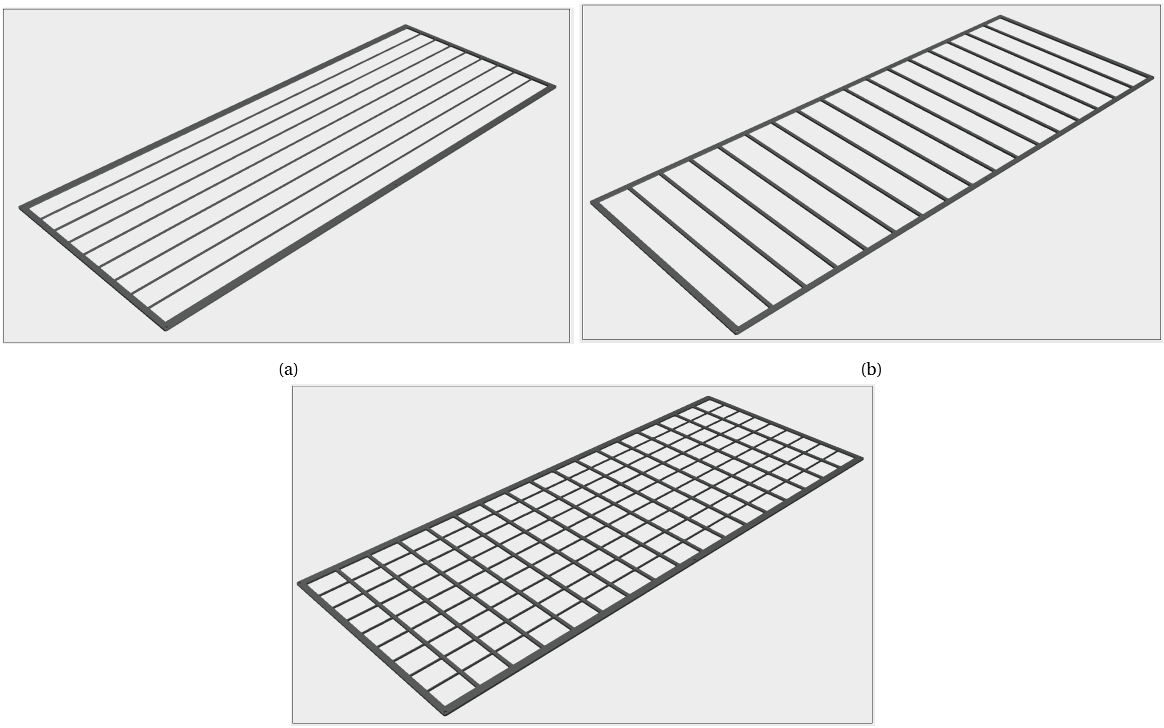
(a)
(b)
(c)

Figure 3.6: CATIA designs of plate with backing cavities (a) Streamwise aligned (PC-X) (b) Spanwise aligned (PC-Z) (c) Rectangular (PC-R)

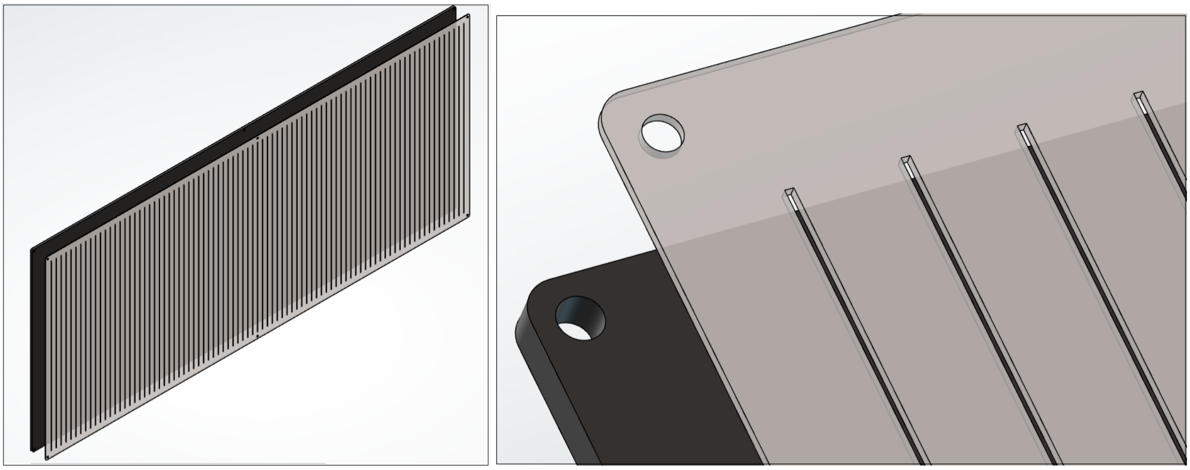
(a)
(b)

Figure 3.7: (a) CATIA design of the G-S grooved plate with a smooth back plate (b) A zoomed-in view of the grooves

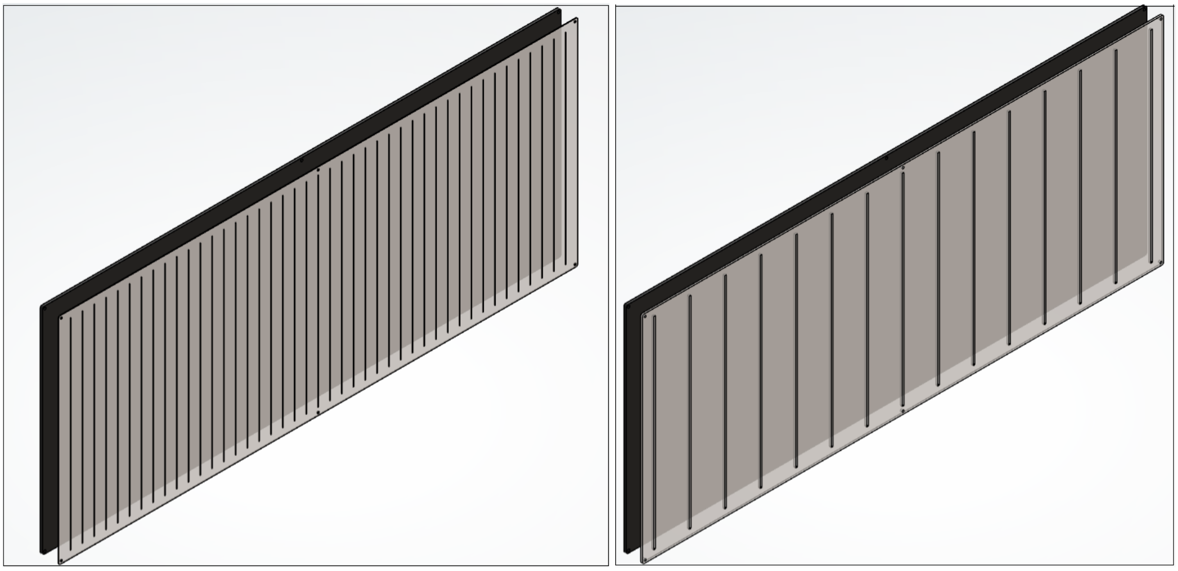

(a)

(b)

Figure 3.8: CATIA designs of the grooved plates with a smooth back plate (a) Grooves with medium spacing, G-M (b) Grooves with large spacing and width, G-L

3.5. Model production

The selected material for the test plates was Polymethyl methacrylate commonly known as acrylic. Acrylic was chosen because it is inexpensive and can be easily machined using laser cutting. The disadvantage of acrylic is its sensitivity to heat which causes the material to expand even with small changes in ambient temperature. The linear thermal expansion coefficient of acrylic ranges from 68 to 75 μm/(m °C) indicating that for every degree rise in temperature, the material expands by 68 to 75 μm for every meter. This was accounted for in the design of the test geometries. The machining process chosen for the creation of pores, grooves and cavities on the surface of acrylic was laser cutting. This was performed by Laserbeest, a laser-cutting service provider in Delft.

Working principle laser cutting

There are two common types of laser cutting based on the laser source: CO_2 and fibre. This section briefly discusses the working principle of both types. Inside the laser head, a high voltage is passed through a glass tube filled with carbon dioxide which increases the energy of the gas particles resulting in the production of light. The glass tube contains a partially reflective mirror on one end and a fully reflective mirror on the other end. The generated light is reflected back and forth by these mirrors as it flows through the tube thereby increasing its intensity. Once the light intensity reached a certain threshold, it passes through the partially reflective mirror. It is then guided by mirrors to leave the laser head as a highly concentrated laser beam as shown in Figure 3.9a. The laser beam is directed from the final mirror through a focusing lens onto the working material. A converging lens is used to focus the laser beam into a small precise spot. The diameter of the laser beam is typically reduced from about 7 mm to 0.1 mm. The focused laser beam has a higher intensity and is capable of vapourising a specific area of the working material. A nozzle surrounding the tip of the tube has air flowing through it at high speeds to remove molten material. The laser-cutting machine has a CNC system which facilitates the movement of the laser head in various directions over the workpiece.

The fibre laser-cutting follows a similar working principle with the only difference being in the production of the laser beam. The beam is generated through laser diodes in the fibre laser cutting machine and transmitted to the laser head through a fibre optic cable. The fibre laser beam has a shorter wavelength than the CO_2 lasers which increases its speed, consistency and quality.

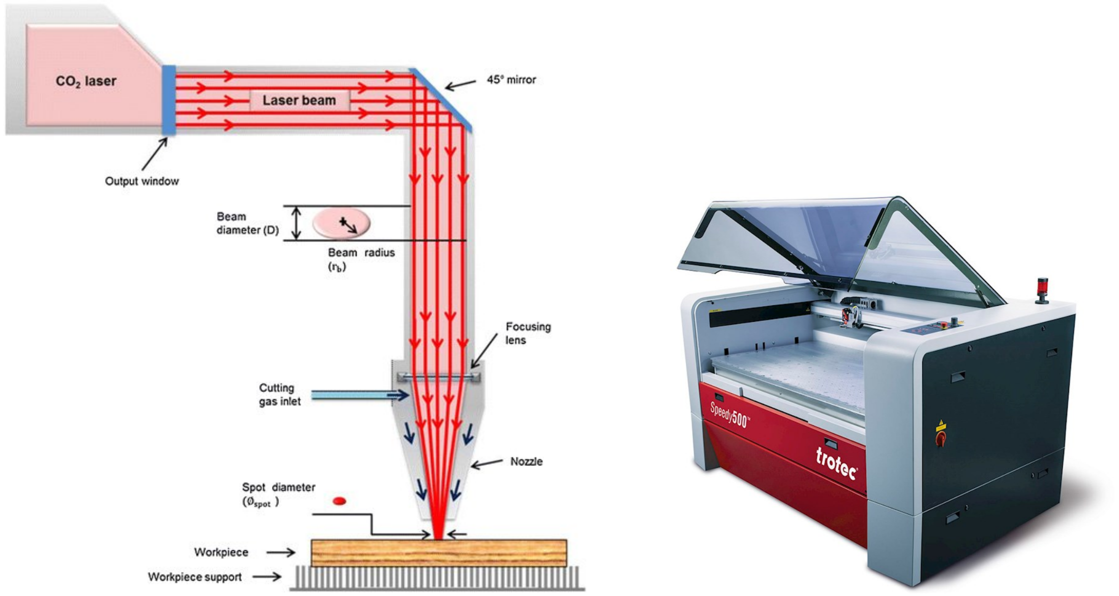

(a) (b)

Figure 3.9: (a) Diagrammatic representation of CO_2 laser cutting (Martinez-Conde et al., 2017) (b) The Trotec Speedy 500 laser cutting machine

Dimensional tolerance of the cut

The dimensional tolerances of the laser cut are dependent on the width of the laser beam. Values of the design diameters vs laser cut hole diameters are shown in Figure 3.10. From this, it was estimated that the overall tolerance of the laser cut is approximately 0.2 mm. This tolerance is quite low, especially for the porous designs as an increase of 0.2 mm in pore diameter could significantly alter its characteristics. Therefore, in the CAD design of the models, a correction was applied to the pore diameter and widths of the cavities and grooves. The design dimensions were reduced by 0.2 mm to account for the tolerance of the laser beam width.

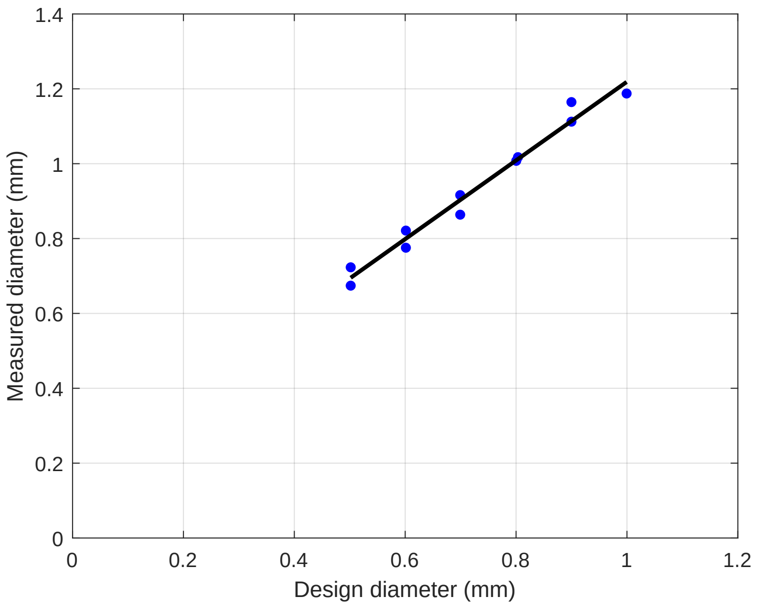

Figure 3.10: Dimensional tolerance of the laser beam

Process

Cast acrylic plates measuring 900 mm × 600 mm were used as the base workpiece. After the pores, grooves and cavities were cut from the acrylic plates, the outer edges of the test plate were laser cut for the bottom plate designs. This was performed only for the bottom plate designs as the edge tolerances for these plates are less significant. The top plate designs and the single plates were milled using CNC machines at DEMO to achieve high tolerances. The tolerance of these plates was given importance as they are required to fit perfectly in the drag measuring equipment.

3.6. Model assembly and adjustments

After the production of the test plates, the two-part plate designs enlisted in Table 3.3 were assembled. For the assembly, different types of adhesives were tested on sample acrylic pieces to determine the bond strength, working and curing times. Instant adhesives like Loctite-401 did not provide sufficient working time. A polyurethane adhesive formed a strong bond between the sample plates but the adhesive formed a thin layer between them increasing the overall thickness of the assembly. This is undesirable due to the dimensional limitations of the Hill. An epoxy adhesive was observed to form a strong bond between the samples without altering the thickness of the assembly and also provided a working time of about 90 minutes. Therefore, a two-component UHU Plus Endfest 300 epoxy adhesive was chosen for this application.

Assembly process

Before assembling the plates, the pores and surfaces were thoroughly cleaned. A compressed air gun was used to unclog pores that were filled with residual molten material from the laser cut. The surfaces of the plates were then cleaned with acetone. In a jar, a 1:1 ratio of the epoxy binder and hardener was taken and thoroughly mixed. A thin layer of this mixture was then applied evenly on the surface of one test plate using a sponge roller. The second plate of the corresponding design was then placed over the first plate with careful consideration of their alignment. Any excess adhesive on the edges or surfaces was cleaned. Distributed weights and binder clips were placed on the plates and set aside for curing. The plates were allowed to cure for 24 hours to ensure a strong bond.

Adjustments

For accurate drag measurements, when test plates are placed inside the Hill, they should be perfectly flushed with the top surface. To ensure this, the thickness tolerance of the plates was checked. Some of the single plate designs were found to be less than 5 mm thick owing to the low tolerance of cast acrylics. The thickness of these plates was increased by placing spacers and metal strips along the edges on the bottom side. As these adjustments were placed along the edges, a small gap was created between the plate and the Hill. This gap is undesirable for porous plates as it would allow airflow through pores and alter their working mechanism. Therefore, the bottom surfaces of these plates were sealed using tape. Before performing measurements the test plate surfaces were cleaned with acetone and pores were unclogged using compressed air to remove unwanted particles.

3.7. Direct force measurements

Direct force measurement (DFM) is a method for measuring the total forces experienced by a specimen using force sensors like load cells. This technique has the advantage of determining the global drag characteristics of the specimen. On the other hand, it also measures unwanted forces like gravity, pressure from streamwise protrusions, mechanical losses and friction from surrounding surfaces (van Nesselrooij et al., 2022). To overcome this, a direct drag measurement device capable of measuring turbulent drag with low uncertainties was developed by van Nesselrooij et al. (2022). This device has been used for characterising the drag of micro-cavity arrays and grooves in this investigation.

3.7.1. Experimental setup

The experimental setup of the drag measurements is presented in this section. A description of the wind tunnel and drag measuring device is covered.

Wind tunnel

All experiments were performed in the M-Tunnel located at the Low-Speed Laboratory at TU Delft (Figure 3.11a). This is an open-circuit wind tunnel operated by a fan that reaches a maximum speed of 2900 RPM and a maximum freestream velocity of approximately 35 m/s. The maximum freestream turbulence intensity is about 0.7%. Figure 3.11b shows a schematic of the test section with a cross-section of 400 × 400 mm. The top surface and one side wall of the test section are made of transparent acrylic to provide optical access. About 600 mm in front of the leading edge of a test plate placed in the test section, a fresh turbulent boundary layer is created using a carborundum strip. The operation of the wind tunnel is controlled through LabView.

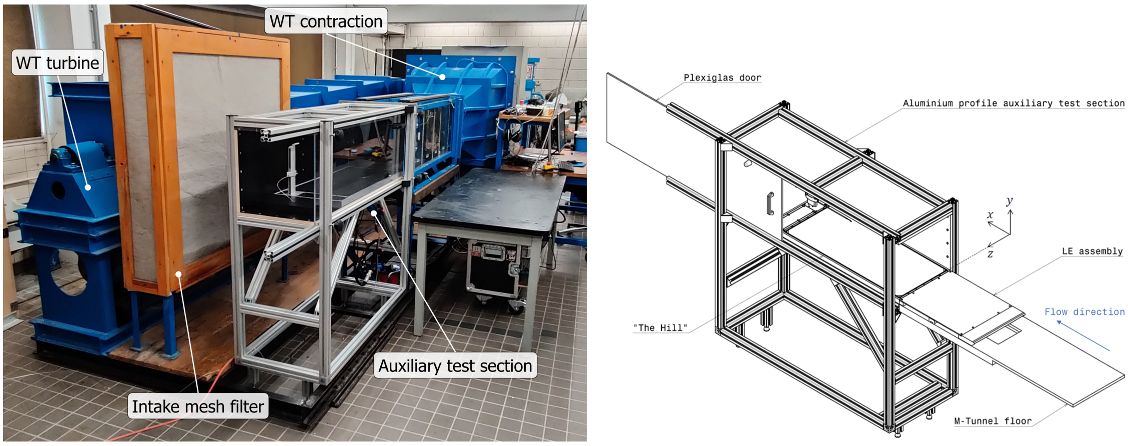

(a) (b)

Figure 3.11: The wind tunnel facility (Hartog, 2021) (a) Image of the open-circuit M-tunnel (b) Schematic representation of the test section with the Hill

Direct drag measurement device

Drag measurements were performed using an apparatus called 'The Hill' developed by Dimple Aerospace B.V. The device is capable of measuring turbulent drag over a flat surface with an uncertainty lower than 0.5% of CD and confidence of level of 95%. Measurement repeatability within 0.5% C_D was reported by van Nesselrooij et al. (2022) who investigated three test plates in two wind tunnels. Moreover, the system has been validated using riblets as a benchmark obtaining a match within 1% of C_D.

A detailed schematic of the device with all its components is shown in Figure 3.12. The Hill has a flexible architecture, making it suitable for wind tunnels with a minimum width of 400 mm. The core element of the device contains a connector tray that accepts test plates measuring 881.3 mm × 366.3 mm × 5 mm. A small air gap of 0.3 mm ± 0.1 mm is present along all the edges between the core and the connector tray to allow the test plate to swing freely. To monitor the pressure variations in the air gap, pressure taps are installed in it which are connected to four pressure scanners in the core. Any additional force caused by the gap is corrected from the overall force measured by the force sensor. A single wiring loom connects the core to a data acquisition system through an opening on the wind tunnel floor. The operation of the system is automatised making the measuring process efficient and easy. Forces are measured using a ME-systeme KD40S series force sensor which has a sampling frequency of 25kHz and range of ±2N. A data periscope containing a temperature and humidity sensor, a pitot tube and an automated traverse for hot-wire anemometry measurements is located downstream of the test plate. For an extensive description of all the components, specifications and working, refer to van Nesselrooij et al. (2022).

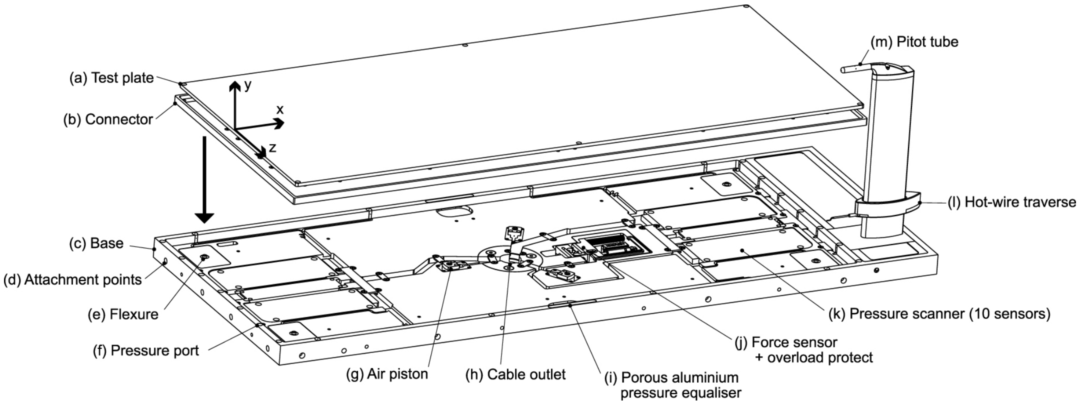

Figure 3.12: A detailed architecture of the drag measurement system with its components (van Nesselrooij et al., 2022)

3.7.2. Measurement plan

This section presents the measurement plan for the direct force measurements performed with the Hill. All the designs (refer Table 3.2) comprising 20 test plates were tested. A smooth aluminium plate named 'TP0000' was chosen as the reference plate. The drag measurements of all the designs were compared against this reference. To determine the effect of plate orientation on the drag forces, a couple of randomly chosen designs were also tested by rotating them by 180°. For an efficient measurement of all the designs, a 'triple sandwich' measurement sequence was adapted. The measurement of three test plates was sandwiched between two reference plate measurements, hence the name triple sandwich. The first run of this sequence was a warm-up which is typically performed at the beginning of the first sequence of the day for warming up the wind tunnel. For consequent sequences, the warm-up round was skipped. To check the repeatability of the measurements, each design was tested three times. This triple sandwich sequence is described in Table 3.4.

Table 3.4: The triple sandwich drag measurement sequence

Index	Measurement name	Test plate
0	Warm-up	TP0000
1	Reference	TP0000
2	Round 1	Design 1
	Round 1	Design 2
	Round 1	Design 3
3	Reference	TP0000
4	Round 2	Design 1
	Round 2	Design 2
	Round 2	Design 3
5	Reference	TP0000
6	Round 3	Design 1
	Round 3	Design 2
	Round 3	Design 3
7	Reference	TP0000

Each test starts and ends with a measurement performed at a 0 m/s free-stream velocity. In between, ten measurements are recorded from 25% to 100% of the wind tunnel's operational speed. This velocity sweep starting and ending with the zero measurements takes about 8 minutes after which the wind tunnel is cooled for 5 minutes before performing the next test. This 5-minute cooling window provides sufficient time for switching test plates. The measurement time of a triple sandwich sequence with a warm-up round is about three hours.

3.7.3. Data processing

During testing, three files are created into which the pressure, forces and ambient condition data are written. These files are processed using MATLAB scripts to determine ΔC_D which is the drag coefficient of the test plate with respect to the reference plate. The ΔC_D is computed as a function of Re_1, which is the Reynolds number based on a characteristic length of 1m. The unit Reynolds number is chosen to enable a comparison between different characteristic length scales. From ambient conditions data, the flow velocity and corresponding Re_1 are calculated using Buck's empirical relation for vapour pressure (Buck, 1981).

The drag coefficient is calculated by correcting for the pressure forces (F_p) and null force shifts (ΔF_{null}) that occur during measurement. Pressure forces are present on the streamwise facing gaps between the connector tray and core and are measured by the pressure taps located in them. The null force is the force measured at 0 m/s before and after the velocity sweep. Changes in the null force value occur due to the sensor's sensitivity to temperature and creep. The wind tunnel is allowed to cool for 5 minutes to minimise this effect. The final drag coefficient is calculated as shown in Equation (3.2), where q is the dynamic pressure and S is the surface area of the test plate which is 0.32 m^2.

$$C_D = \frac{F - F_p - \Delta F_{null}}{qS} \tag{3.2}$$

3.8. Particle Image Velocimetry

Several experimental and computational investigations performed by the research groups of Silvestri et al and Gowree and Scarano et al claimed that micro-cavity arrays reduced turbulence energy in the near-wall region by modifying the coherent structures leading to the reduction of skin friction drag. To validate these claims and expand our understanding on the flow physics of micro-cavity arrays in a turbulent boundary layer, flow characterisation experiments were performed using PIV.

Particle Image Velocimetry (PIV) is an optical and non-invasive method used to measure flow fields. It facilitates the quantitative mapping of instantaneous flow fields and the visualisation of flow structures. In principle, tracer particles that are small enough to follow the fluid motion are introduced into the flow and illuminated by a laser sheet along the plane of focus. The light scattered by the particles is captured using a high-speed camera in a pair of image frames with a small time separation. The image frames are divided into small regions called interrogation windows containing a few particle images. A cross-correlation analysis of each window between the two frames determines the displacement of the particle images. This displacement divided by the time separation between the laser light pulses and image magnification yields the local velocity of the fluid. This is repeated for the entire image frame, resulting in the mapping of the instantaneous flow field.

3.8.1. Experimental setup

The experimental setup of the PIV measurements is shown in Figure 3.13. The measurements were conducted at the M-Tunnel which is the same wind tunnel where the drag measurements were performed. The test plates were placed in the 'PHill' (PIV-Hill), a mount designed by Lai (2021) to replace the Hill. The PHill replicates the plate holder of the Hill and ensures that the flow conditions are similar to that of the drag measurements. As the depth of the PHill was larger than 5mm, spacers were placed below the test plates to ensure that they are flush with the leading edge mount. Images were captured with a LaVision sCMOS CLHS camera having a pixel size of 6.5 μm and a sensor size of 2560 px × 2160 px. The camera was attached to a three-axis mount which was fixed to traverse to allow the camera to move along the streamwise direction. A 105mm AF Micro Nikkor lens with an f# of 8 was used for all the measurements. The camera was vertically positioned at the same level as the surface of the test plate with a small upward tilt to minimise the averaging effect caused by the light incidence angle. The small upward tilt was necessary to cover the entire boundary layer of the flow. Images were recorded in a double-frame mode with an exposure time of 10 μs and calibrated using millimetric paper placed at the location of the laser sheet.

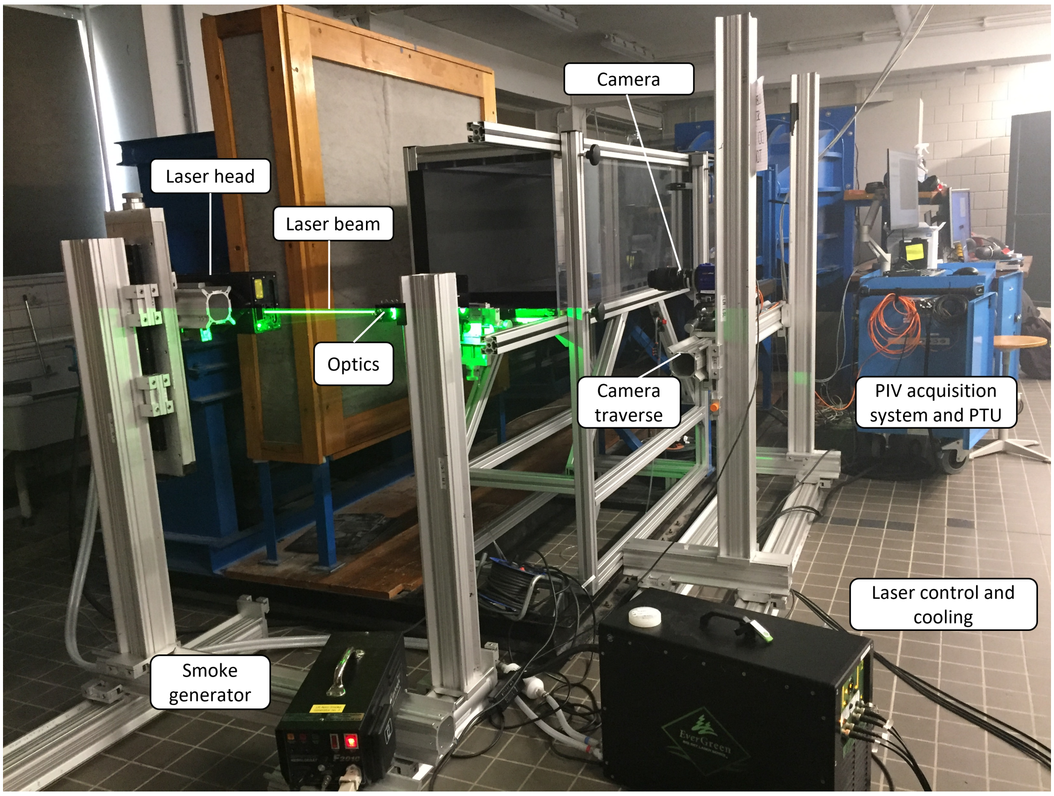

Figure 3.13: Experimental setup of the PIV measurements

The tracer particles were water-glycol based with a mean diameter of approximately 1μm. They were generated by a SAFEX Fog 2010+ smoke generator that was placed near the inlet of the wind tunnel. To ensure a consistent particle density in the test section, sufficient seeding is generated and allowed to stabilise for a few seconds just before that the start of the measurements. The particles were illuminated by a double-pulsed ND:Yag laser (Quantel Evergreen 200 laser) emitting a green light with a wavelength of 532 nm. The laser beam emitted from the laser head passes through an arrangement of mirrors and lenses as shown in Figure 3.14 to convert it into a sheet along the x-y plane with a thickness of 1.5 mm. The laser sheet extending into the test section is shown in Figure 3.15. The shooting of the laser pulses and triggering of the camera are controlled via a LaVision Programmable Timing Unit (PTU). The laser intensity, time separation between the image frames and image pairs, exposure time and a number of measurements were regulated using the DaVis software on a PIV acquisition system.

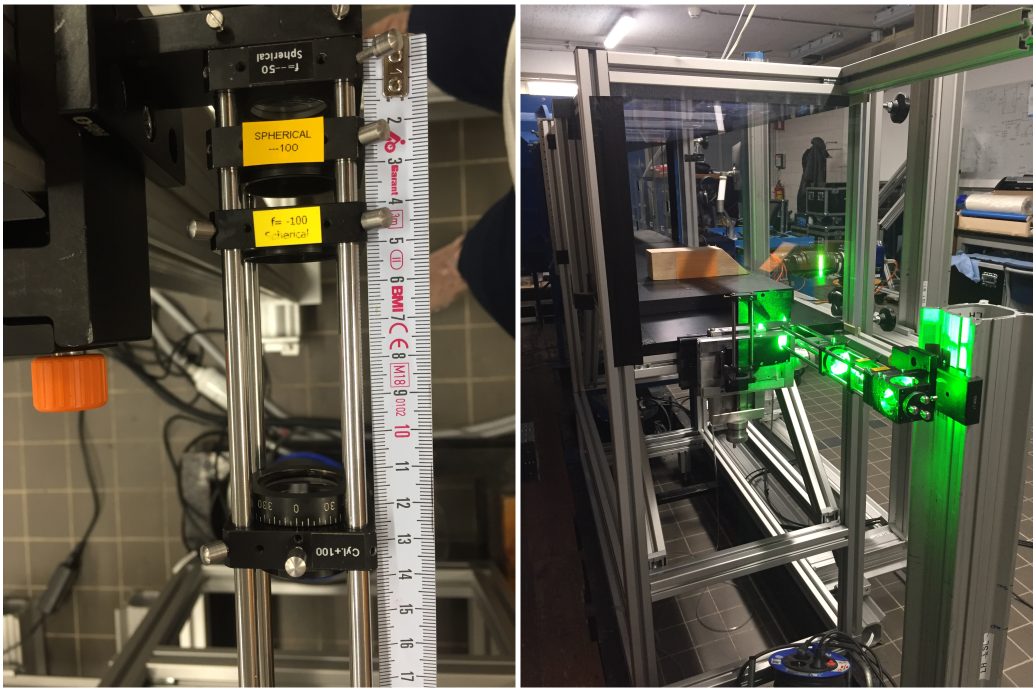

(a) (b)

Figure 3.14: Arrangement of lenses for the conversion of a laser beam into a wall-normal laser sheet

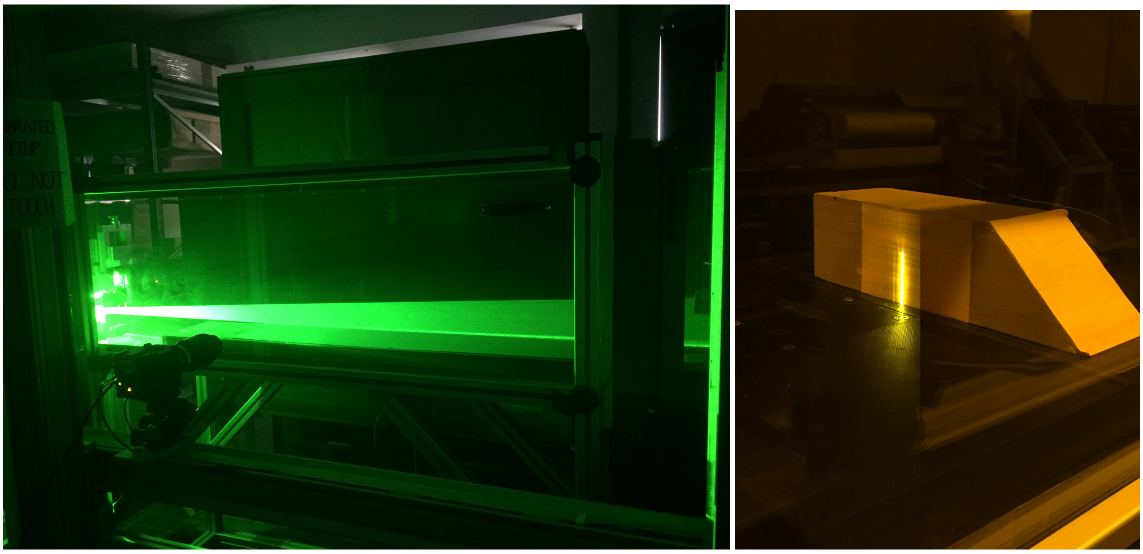

(a) (b)

Figure 3.15: A thin laser sheet along the centerline of the test plate

3.8.2. Measurement plan

With PIV measurements the attributes of the TBL that were analysed are the mean velocity profiles, velocity fluctuations, Reynolds stress and occurrence of turbulence events quantitatively and qualitatively. Based on the outcomes of the drag measurements, a few designs were selected for the analysis. For the PS-C design, measurements were performed at four locations (referred to as stations) as shown in Figure 3.16, to evaluate the effect of the micro-cavity array at different streamwise locations. For the remaining designs, the measurements were performed at the trailing edge of the test plates (S4) where the TBL is fully developed.

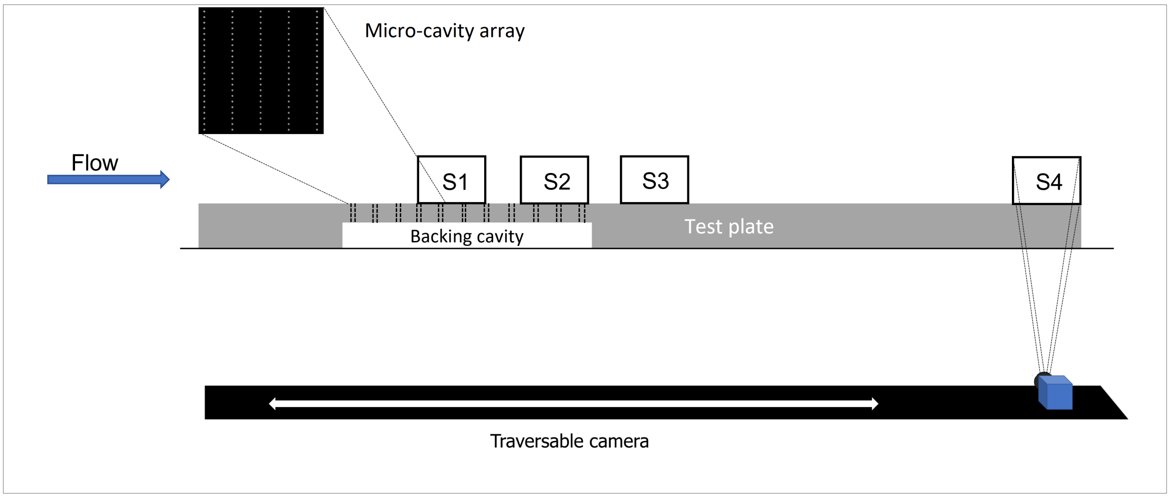

Figure 3.16: Schematic of PIV measurement locations along the streamwise direction (modified from Hartog (2021))

Measurements were performed at a freestream velocity of 14 m/s. The laser pulse separation time (Δt) was calculated based on the flow velocity and a particle displacement of 20 pixels per image pair. The camera trigger rate was chosen with the consideration that consecutive image pairs were uncorrelated. The main parameter of the PIV measurements is listed in Table 3.5.

Table 3.5: Measurement parameters for the PIV experiments

Measurement parameter		**x-y plane**
Laser sheet thickness	(mm)	1.5
FOV, w x h	(mm x mm)	50.05 x 32.37
Laser sheet location	(-)	Center-plane
F-stop, f#	(-)	8
Wind speed	(m/s)	14
Δt	(μs)	29
Trigger rate	(Hz)	30
Camera exposure time	(μs)	10
Resolution	(px/mm)	51.15
Particle displacement	(px/image pair)	20
No.of image pairs	(-)	600
No.of plates measured	(-)	9

3.8.3. Data processing

This section discusses the various steps involved in the processing of PIV data. The pre-processing of the images and computation of the velocity fields through cross-correlation were performed on LaVision DaVis 10.2 software. Post-processing of the velocity field data to extract the TBL characteristics was performed using MATLAB.

Pre-processing

The first step is the pre-processing of raw measurement images to make them suitable for subsequent processes. The surfaces of the black acrylic test plates were reflective; moreover, brighter reflections were produced by the edges of pores and grooves as shown in Figure 3.17a. To filter these reflections and background noise, a Butterworth high-pass filter with a filter length of seven images was applied to all the raw images. The filtering was effective in removing unwanted spots as shown in Figure 3.17b.

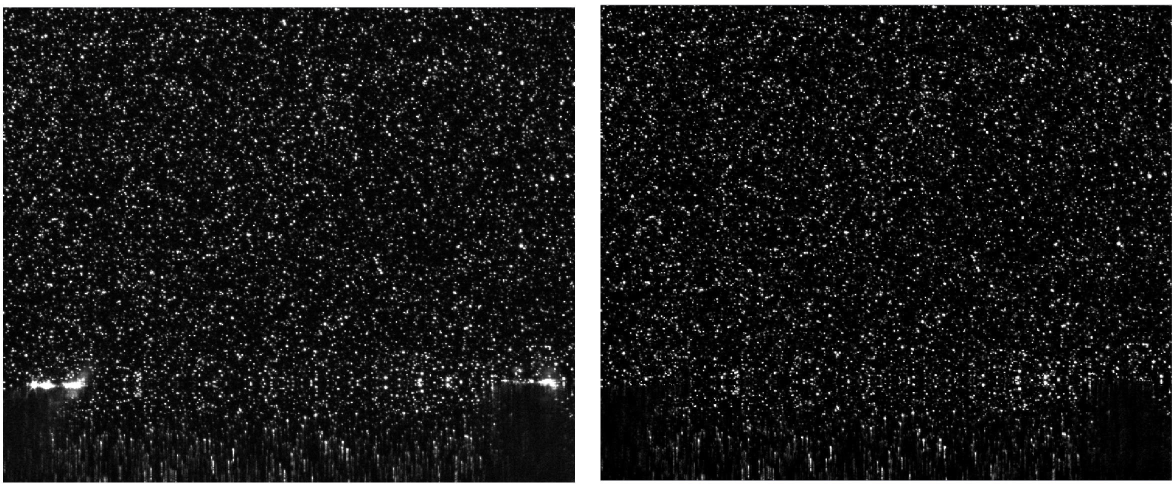
(a) (b)

Figure 3.17: Zoomed-in PIV image of a porous plate exported from DaVis (a) Raw image with noise and reflections (b) Filtered image

Cross-correlation

Cross-correlation is a statistical method applied to the filtered images to compute the local displacement vectors of particle images. The images are first partitioned into small interrogation windows containing at least ten particles. A cross-correlation analysis is performed between the corresponding windows of the two image frames. This produces a cross-correlation map in which the peak's distance from the origin determines the mean particle image displacement. The local velocity is computed by dividing the displacement by the laser pulse separation time and magnification. A sequence of these steps is illustrated in Figure 3.18.

To determine the appropriate settings for interrogation windows, Hartog (2021) performed an elaborate benchmark test with various combinations of window sizes, shapes and overlap ratios. As a similar setup, measurement plane and location were used in the current experiments, a validation of a few settings was performed. The target was to achieve images with high detail and low noise. The test cases and results can be found in Appendix B. The settings that were finalised for the cross-correlation analysis are listed in Table 3.6. An example of the instantaneous velocity field computed using cross-correlation is shown in Figure 3.19a. It is evident that the FOV covers the entire boundary layer as the velocity at the top region is equal to the freestream velocity. Moreover, the flow structures have been computed with sufficient detail without the presence of grainy structures that are typically introduced by high levels of noise. Figure 3.19b shows the mean velocity field computed from 600 images. The mean field is observed to be smooth indicating a good convergence of the results. In both images, the horizontal region with the lowest velocity indicates the surface of the test plate. The pores on the plate are visible as bumps in the mean velocity field plot.

Table 3.6: Cross-correlation settings

Initial pass	
Window size	96 × 96
Window shape	Elliptical 2:1
Overlap	75%
Number of passes	1
Final pass	
Window size	16 × 16
Window shape	Elliptical 2:1
Overlap	75%
Number of passes	2
Maximum expected particle displacement (px)	22
Geometric mask	Off

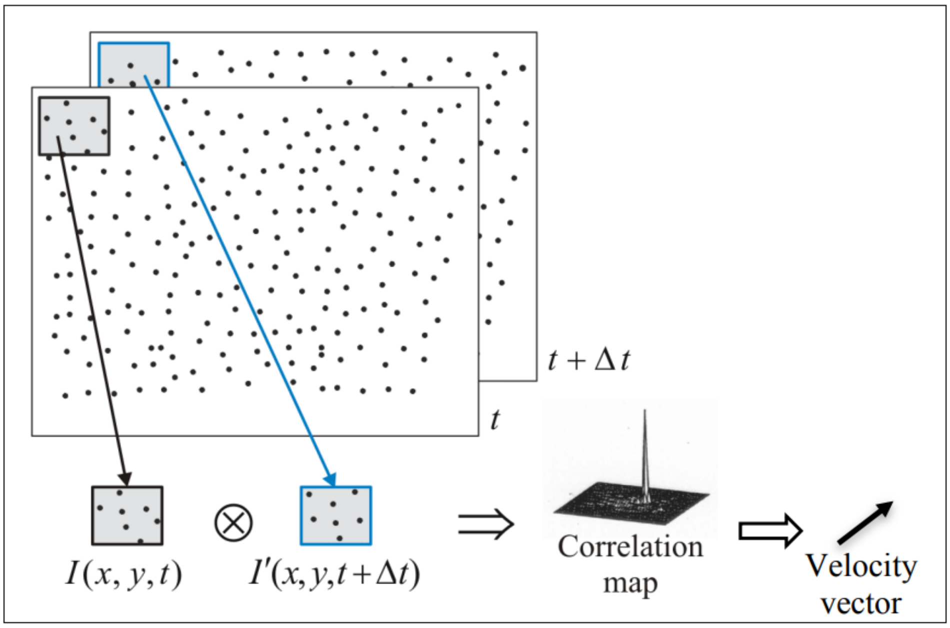

Figure 3.18: Schematic of the sequence of processes in the computation of the instantaneous flow field (Scarano, 2013))

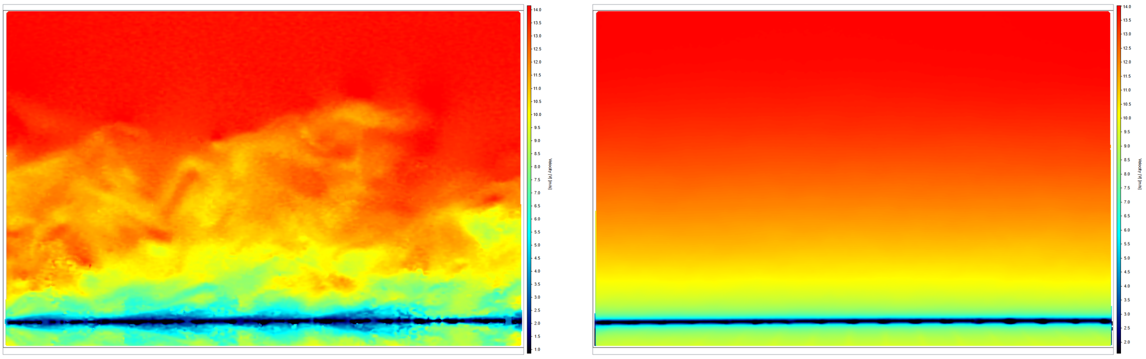

(a) (b)

Figure 3.19: Results of cross-correlation exported from DaVis, flow is from left to right (a) Instantaneous velocity field (b) Mean velocity field

Post-processing

The vector field data were exported from DaVis and further processed in MATLAB for quantitative analysis of the boundary layer. Techniques used for the computation of boundary layer profiles and the detection of turbulence events are discussed in this section. In the PIV experiments, a cavity was present under the test plates as they were raised using spacers. This may have interfered with the performance of the PN-B, PS-C and PC-R designs as the underside of these test plates was not sealed.

Boundary layer profiles

The steps for the computation of the boundary layer profiles of mean velocities, velocity fluctuations and Reynolds stress are given below. The MATLAB codes for the following processes were primarily formulated by Hartog (2021) which were then modified to suit the requirements of the current work.

- Export vector field data from DaVis: Mean streamwise and wall-normal velocities, standard deviations of the mean velocities and Reynolds stress.
- Store data in the form of matrices

- Estimate the wall location over the entire FOV by determining the point of minimum mean velocity at every streamwise coordinate and then smoothening the wall profile by applying a double sliding median and fitting a third-degree polynomial.

- Correct for the horizontal tilt in the wall by projecting the boundary layer profile at every x coordinate onto a new vector with the y location of the wall estimate being the first point.

- Apply this correction to all the data matrices such that all data below the estimated wall is removed.

- Perform spatial averaging over selected streamwise locations in the FOV (or the entire FOV) to compute the wall-normal profiles. Averaging over specific streamwise locations was implemented in scenarios where reflections were present in the FOV.

- Calculate boundary layer parameters: boundary layer thickness (δ), displacement thickness (δ^*), momentum thickness (θ) and shape factor(H).

- Estimate friction velocity (u_τ) by performing boundary layer fitting using a method adapted from Rodríguez-López et al. (2015) called the composite method. This method was chosen after an assessment with Clauser's and Spalding's methods. The composite method was observed to fit the largest region of the velocity profile in comparison to Clauser's and Spalding's methods. Moreover, the composite fit is not influenced by the biases in the near-wall region. Compute the skin friction coefficient C_f using the following expression,

$$C_f = 2\left(\frac{u_\tau}{U_\infty}\right)^2. \tag{3.3}$$

- Plot the normalised boundary layer profiles.

VITA analysis

The Variable Interval Time Averaging (VITA) technique was initially formulated by Blackwelder and Kaplan (1976) for detecting the bursting phenomenon in the near-wall region. The algorithm looks for sweeps and ejections which are the events driving bursts. As these events are associated with velocity fluctuations, detections are made by analysing streamwise fluctuations within a time window that is of the order of the time scale of the events. The appropriate time window reported by Blackwelder and Kaplan (1976) and also used by Silvestri et al. (2017a) is $T_w^+ = 10$ which corresponds to about 400 to 600 μs (using the conditions of this work). In the PIV experiments, the minimum separation time between image pairs in order to obtain uncorrelated images at freestream velocity of 14 m/s is 3600 μs which is very large for the detection for the events. Therefore, instead of using temporal data, spatial data was used for the VITA analysis owing to Taylor's hypothesis (Taylor, 1938) which related the temporal and spatial characteristics of turbulence.

Firstly, time separation between adjacent streamwise locations was computed using the local velocity. The number of streamwise samples required to obtain $T_w^+ = 10$ was estimated. An example is shown in Figure 3.20, where the spatial domain at 'x' distance from the is divided into 4 sets each containing 6 sample points (these values are chosen for representation purposes only).

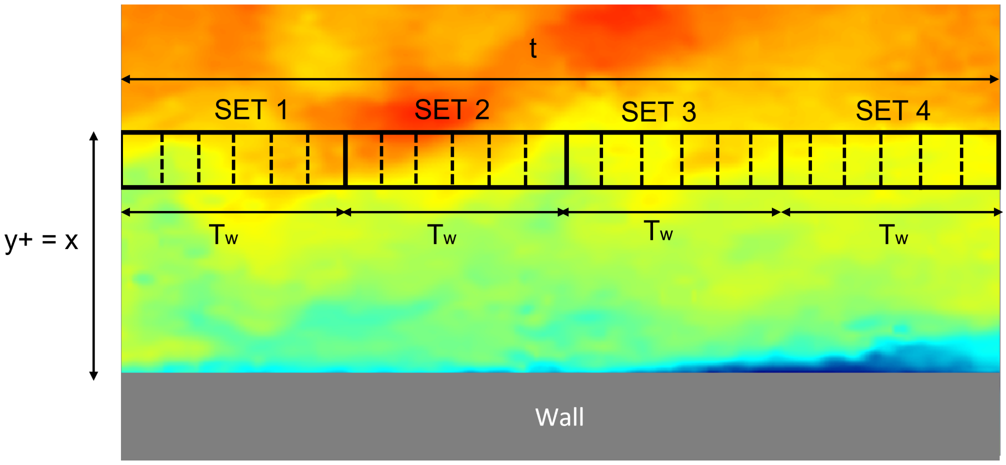

Figure 3.20: Schematic of the spatial data sets used for the VITA analysis

The VITA of a fluctuating velocity signal u(t) is estimated using the following expression,

$$\hat{u}(t, T_w) = \frac{1}{T_w} \int_{t-\frac{1}{2}T_w}^{t+\frac{1}{2}T_w} u(t)dt \tag{3.4}$$

The local turbulent energy is obtained by calculating the variance of one set,

$$\text{Var}(t, T_w) = \hat{u}^2(t, T_w) - [\hat{u}(t, T_w)]^2 \tag{3.5}$$

Next, the variance of the entire signal is calculated as follows,

$$Var(t) = \lim_{t \to \infty} \frac{1}{t} \int_0^t u^2(t)dt \tag{3.6}$$

A detection function is defined such that

$$D(t) = \begin{cases} 1 & \text{if Var}(t, T_w) > kVar(t) \\ 0 & \text{otherwise} \end{cases} \tag{3.7}$$

where k is a threshold level to detect bursts. A threshold value of 1.2 (Blackwelder and Kaplan, 1976)was used to filter out the outer region turbulent activity and capture the bursts occurring in the near-wall region. To distinguish between sweep and ejection events, Whalley (2011) defined the following detection function

$$D(t) = \begin{cases} 1 & \text{if Var}(t, T_w) > kVar(t) \text{ and } \frac{du}{dt} > 0 \text{ sweep event} \\ 0 & \text{if Var}(t, T_w) < kVar(t) \text{ no event} \\ -1 & \text{if Var}(t, T_w) > kVar(t) \text{ and } \frac{du}{dt} < 0 \text{ ejection event} \end{cases} \tag{3.8}$$

This process was repeated at every wall-normal location in the velocity field for every image. The total number of turbulence events that occurred during the measurement of each test plate was determined.

4

Results and discussion

The results of the direct force measurements and PIV experiments are presented and discussed in this chapter. Section 4.1 presents the drag performance of the test plates followed by a discussion of the results in Section 4.2. The PIV results are given in Section 4.3 followed by a discussion in Section 4.4.

4.1. Drag performance of test plates

The drag results are presented in terms of ΔC_D (%), which is the difference in drag coefficient with respect to the smooth reference plate expressed in percentage. The data supporting the estimation of ΔC_D like drag coefficient values, null force and pressure drag corrections and uncertainty of ΔC_D in a measurement set are presented for one design set in this chapter. For the remaining designs, the data can be found in Appendix A. The second measurement point has been omitted in the ΔC_D plots as the results for most designs contained outliers which is believed to be caused by resonance.

4.1.1. Silvestri's pore designs

The drag results of Silvestri's designs excluding PS-C are shown in Figure 4.1. It is evident that the drag produced by all three designs is higher than the drag of a smooth reference (Figure 4.1a). The drag is also observed to increase with increasing pore size. The drag increase produced by the designs with small (D = 1.2 mm) and medium (D = 1.8 mm) pores are about 1% and 2% respectively and remain nearly constant at all measured Reynolds numbers except the lowest where they are slightly less. However, ΔC_D of the largest pore design (D = 2.5 mm) increases with increasing Reynolds number, from about 1% to 5.5%. Figure 4.1b shows a similar trend where C_D of the largest pore design is highest and its difference with the reference increases with increasing Re_1. In general, C_D shows a decreasing trend with increasing Re_1.

The null force correction is less than 0.2% (Figure 4.1c) indicating no anomalies with the measurements of the force sensor. The pressure drag correction shown in Figure 4.1d ranges between 1% to 5% which is within acceptable limits. The RMSE of the designs (Figure 4.1e) is about 2% at low velocities and reduces below 1% at high velocities, indicating good measurement repeatability and confidence in the results.

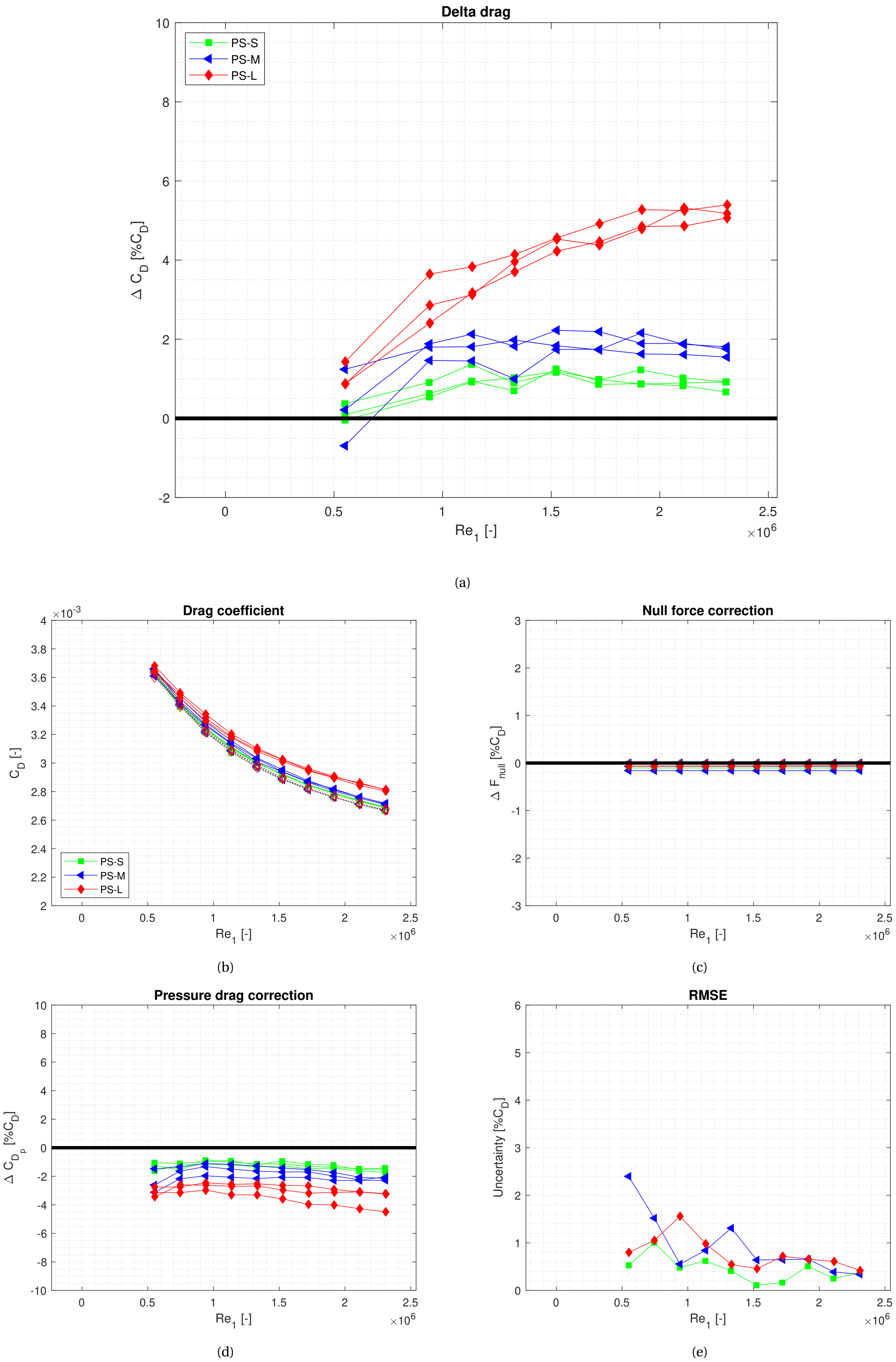

(a)

(b)

(c)

(d)

(e)

Figure 4.1: Drag measurement results for Silvestri's pore designs (a) Change in drag coefficient w.r.t reference plate (b) Drag coefficient, dotted lines: smooth reference plate (c) Null force shift corrections (d) Gap pressure drag corrections (e) Uncertainty of measurement set determined as RMSE

4.1.2. New pore designs

The drag results of the new pore designs are discussed in this section under two categories: size and alignment of the pores and pore spacing. In both categories, the results are compared with the baseline plate as the design parameters were modified with respect to the baseline design.

Pore size and configuration

Figure 4.2a shows that drag produced by the new pore designs in this category is higher than the smooth reference plate. The baseline produces a ΔC_D of about 1%. The ΔC_D of the design with smaller pore depth is slightly less than the baseline; however, the difference in their C_D values is negligible. Changing the configuration of pores from inline to staggered does not significantly alter the ΔC_D except at the highest Re_1 which is an outlier. A similar outlier is present for the large pore design which is thought to have been caused due to wind tunnel vibrations and resonance. The vibration caused at the highest fan speed might not have been sufficiently damped by the measurement device. The ΔC_D of the large pores has an increasing trend and is also higher than the other designs.

Pore spacing

The effect of pore spacing on the drag performance of a porous plate is shown in Figure 4.2b. The design with medium streamwise spacing produces a lower ΔC_D than the baseline which reaches a maximum of 1.5% at the highest Re_1. At this point, the ΔC_D produces a 0.5% drag reduction w.r.t the reference. However, this reduction is too low and does not reflect a significant result in their C_D values. Reducing the streamwise spacing further results in the production of higher drag. The C_D of the small streamwise spacing is significantly higher than the reference thereby resulting in a higher ΔC_D. As observed earlier, the last measurement point is an outlier. The design with a higher spanwise spacing shows a slightly lower ΔC_D than the baseline, but this difference is negligible in their C_D values.

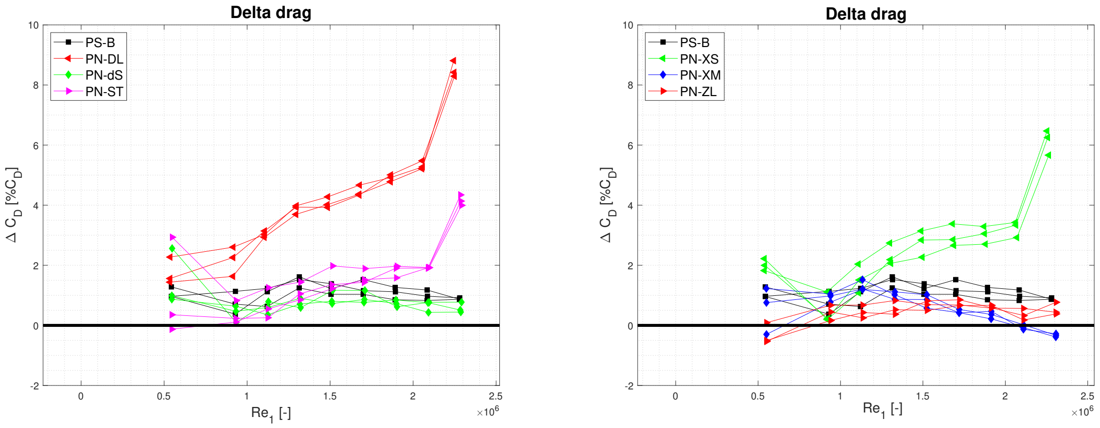

(a) (b)

Figure 4.2: Comparison of change in drag coefficient w.r.t reference plate for new designs (a) Pore size and configuration (b) Streamwise and spanwise pore spacing

4.1.3. New backing cavity designs

Figure 4.3 presents the influence of backing cavities on the drag performance of porous plates. As the backing cavities are placed below a porous plate of 2mm thickness, the drag results are compared with the PN-dS plate which has the same porous top plate but backed by a smooth plate. As observed earlier, the drag increase of PN-dS is similar to that of the baseline. Contrary to expectations, all backing cavity designs produce a higher ΔC_D than PN-dS. A dip in ΔC_D is produced by the PC-R design at the second measurement point but as the RMSE is higher in comparison to the other measurement points, this is thought to be a measurement error. The streamwise and spanwise aligned backing cavities have a similar drag performance which is in general higher than the rectangular design.

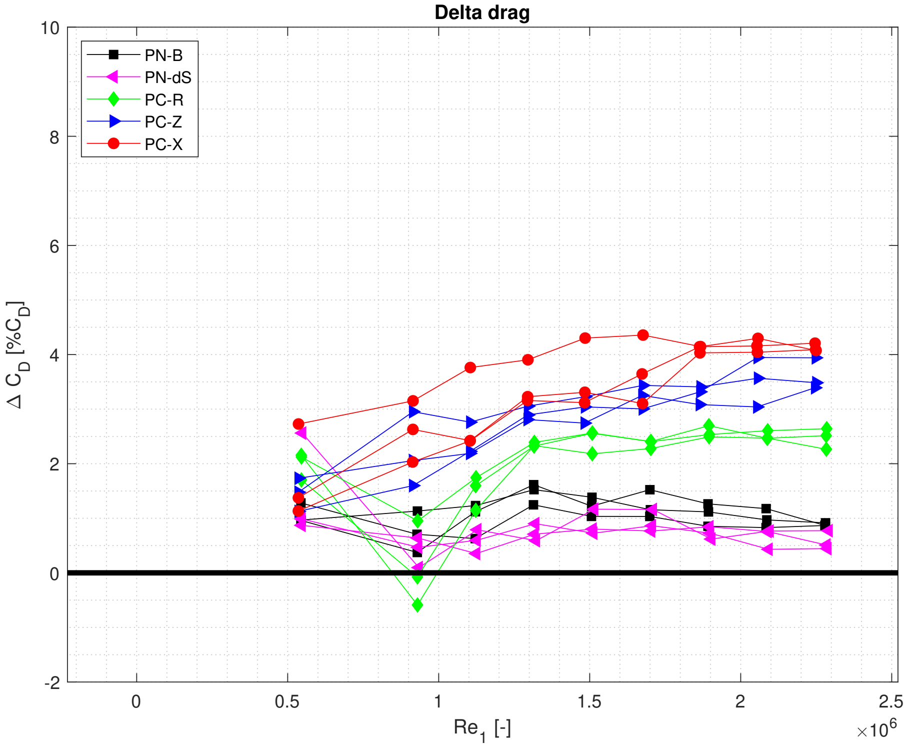

Figure 4.3: Comparison of change in drag coefficient w.r.t reference plate for new backing cavity designs

4.1.4. Permeable trailing edge designs

The drag performance of the permeable trailing edge designs that were studied by Rubio Carpio et al. (2020) for noise reduction is shown in Figure 4.4. As all these designs have a staggered pore configuration, they are compared with the new staggered design PN-ST, which has the same pore dimensions but a larger spacing than PA-L. All the designs show an increased drag performance w.r.t the smooth reference. A grouping in results is observed wherein the small and medium spaced designs have a ΔC_D of 3 to 4% and the larger spaced designs have a 1% ΔC_D. The pore spacing which is directly linked to the porosity of the design plays a crucial role in its drag performance. As previously seen, the last measurement point of PN-ST is an anomaly caused by wind tunnel vibrations.

4.1.5. New groove designs

The drag performance of the different groove designs is shown in Figure 4.5. The results show that all the designs produce a higher drag than the smooth reference. Their ΔC_D is also observed to be higher than the baseline porous design. Although the design of G-S was based on the design of PN-B, there is no correlation between the drag performance of both designs. The G-M design produces the closest result to PN-B but this is believed to be caused due to the lower number of grooves.

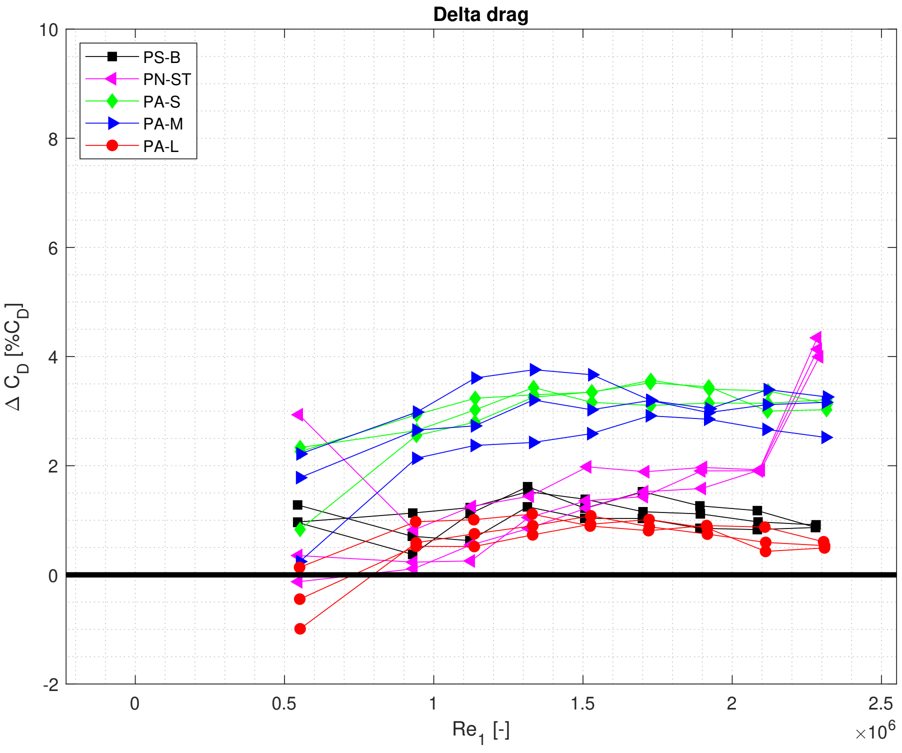

Figure 4.4: Comparison of change in drag coefficient w.r.t reference plate for permeable trailing edge designs

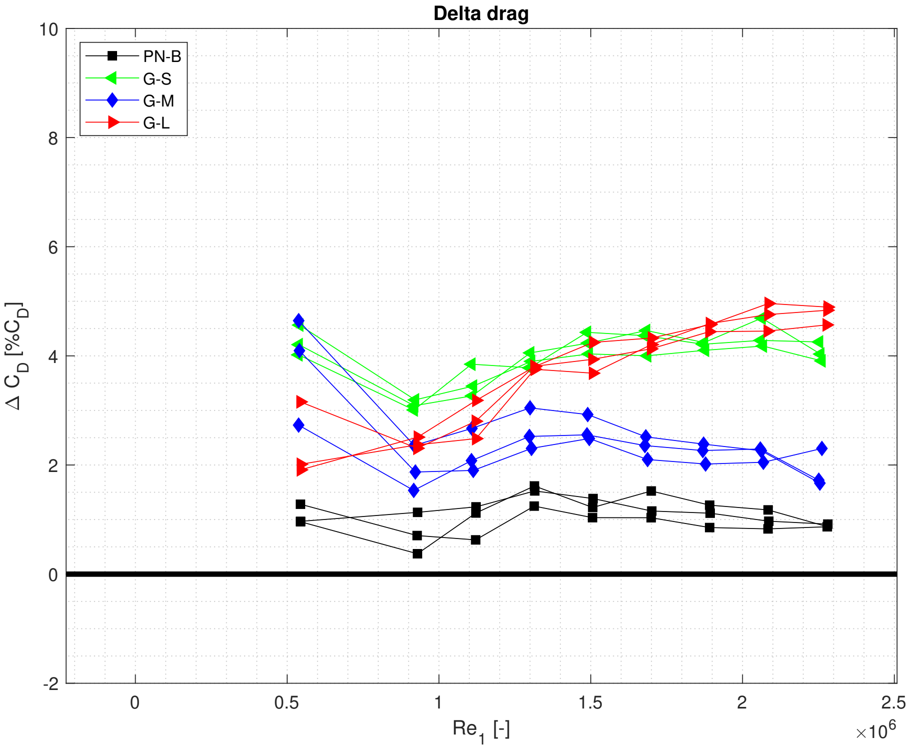

Figure 4.5: Comparison of change in drag coefficient w.r.t reference plate for groove designs

4.2. Discussion on drag results

This section presents a discussion of the DFM. Unfortunately, none of the designs produced any significant drag reductions within the tested conditions. The following have been identified as potential causes for the observed drag increase.

Pressure drag

A closed-type flow is a cavity flow phenomenon in which flow separates at the upstream edge of a cavity resulting in the formation of a shear layer which enters the cavity and impinges on the downstream wall. This increases pressure forces on the wall resulting in pressure drag. In the current scenario, the drag increase produced by the test plates is caused by the pressure drag acting inside the pores and grooves. This is notable by the increasing drag trend with increasing porosity of the micro-cavity array as shown in Figure 4.6a. This trend is present for both the staggered and aligned configurations, however the difference in drag values is attributed to flow interactions between pores. Porosity is directly proportional to pore diameter and the number of pores. As the pore diameter increases, more flow is allowed to enter the pore which increases the pressure drag. Gerhold et al. (2016) and Howerton and Jones (2015) investigated the drag of acoustic liners and made similar observations; drag increases with increasing hole diameter.

The porous plates with staggered configurations have the same pore diameter but varied spacings. For these designs, drag increases with decreasing spacing which increases their porosity (Figure 4.6a). As the size of the test plate is fixed, decreasing the pore spacing increases the total number of pores which causes the pressure drag to increase. A similar trend has been reported by Wilkinson (1983) and Gerhold et al. (2016) with acoustic liners. The drag produced by the groove plates is also caused by the pressure forces acting on the downstream walls inside the grooves. The G-L and G-S designs produce higher drag as they have a larger area exposed to the flow entering the groove compared to the G-M design (Figure 4.5).

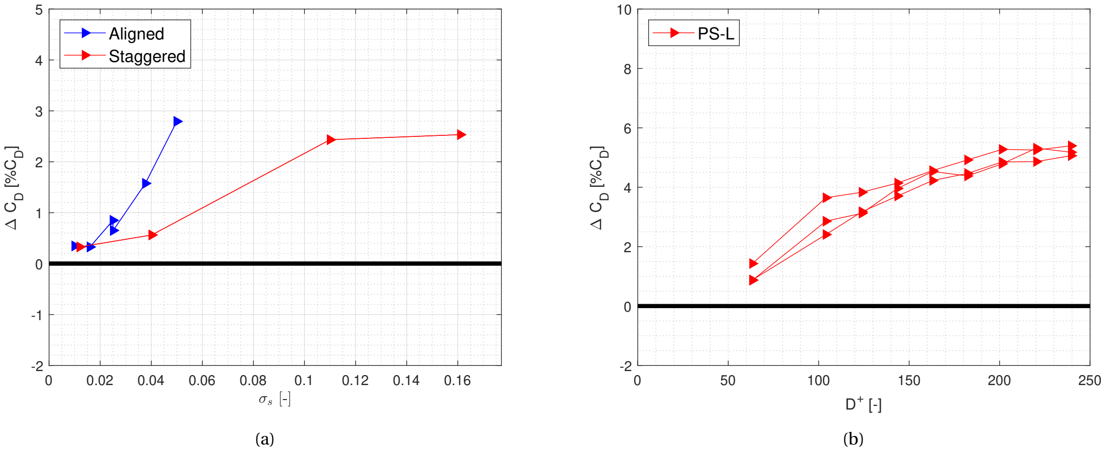

(a) (b)

Figure 4.6: Trends in ΔC_D, (a) ΔC_D versus porosity for designs with aligned and staggered pore configuration, denoted ΔC_D correspond to values at free-stream velocity of 14 m/s (b) ΔC_D versus pore diameter in viscous units for the PS-L design

Production of turbulence energy

Another phenomenon that contributes to drag is an increase in the production of turbulence energy in the presence of surface modifications and backing cavities. The processes leading to turbulence energy production are: the breaking of the shear layer traversing the pores and the wall-blowing action created by the backing cavities. Silvestri et al. (2017a) in an investigation of the performance of micro-cavity arrays with different pore sizes concluded that pores with $D^+ > 145$ cause the shear layer to break apart. For the PS-L design, its D^+ ranges from 60 to 240 with increasing flow speed which causes a significant increase in drag as shown in Figure 4.6b. The drag rise at higher Re_1 could be caused by the increased production of turbulence energy as the optimum threshold of D^+ is exceeded.

The action of wall-blowing is known to destabilise the turbulent boundary layer (Burden, 1969; Kametani et al., 2015) as it interacts with the coherent structures and interrupts the burst-sweep cycle. Investigations on controlled wall-blowing by Choi et al. (1994) and Spangler (1966) have shown the potential to reduce skin friction drag but in this case, the phenomenon is random thereby disruptive to the near-wall flow. Wall-blowing is caused by the backing cavities as it is capable of holding and redistribution a part of the air that enters through the pores. This phenomenon has been observed through PIV experiments (see **??**) which is discussed in the following section. The streamwise aligned cavities have a larger volume due to their orientation; thus the PC-X design produces higher drag. Conversely, the PC-R design has backing cavities with smaller volumes and produces lower drag.

Interaction with low-speed streaks

As stipulated by the design guidelines of micro-cavity arrays, the spacing between pores is crucial for effectively disrupting the low-speed streaks. The designs that were dedicated to studying the effect of spacing on the performance of the micro-cavity array showed some specific drag trends (Figure 4.2b). PN-XM with a streamwise spacing that is half of PS-B (designed according to the guidelines) showed a similar drag performance as PS-B. However, a further reduction in streamwise spacing (PN-XS) caused an increase in drag. In addition to larger pressure drag from the increased number of pores, a chaotic disruption of the low-speed streaks by the closely spaced pores could contribute to the extra drag. Increasing the spanwise spacing beyond the minimum recommended value as in PN-XL shows a slightly lower drag than PS-B. Although this drag reduction is insignificant due to its low values, it is possible that a higher spanwise spacing produces lower drag. A few designs were selected based on their drag performance and their influence on the turbulent flow field were analysed.

4.3. PIV results

This section presents and discusses the results of the PIV experiments. Section 4.3.1 discusses the quality of the PIV data, Section 4.3.2 presents the turbulent boundary analysis of the test plates and finally, a discussion of the results are presented in Section 4.4.

4.3.1. Data quality assessment

Assessing the quality of data is crucial for determining the validity and reliability of the experimental measurements. This section discusses uncertainties in the results computed from PIV measurements and the effects of data averaging.

Uncertainty quantification

Uncertainty determines the range of the measurement error. The uncertainty of the instantaneous velocity is defined as shown in Equation (4.1) in which the pixel correlation error $\epsilon_{\mathrm{corr}} = 0.1$ (Raffel et al., 1998).

$$\epsilon_u = \epsilon_{\mathrm{corr}} \frac{\Delta x_{px}}{\Delta t} \tag{4.1}$$

Uncertainties of the mean velocity, standard deviations and Reynolds stresses were computed using the following relations (Benedict and Gould, 1996) at every coordinate location in the FOV. N denotes the total number of sample points which in this case is the number of image pairs and is equal to 600.

$$\epsilon_{\overline{u}} = \frac{\sigma_{\mathrm{u}}}{\sqrt{N}} \tag{4.2}$$

$$\epsilon_{u'} = \frac{\sigma_{\mathrm{u}}}{\sqrt{2(N-1)}} \tag{4.3}$$

$$\epsilon_{R_{xy}} = \sigma_{\mathrm{u}}\sigma_{\mathrm{v}}\sqrt{\frac{1+\rho_{uv}^2}{N-1}} \tag{4.4}$$

where ρ_{uv} is the cross-correlation coefficient and is computed as follows,

$$\rho_{uv} = \frac{\overline{u'v'}}{\sigma_u \sigma_v}$$

Boundary layer profiles were calculated through a spatial averaging of the streamwise coordinates within a selected region of the entire FOV. The uncertainty of spatially averaged profiles is decreased proportionally to the inverse of the square root of the number of uncorrelated data points (Sciacchitano and Wieneke, 2016). As the data was processed with a 75% overlap of the interrogation windows, every fourth data point in the streamwise direction is uncorrelated. Therefore, the uncertainty of spatially averaged data is computed as follows,

$$\epsilon_T = \frac{\frac{1}{N_x/4}\sum_{\xi=1}^{N_x} \epsilon_T(\xi)}{\sqrt{N_x/4}} \quad \text{with} \quad \xi = \{x(1), x(5), ..., x(N_x-3)\} \tag{4.5}$$

where N_x denotes the number of streamwise coordinate points in the FOV.

The uncertainty of mean velocity and turbulent statistics of all the test plates at freestream velocity of 14 m/s is presented in Table 4.1. In general, the uncertainties are all less than 1% with respect to their corresponding local values. The change in uncertainties with different test plates is also observed to be low. Thus, this provides high confidence in the measurement data.

Table 4.1: Mean uncertainties of the spatially averaged wall-normal profiles at U_∞ = 14 m/s. Values are represented in percentages calculated with respect to the corresponding local value.

Plate name	ϵ_u (m/s)	$\epsilon_{\overline{u}}$ (%)	ϵ_{σ_u} (%)	ϵ_{σ_v} (%)	$\epsilon_{\overline{u'v'}}$ (%)
Reference: S1	0.067	0.17	0.12	0.08	0.15
Reference: S2	0.067	0.17	0.12	0.08	0.15
Reference: S3	0.067	0.17	0.12	0.08	0.15
Reference: S4	0.067	0.21	0.15	0.09	0.14
PS-C: S1	0.067	0.16	0.11	0.07	0.15
PS-C: S2	0.067	0.16	0.11	0.07	0.15
PS-C: S3	0.067	0.16	0.12	0.07	0.15
PS-C: S4	0.067	0.20	0.14	0.09	0.13
PN-B: open base	0.067	0.23	0.16	0.10	0.16
PN-B: closed base	0.067	0.21	0.15	0.09	0.15
PN-DL	0.067	0.21	0.15	0.09	0.14
PN-XS	0.067	0.21	0.15	0.09	0.14
PN-dS	0.067	0.21	0.15	0.09	0.14
PN-ST	0.067	0.21	0.15	0.09	0.14
PC-R: open base	0.067	0.23	0.16	0.10	0.17
PC-R: closed base	0.067	0.21	0.15	0.09	0.15
G-S	0.067	0.21	0.15	0.09	0.14
G-M	0.067	0.21	0.15	0.09	0.14

Averaging effects

Averaging of data can lead to erroneous results in the near-wall region of the turbulent boundary layer due to high velocity gradients. Data averaging is caused by the finite size of the interrogation windows and the finite thickness of the laser sheet. In the first case, computation of the resultant velocity vector is performed by averaging the data in the interrogation window. The second effect is a result of the camera tilt in the near-wall region. As the camera is tilted upwards, the incidence light forms a non-horizontal optical path through the laser sheet over which data is averaged.

Hartog (2021) developed a method for analysing these effects by creating two biased velocity profiles. The first profile is created by applying only the window averaging effects to the fitted profile and the second profile is created by including the effect of the camera tilt. Based on the distance of the camera from the laser sheet and the height of the FOV, the tilt angle was estimated to be 0.48°. The averaging effects were investigated for two designs; smooth reference and PN-XS and the results are shown in Figure 4.7. In both cases, the window averaging effect and the total averaging effect profiles are identical and coincide with the fitted profile beyond y^+=10. This means that the averaging effects are negligible in this region. Below y^+=10, the averaging profiles deviate from the fitted profile with the largest deviation being at the point closest to the wall. Here, the bias is large as the velocity gradients are higher. The underestimation of velocity in this region is also caused by the loss of data due to reflections. Overall, the averaging effects are prominent in the near-wall region and do not affect the results beyond y^+=10.

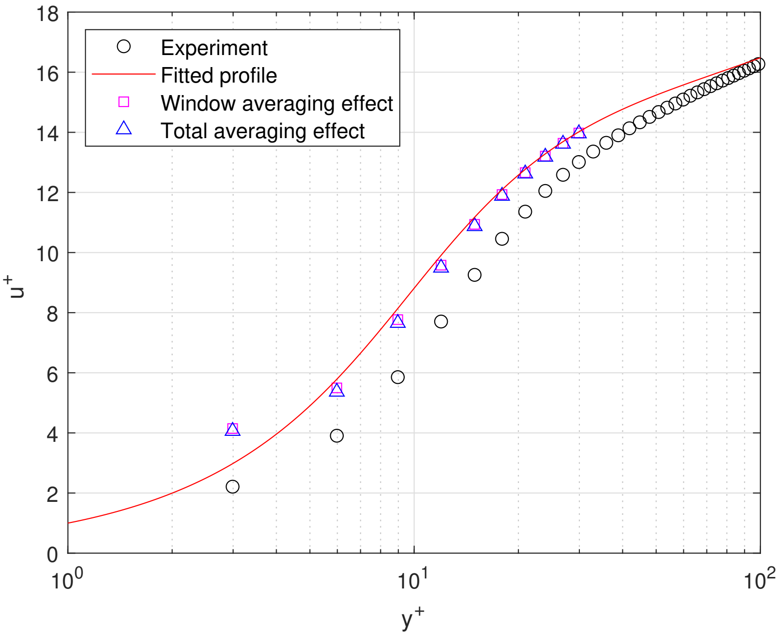

(a)

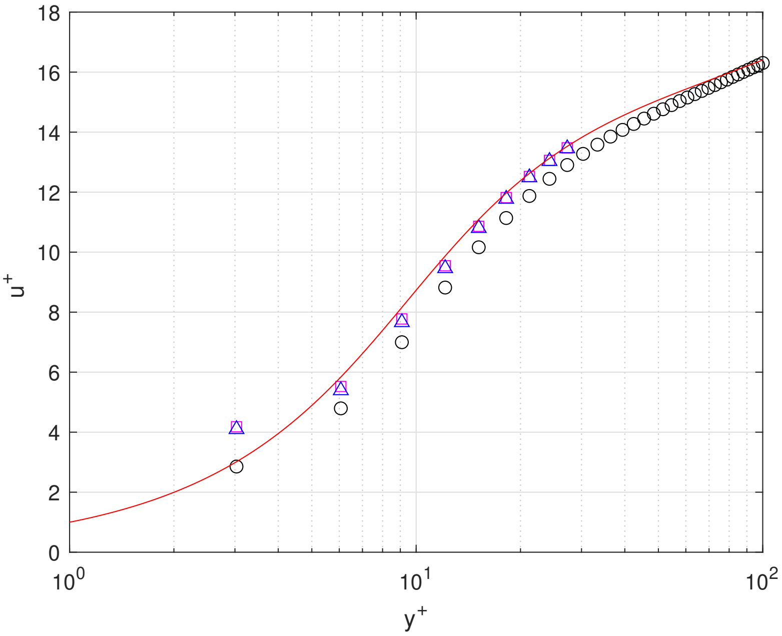

(b)

Figure 4.7: Averaging effects on the PIV data (a) Smooth reference (b) PN-XS design

4.3.2. Turbulent boundary layer analysis

This section discusses various characteristics of the turbulent boundary layer over the test plates; boundary layer profiles of mean velocity, streamwise and wall-normal fluctuations and Reynolds stress and the occurrence of turbulence events. The boundary layer profiles of each design are compared with the smooth reference and DNS data by Schlatter and Örlü (2010). The DNS data is included to validate the measured results. In general, the PIV profiles show a good agreement with the DNS data except very close to the wall. This could be caused by the near-wall averaging effects. The burst profiles indicate the number of sweep and ejection events occurring within y^+=100. Detection of the turbulence events was achieved using the VITA technique. The results of selective designs are presented and discussed here. The results of the remaining designs can be found in Appendix C.

PN-B: open base vs closed base

The PN-B baseline design was tested under two conditions and the results are compared in this section. The first condition is with the base of the plate mount (PHill) open. In this scenario, the flow above the plate is at U_∞ = 14 m/s and below the plate is ambient. The second condition is with the base of the PHill closed, which results in the formation of a single large cavity beneath the test plate as it is raised with spacers. Airflow through the cavity occurs either through the pores or the edges of the plate. The averaged wall-normal velocities for the open and closed conditions are shown in Figure 4.8. In the open condition (Figure 4.8a), local regions of high velocities are present above all the pores indicating that flow is being injected into the boundary layer. The effects of this injection are wall-bounded and diminish in the upper region of the boundary layer. On the other hand, in the closed condition, the wall-normal velocities over the pores are lower and the disturbances spread higher into the boundary layer.

The boundary layer profiles of the open and closed cases in Figure 4.9 show the influence of wall-normal fluid interactions on the mean flow and turbulence statistics. Overall, all profiles corresponding to the open conditions are shifted upwards with respect to the reference. This is expected due to the local regions of high velocities that were present over the pores. In the outer regions of the boundary layer, the velocity fluctuations and Reynolds stresses overlap with the reference due to the diminished effects of the porous interactions as observed earlier. For the closed condition, the streamwise velocity fluctuations within buffer layer are lower than the reference. Although near-wall data is not reliable due to biases, the buffer layer data matches with the DNS data and thus reductions in the streamwise fluctuations are valid. However, the Reynolds stress in the logarithmic layer is higher indicating an increase in turbulence activity.

In the burst profiles that were computed using the VITA technique (Figure 4.10), the difference in number of events between the closed case and the reference is large for y^+<30, which coincides with the streamwise velocity fluctuations profile. Beyond y^+=30, the difference in sweeps count reduces while the ejections count matches with the reference. The small increase in the streamwise velocity fluctuations above y^+=30 is reflected in the burst profiles as an increase in turbulence activity. The burst profiles of open case in most regions show lower occurrences of turbulence events which is contrary to the turbulence intensity profiles. One possible reason for the underestimation of the turbulence events could be the size of the averaging window. Windows that are smaller than the large-scale structures might detect signals that are lower than the detection threshold and filter them out.

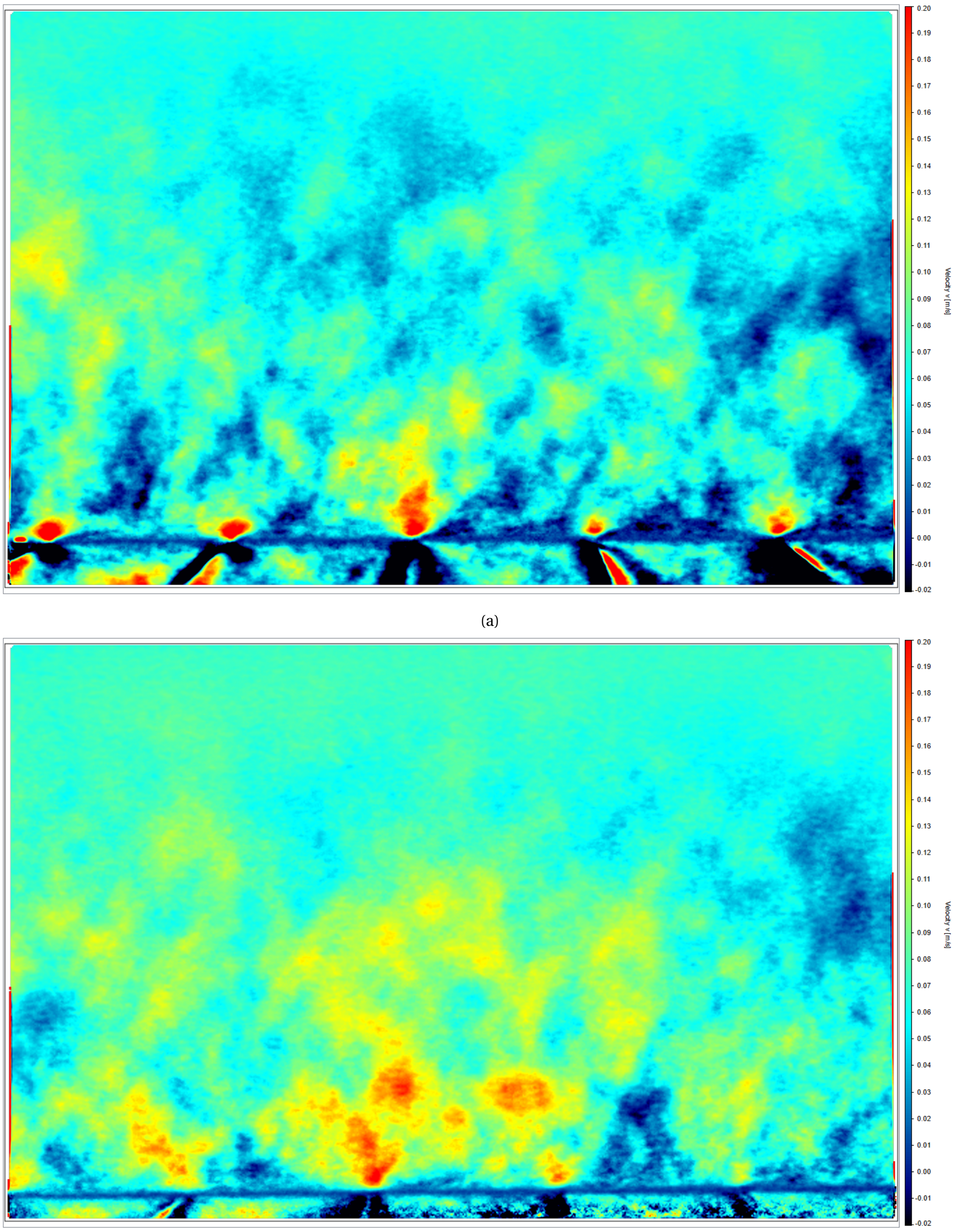

(a)

(b)

Figure 4.8: Averaged wall-normal velocity fields for the PN-B design; flow is from left to right (a) Open base (b) Closed base

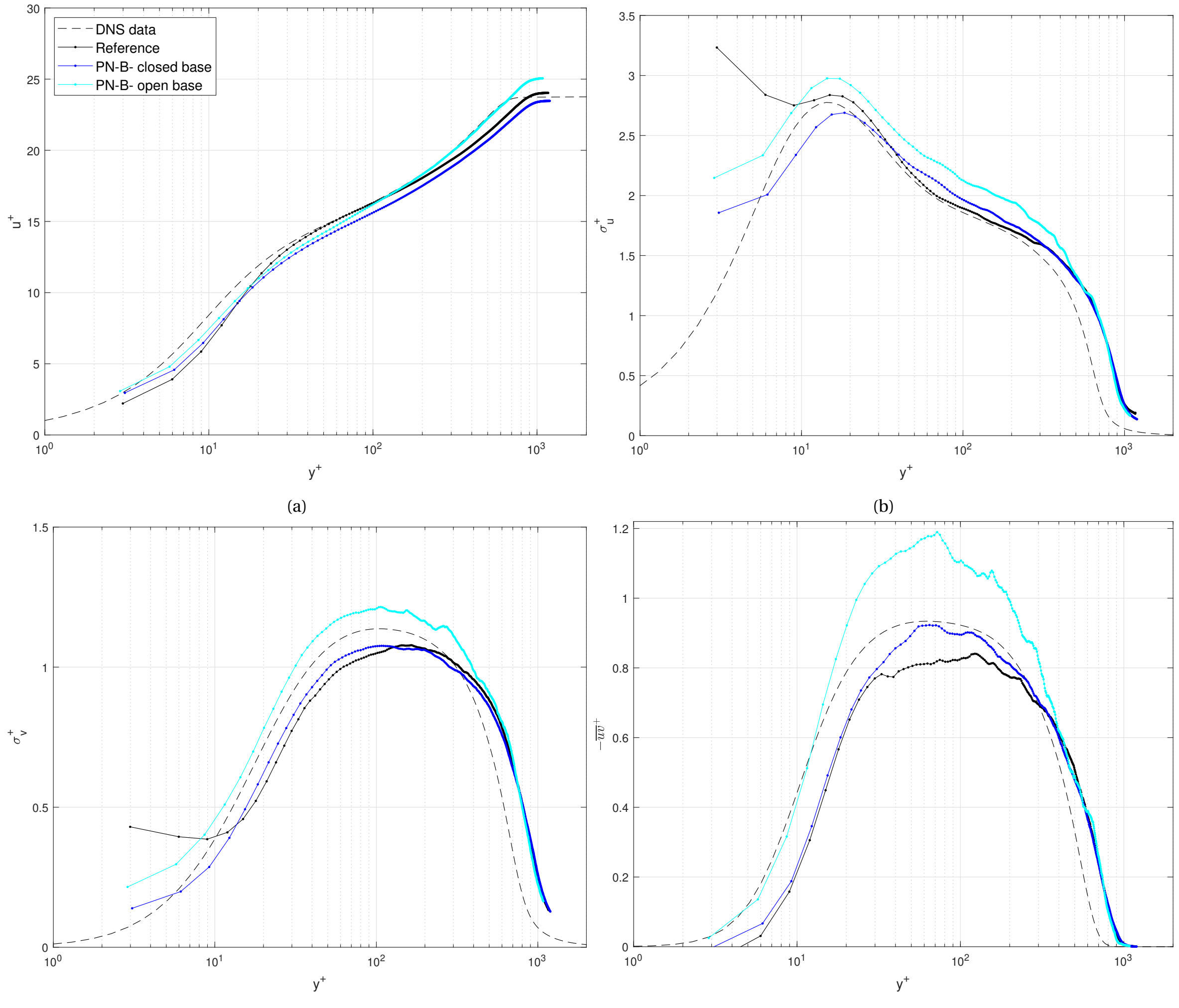

(a) (b)

(c) (d)

Figure 4.9: Boundary layer profiles of PN-B design with the open and closed base and smooth reference at station 4 (a) Mean velocity (u^+). (b) Streamwise velocity fluctuations (σ_u^+). (c) Wall-normal velocity fluctuations (σ_v^+). (d) Reynolds stress ($-\overline{uv}^+$)

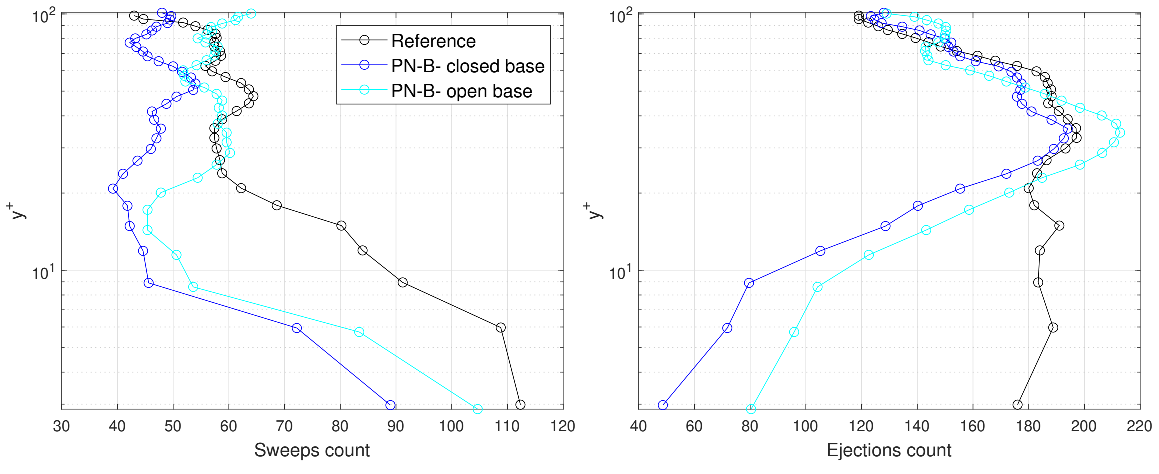

(a) (b)

Figure 4.10: Burst profiles with open and closed base and smooth reference at station 4 (a) Sweeps (b) Ejections

Correlation with hot-wire measurements

Hotwire measurements were performed for a few designs and their correlation with the PIV measurements is presented in this section. The hotwire measurements were performed at the trailing edge of the test plate, behind the last row of cavities. The mean velocity profiles and streamwise velocity fluctuations of the PN-dS, PN-ST and G-M designs obtained from PIV and HWA are compared. However, it should be noted that the Re_τ of the PIV, HW and DNS measurements are not consistent. The Re_τ of the PIV measurements is about 900, HW measurements are about 1200 and DNS data is 600. Hotwire data is not available in the near-wall region due to the physical limitations of the measurement technique. The mean velocity profiles agree well with the DNS data but a large offset in streamwise velocity fluctuations is present. This could be attributed to the difference in Re_τ.

The mean velocity profiles (Figure 4.11a,Figure 4.13a and Figure 4.15a) of all the designs are shifted upwards within the buffer layer. The highest shift occurs within the viscous sublayer and lower part of the buffer layer. This upshift could be caused by the biases in the near-wall region and/or the interaction between the pores and the flow. The percentage of contribution between these two effects is difficult to determine and it is likely to vary for each design. However, even if the flow is modified in the presence of the pores, their effects are not seen beyond the buffer layer in the PIV results as the profiles overlap with the reference. The hot-wire profiles show stronger wakes in the outer region which could be a result of the higher Re_τ.

The PIV streamwise velocity fluctuations profiles of PN-dS (Figure 4.11b) and G-M (Figure 4.15b) show a reduction in their peaks with respect to the reference. These reductions although small are statistically significant as they are outside the error margin introduced by measurement noise. On the other hand, the peak of the PN-ST profile (Figure 4.13b) is higher than the reference. The HW streamwise velocity fluctuations profiles of all the designs are lower than the corresponding HW reference. The inconsistency between the PIV and HW profiles of the PN-ST design could be caused due the streamwise spatial averaging of the PIV data. The wall-normal velocity fluctuation profiles of PN-dS (Figure 4.11c) and G-M (Figure 4.15c) overlap the reference profile in most regions. A small reduction in the peak is observed in both cases at $y^+ > 100$ indicating minor damping of the wall-normal fluctuations. In the PN-ST profile (Figure 4.13c), the fluctuations are higher than the reference at $y^+ < 30$. This could be because of an exchange of fluid through the pores, causing an increase in the strength or occurrence of the near-wall turbulent activity.

In the Reynolds stress profiles, the peak of the PN-dS design (Figure 4.11d) is lower than the reference and is shifted closer to the wall. For the PN-ST design (Figure 4.13d, the magnitude of the peak is similar to the reference but is also shifted closer to the wall. On the other hand, the peak of the G-M Reynolds stress profile (Figure 4.15d) is significantly lowered with respect to the reference in the region $20 < y^+ < 300$. This is the consequence of reductions in both streamwise and wall-normal velocity fluctuations. The burst profiles support the trends observed in the streamwise velocity fluctuation profiles. For the PN-dS and G-M designs (Figure 4.12 and Figure 4.16), the significant reduction in the number of sweeps and ejections below $y^+ = 30$ corresponds with the lowering of the streamwise fluctuations peak. Similarly, for the PN-ST design (Figure 4.14), the increase in velocity fluctuations is reflected as a sharp increase in the occurrences of both sweeps and ejections.

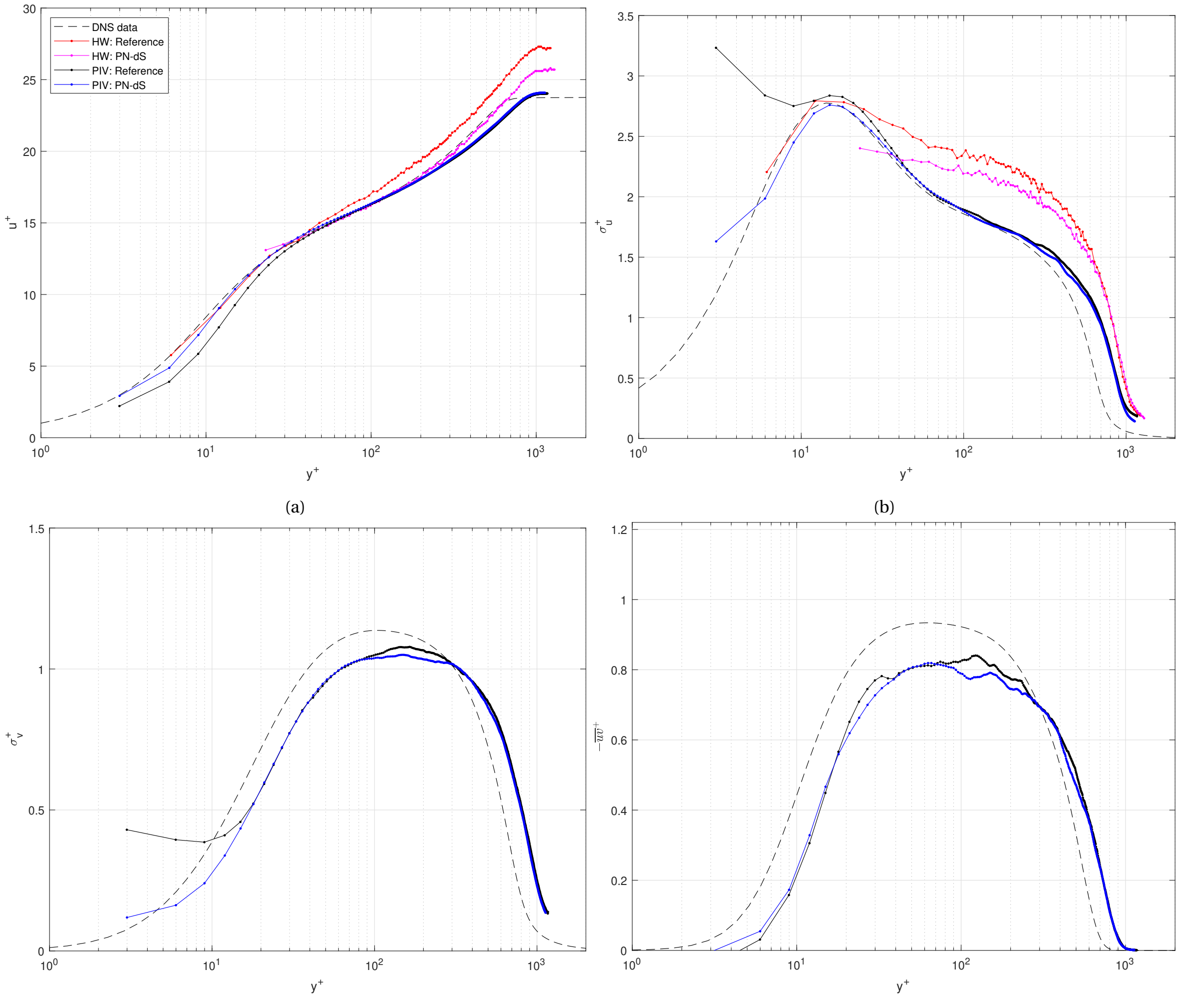

(a) (b)

(c) (d)

Figure 4.11: Boundary layer profiles of PN-dS design and smooth reference at station 4 (a) Mean velocity (u^+). (b) Streamwise velocity fluctuations (σ_u^+). (c) Wall-normal velocity fluctuations (σ_v^+). (d) Reynolds stress ($-\overline{uv}^+$)

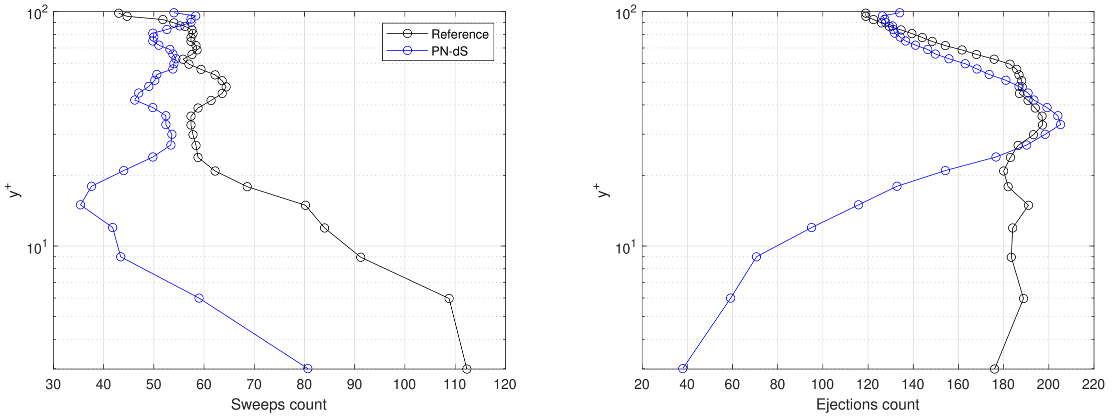

(a) (b)

Figure 4.12: Burst profiles of PN-dS design and smooth reference at station 4 (a) Sweeps (b) Ejections

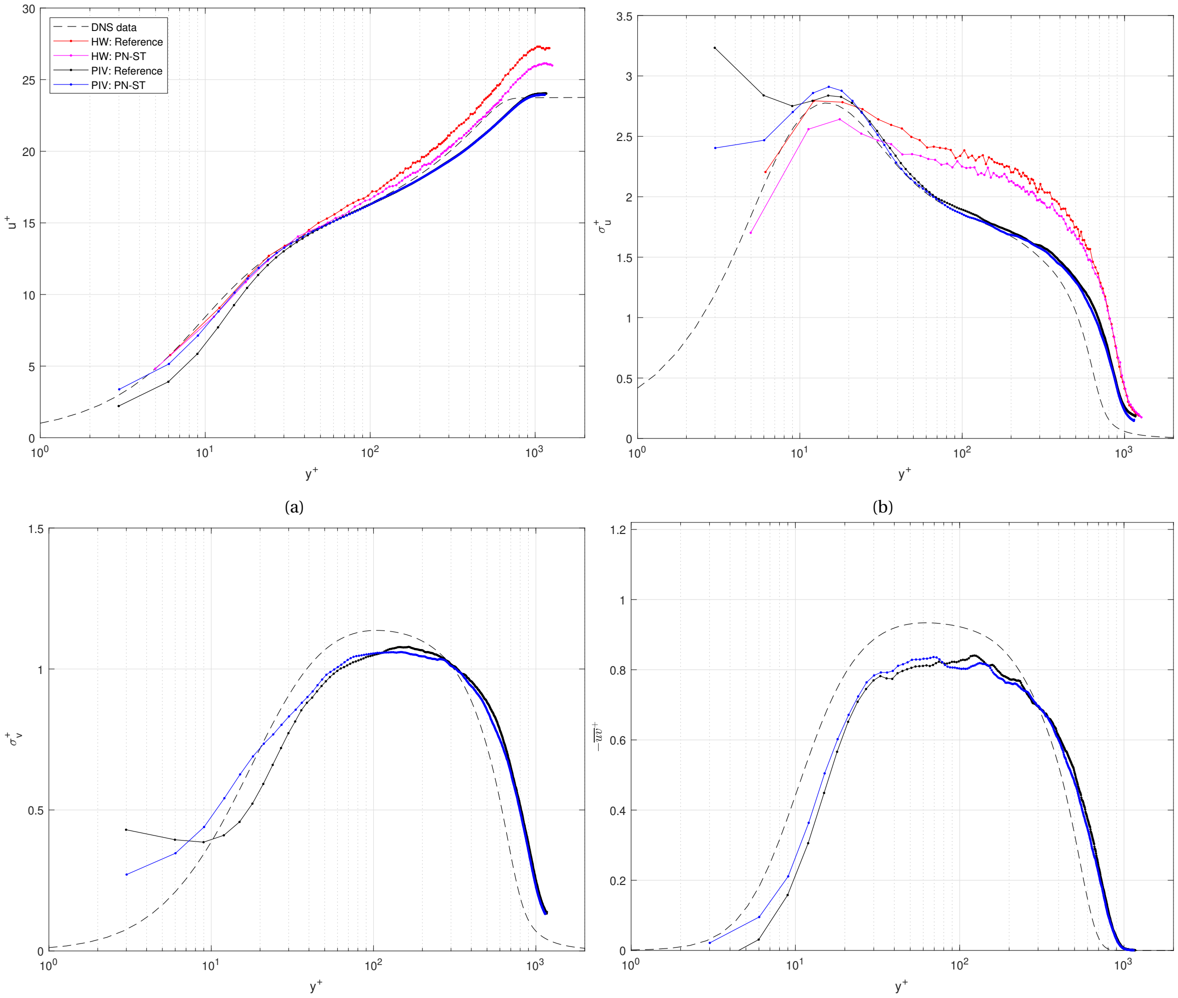

(a) (b)

(c) (d)

Figure 4.13: Boundary layer profiles of PN-ST design and smooth reference at station 4 (a) Mean velocity (u^+). (b) Streamwise velocity fluctuations (σ_u^+). (c) Wall-normal velocity fluctuations (σ_v^+). (d) Reynolds stress ($-\overline{uv}^+$)

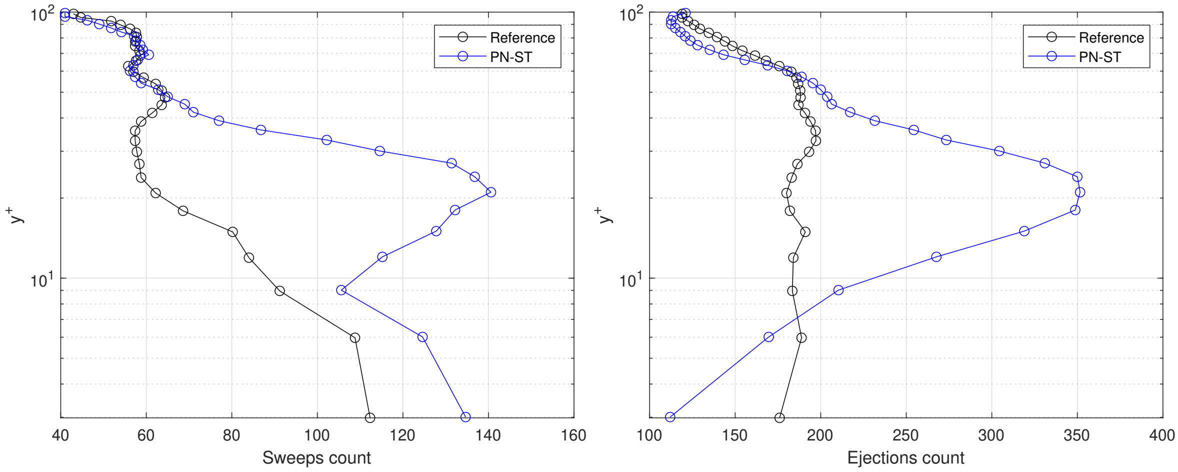

(a) (b)

Figure 4.14: Burst profiles of PN-ST design and smooth reference at station 4 (a) Sweeps (b) Ejections

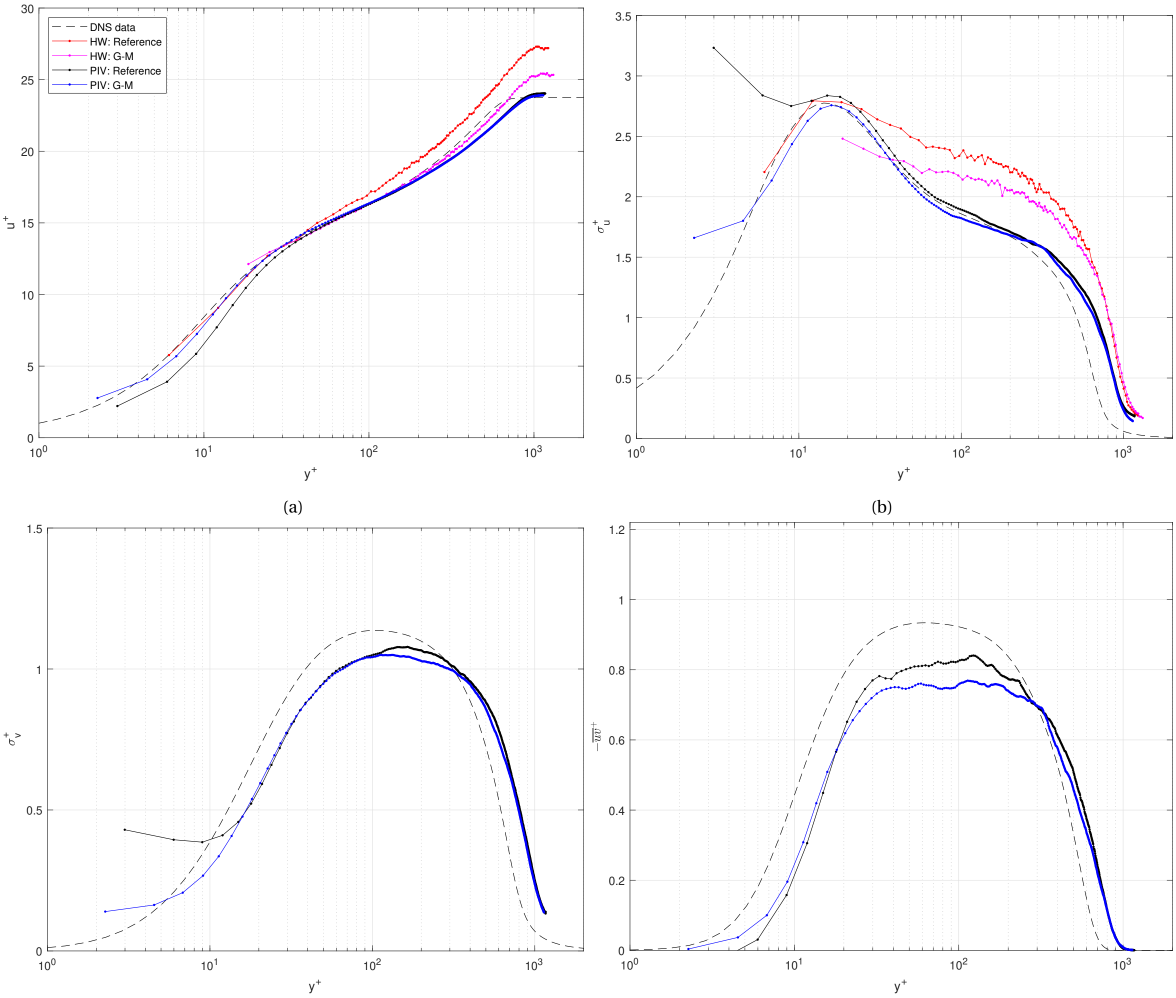

(a) (b)

(c) (d)

Figure 4.15: Boundary layer profiles of G-M design and smooth reference at station 4 (a) Mean velocity (u^+). (b) Streamwise velocity fluctuations (σ_u^+). (c) Wall-normal velocity fluctuations (σ_v^+). (d) Reynolds stress ($-\overline{uv}^+$)

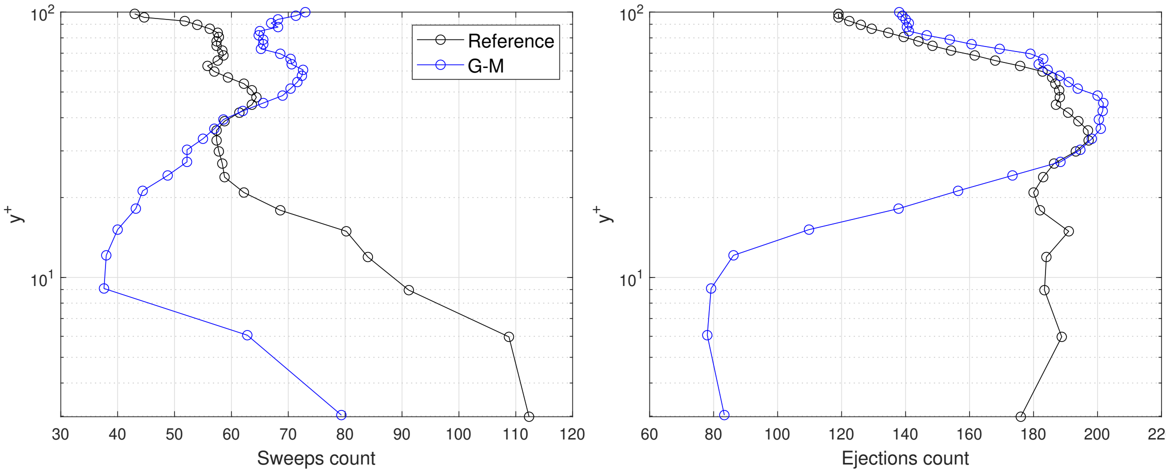

(a) (b)

Figure 4.16: Burst profiles of G-M design and smooth reference at station 4 (a) Sweeps (b) Ejections

Boundary layer development over a micro-cavity array

In this section, characteristics of the turbulent boundary layer at three streamwise locations over a micro-cavity array are discussed. The goal is to understand the development of a boundary layer passing over a micro-cavity. The PS-C design having a local micro-cavity array with a single backing cavity was used in this analysis. The first measurement station (S1) is at the centre of the cavity array, the second (S2) is at the trailing edge of the array spanning over the last three rows of pores and the third (S3) is downstream of the array (refer to Figure 3.16).

The mean velocity profiles (Figure 4.17a) of the test plate and the reference at all three stations overlap almost perfectly above $y^+ = 30$. However, within the viscous sublayer and buffer layer, the profiles of the test plate are higher than the reference. This trend is similar to the previous cases and is expected to be caused by the near-wall averaging effects and reflections. In the streamwise velocity fluctuations profiles (Figure 4.17b), the peak of the S1 profile is significantly shifted upwards in the region between $y^+ = 10$ and $y^+ = 20$. The peaks of the S2 and S3 profiles are relatively similar in magnitude and do not differ from their respective reference profiles; however, the location of the S3 peak is observed to shift closer to the wall.

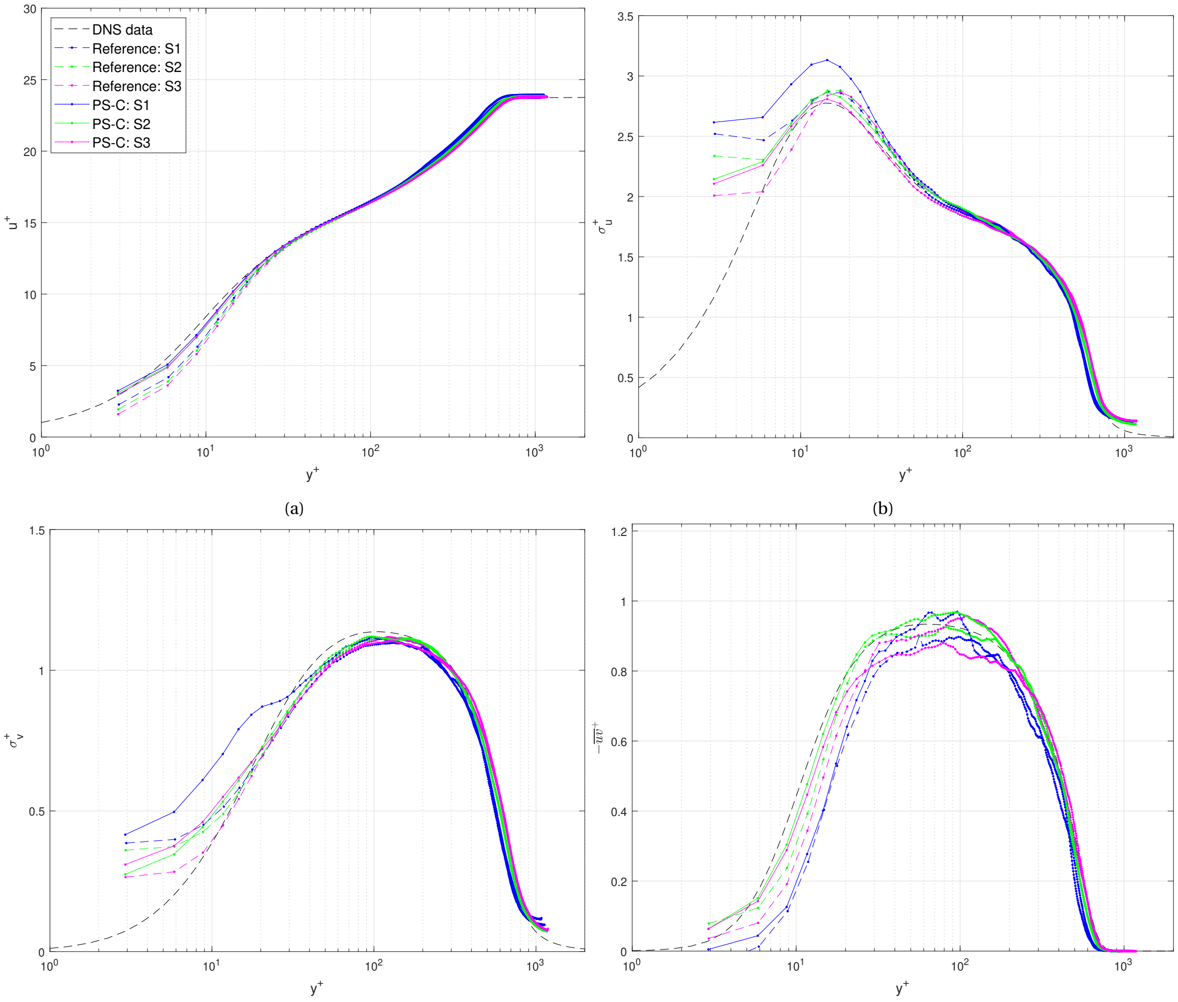

(a) (b) (c) (d)

Figure 4.17: Boundary layer profiles of PS-C design and smooth reference at stations 1,2 and 3 (a) Mean velocity (u^+). (b) Streamwise velocity fluctuations (σ_u^+). (c) Wall-normal velocity fluctuations (σ_v^+). (d) Reynolds stress ($-\overline{uv}^+$)

In Figure 4.17c, variations in wall-normal fluctuations are significant within the buffer layer, whereas the profiles in the logarithmic and outer regions of the boundary layer are almost indistinguishable. The S1 profile shows a large increase in wall-normal fluctuations which could be caused by the interaction between the fluid and the pores. At S2 and S3, the fluctuations decrease and are similar in magnitude. The Reynolds stress (Figure 4.17d) peaks of the test plate at S1 and S2 have a similar magnitude and are higher than the reference peaks. However, the peak of S3 drops below the reference and is the lowest. Thus, the Reynolds stresses are higher over the pores and reduce behind the micro-cavity array.

The burst profiles in Figure 4.18 show that the turbulence activity is the highest at S1. This corresponds with the peaks in the velocity fluctuation profiles. The similarity of the streamwise fluctuation peaks at S2 and S3 are reflected in the sweeps profile. The ejections profile shows a higher event count at S1 and S3. In comparison to S2 and S3, the peaks of the burst profiles at S1 are shifted away from the wall. Overall, the number of bursts decreases from the center of the array towards the leading edge and then increases again behind the array.

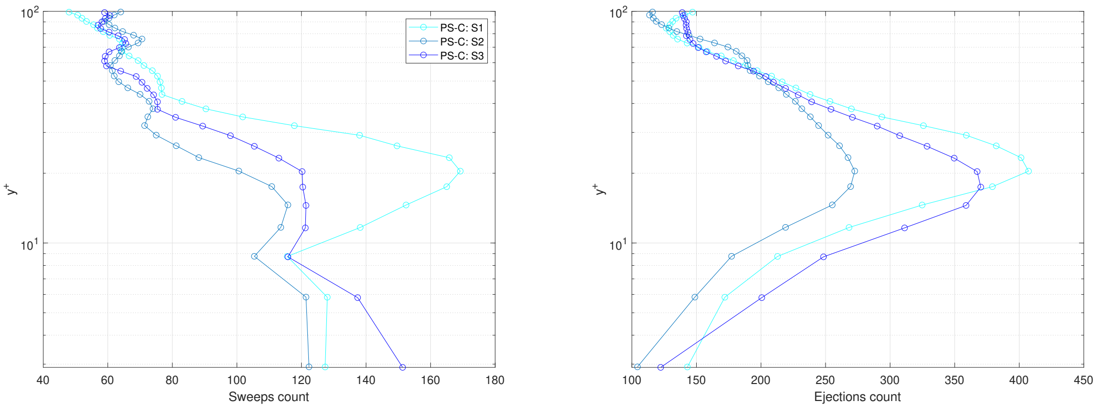

(a) (b)

Figure 4.18: Burst profiles of PS-C design at stations 1,2 and 3 (a) Sweeps (b) Ejections

4.3.3. Detection of events using the VITA technique

The detection of turbulence events was performed using the VITA technique. Figure 4.19 shows the events detected at y^+=100 in a single instantaneous velocity field. As VITA was performed using the spatial information from PIV measurements, the time axis corresponds with the streamwise space in Figure 4.20. The positive signal represents a sweep and the negative signal represents an ejection. The regions corresponding to the detections are highlighted in the figure below. On observing the velocity vectors, it is evident that at the location of an ejection there is the out-rush of fluid. Similarly, the sweep location shows fluid moving downwards. This indicates that the VITA detections correlate with the turbulence phenomena observed in the vorticity field. It should however be noted that the detection is sensitive to the threshold value k. Blackwelder and Kaplan (1976) reported that with increasing k, the number of detections increase. This effect has not been investigated in this work, but the selected threshold value is based on the work of Silvestri et al. (2017a) and Scarano et al. (2022b).

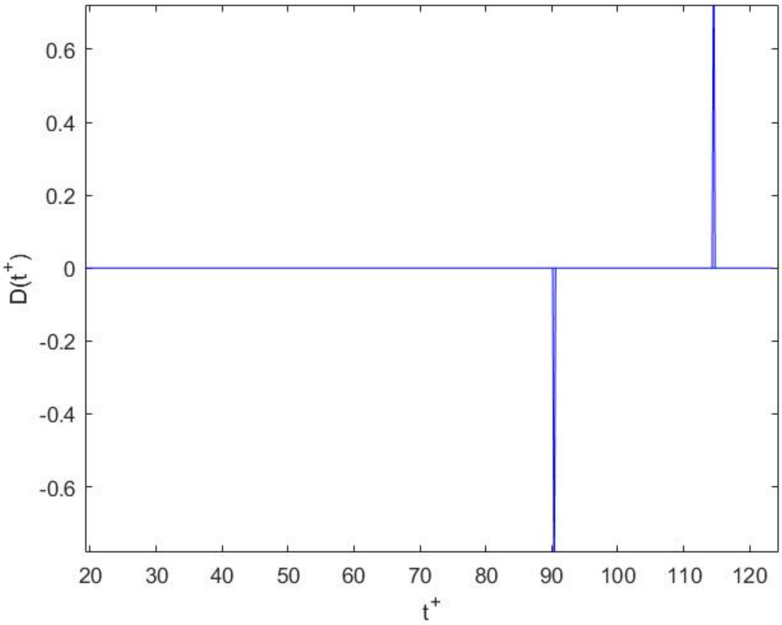

Figure 4.19: Detection of sweep and ejection events in the TBL of the reference at y^+=100; positive detection: sweep, negative detection: ejection

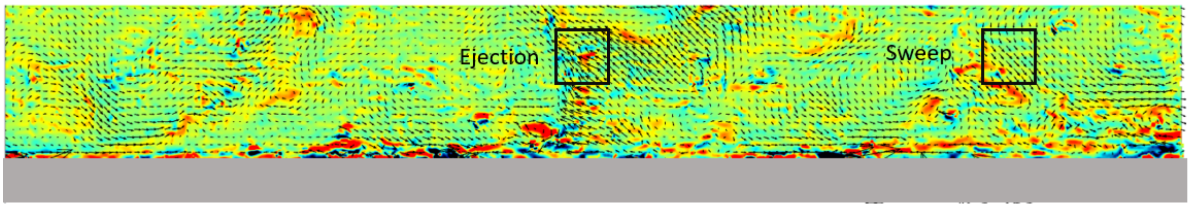

Figure 4.20: Instantaneous minus mean vorticity field of the reference plate; flow is from left to right

4.4. Discussion of PIV results

Existing research on micro-cavity arrays (Silvestri et al., 2017a,b; Bhat et al., 2021; Scarano et al., 2021, 2022b) has shown their capability to reduce turbulence energy in the boundary layer by interacting with the near wall sweep and ejection events. These events are responsible for the production of Reynolds stress which accelerates the near-wall flow and increases skin friction (Adrian, 2007). Therefore, a reduction in sweep and ejections is linked with skin friction reduction. In this section, a comparison between the current work and existing results is discussed.

Silvestri et al: Experimental

Hotwire measurements conducted by Silvestri et al have shown that a local micro-cavity array on a flat plate reduces the streamwise velocity fluctuations in a turbulent boundary layer. This phenomenon has been observed for arrays with and without a backing cavity. In this work, the PS-C is a replica of their design and has been tested under similar conditions to validate the reported results. A comparison between the current work and the results of Silvestri et al. (2017b) is shown in Figure 4.21. There is a significant difference between the streamwise velocity fluctuations below $y^+ = 200$ for all the cases. This could be because of the state of the turbulent boundary layer in the test section. Although freestream conditions and development length of the boundary layer were replicated, there is a possibility that the approaching boundary layer is different due to the tripping mechanism. The results of the current work align well with the DNS data indicating a well-developed turbulent flow. A reduction in the turbulence intensity with respect to the reference is observed in both experiments. In Silvestri et al's data, the peak of the design with the 5mm backing cavity is reduced by 3.09% and the peak of the PS-C with a 3mm backing cavity is reduced by 1.9%. While the reduction is restricted within the buffer layer in the current work, Silvestri et al's data show the reduction extending up to the log layer. Moreover, the reduction of turbulence increases with the increasing size of the backing cavity up to a maximum of 3.5%, which could not be studied in this work due to restrictions in the experimental setup.

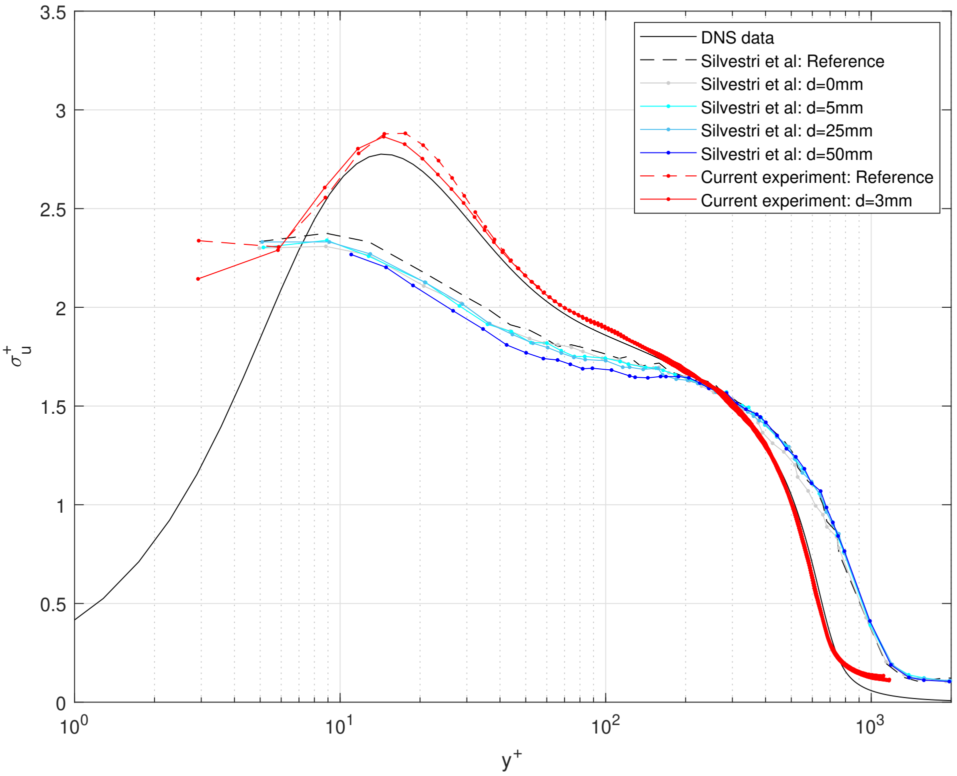

Figure 4.21: Comparison of the current PIV results of PS-C design at S2 with Silvestri et al. (2017b)'s hotwire results of a micro-cavity array with a backing cavity of varying depths

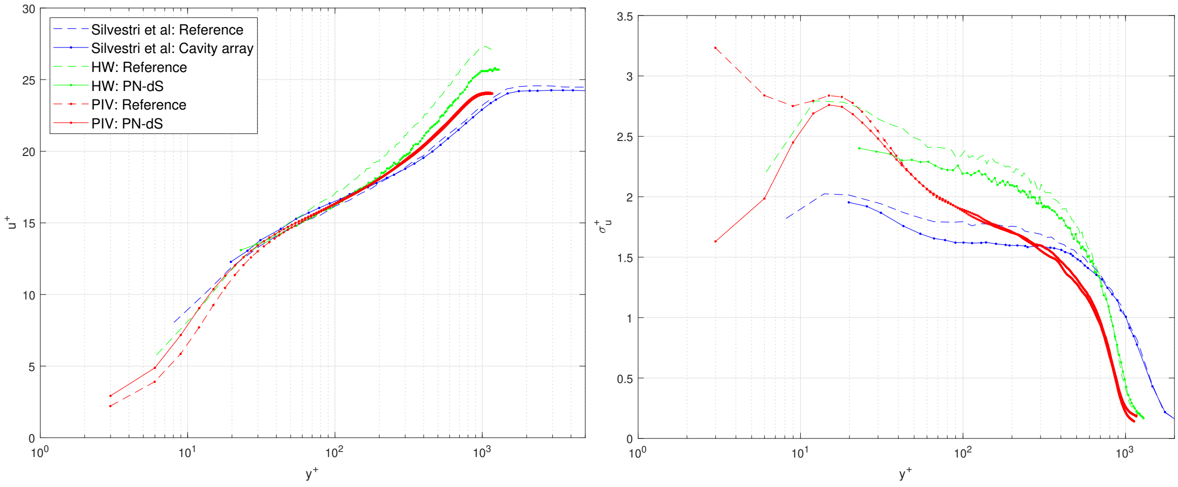

(a)

(b)

Figure 4.22: Comparison of the current PIV and HW results of PN-dS design with Silvestri et al. (2017a)'s hotwire results of a micro-cavity array without a backing cavity

A comparison of another case is depicted in Figure 4.22. This is a porous plate without a backing cavity. Hotwire measurements of Silvestri et al. (2017a) taken behind a local micro-cavity array are compared with PIV and hotwire data recorded at the trailing edge of the PN-dS design. In the mean velocity plot (Figure 4.22a), the profiles correlate very well specifically in the log layer but the same cannot be said about the streamwise fluctuations profile (Figure 4.22b). Similar to the previous case, a large difference in turbulence intensities is observed between the two experiments. Looking at the trends in the profiles, it is evident that the hotwire measurements in show a significant reduction in turbulence intensities. Moreover, this reduction extends up to the log layer in both cases. However, the PIV profile shows only a local reduction in turbulence.

Bhat et al: DNS

Bhat et al. (2021) analysed the characteristics of the turbulent boundary layer over the micro-cavity design that was optimised by Silvestri et al for maximum turbulence attenuation. Figure 4.23 presents a comparison between the DNS results and PIV results at the centre (mid) and trailing edge of the cavity array (end). It should be noted that the DNS simulations were performed in a channel flow at $Re_\tau = 1660$ whereas the PIV experiments were performed in a normal turbulent flow at $Re_\tau = 900$.

Overall, the correlation between the DNS and PIV results is better in comparison to the correlation between the hotwire results of Silvestri et al and the current work. The DNS streamwise velocity profiles overlap but the PIV profiles show a reduction in the peak behind the cavities. On the contrary, the wall-normal fluctuations and Reynolds stress behind the cavities in the DNS data are lower. This indicates a reduction in turbulence energy which however does not correlate with the PIV results. Opposing trends between the DNS and PIV data do not provide a clear answer to the streamwise development of the turbulent boundary layer over the pores.

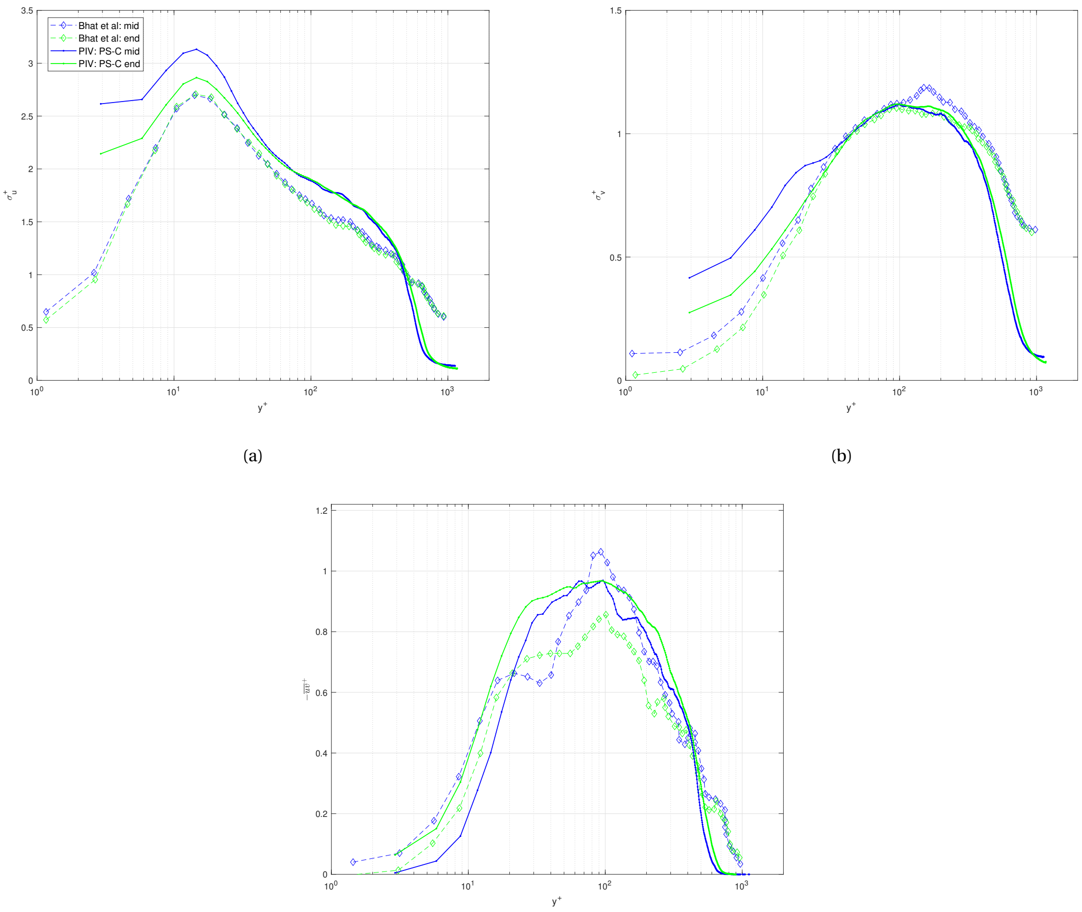

(a)

(b)

(c)

Figure 4.23: Comparison of the current PIV of PS-C design at S1 and S2 with Bhat et al. (2021)'s DNS results of a micro-cavity array with a backing cavity (d=50mm) at the mid and end of the cavity array

5

Discussion

A overarching discussion of the results are discussed in this chapter. Section 5.1 presents a comparison of the experimental results and Section 5.2 presents a discussion on the validation of results from literature.

5.1. Comparison of experimental results

The drag produced by the porous and groove test plates placed in a turbulent flow is the foremost factor under investigation in this study. The overall drag of the test plates was measured through direct force measurements (DFM) and the skin friction drag was estimated indirectly from u_τ through PIV and hotwire measurements. ΔC_D obtained from DFM is the difference in total drag while ΔC_f is the difference in skin friction drag component between a test design and smooth reference.

An overview of drag estimations, peak streamwise velocity fluctuations and peak Reynolds stress from the different experimental methods is presented in Figure 5.1 for a few test designs. The ΔC_f from HW experiments show a drag increase for all the tested designs. This is contrary to the trend observed in the streamwise velocity fluctuations profiles in Section 4.3.2, where the streamwise velocity fluctuations of the test designs were lower than the smooth reference. This could be interpreted in two ways; the reduction in the streamwise turbulence intensities which is an indication of a reduction in turbulence energy does not correlate with C_f reduction or the indirect estimation of C_f through boundary layer fitting is not accurate. The PIV estimations ΔC_f show both an increase and decrease in skin friction drag. For the PN-B, PN-XS, G-S and G-M designs there is an increase in C_f but similar to the HW results, their corresponding streamwise velocity fluctuations profile has a lower peak than the reference. However, peaks of the Reynolds stress profiles of these designs (excluding G-M) are higher than the reference. Therefore, the increase in C_f corresponds with the increase in Reynolds stress. The G-M is an exception as it produces an increase in C_f but which does not correlate with the behaviour of its velocity fluctuations or Reynolds stress profiles. The PN-ST design is the only one whose drag increase is consistent with all its turbulent statistics results. A reduction in C_f is observed for the PN-dS and PN-DL designs. The turbulent statistics of PN-dS correlate with the lower C_f due to reductions in the streamwise velocity fluctuations and Reynolds stress peaks. For PN-DL, the small drag reduction correlates with a Reynolds stress reduction present above $y^+ = 100$.

The ΔC_D from direct force measurements show a drag increase for all the test plates. As this indicates the total drag, the contribution of pressure drag is believed to be significant. Even if it is assumed that the C_f estimations are inaccurate, the reduction in the peaks of the velocity fluctuations and Reynolds stresses do not correlate with the drag performance. This strengthens the hypothesis that the contribution of pressure drag outweighs skin friction reduction.

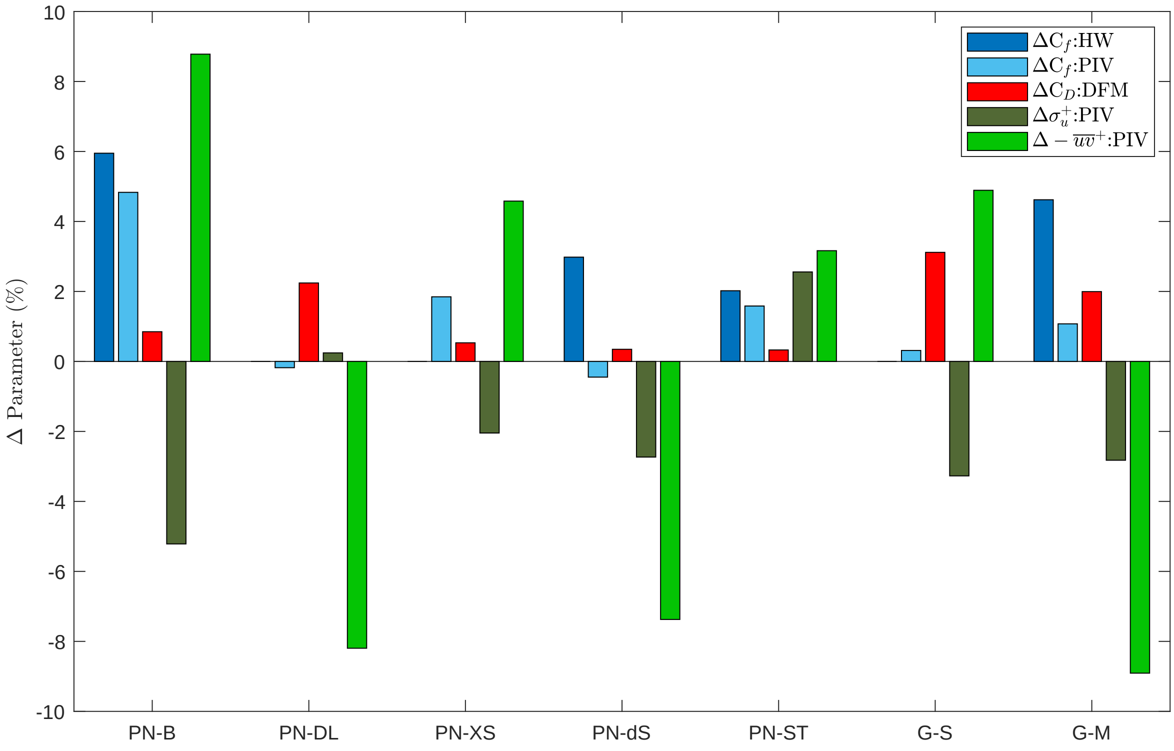

Figure 5.1: Comparative overview of drag estimations from hotwire, PIV and direct force measurements and peak streamwise velocity fluctuations and Reynolds stresses from PIV

5.2. Validation of results

Validation of existing results on micro-cavity array was performed by replicating several designs. The PS-C design was the closest replica to Silvestri et al. (2017a)'s localised micro-cavity array with a backing cavity. One design aspect which could not be replicated was the volume of the backing cavity. The prominent difference in results was the values of turbulence intensities. The overall turbulence energy in Silvestri's experiments was much lower than the current research and the DNS data. This showed that the turbulent flow field was not similar in both cases. For a localised micro-cavity array with a shallow backing cavity, the reduction of peak turbulence intensities is validated. This reduction is present only within a small region of the turbulent boundary layer which is contrary to Silvestri et al's result. Similar observations have been made with the PN-dS design which does not contain a backing cavity. The hot-wire measurements are validated by the hot-wire measurements from the current research as reductions in turbulence intensities in both cases extend into the outer layer. These cases strengthen the argument from literature that wall-normal pores manipulate the turbulent boundary layer and reduce its energy.

In the DNS study, Bhat et al. (2021) investigated the wall-normal flow through pores and stated that the direction of the wall-normal flow in the pores depends upon the flow structures in the turbulent flow above them. A combination of downward and upward flow components was observed as shown in Figure 5.2. Bhat et al. (2021) proposed that the wall-normal interactions damp the Reynolds stress and turbulence intensities in the buffer and log regions of the boundary layer resulting in a reduction of skin friction drag. To check this theory, the averaged wall-normal velocity fields of the PN-B design(Figure 5.3). This test plate has a large cavity below as it was raised with spacers. An injection of fluid through the pores into the boundary layer is visible which occurs due to the cavity beneath the plate. The flow that enters through the pores is redistributed within the cavity and ejected back into the TBL. Although this results in the reduction of the streamwise fluctuations peak by 5.2%, the Reynolds stress increases by 8.8%. Furthermore, the skin friction drag estimated through HWA and PIV is 6% and 4.9% respectively. This contradicts the theory proposed by Bhat et al.

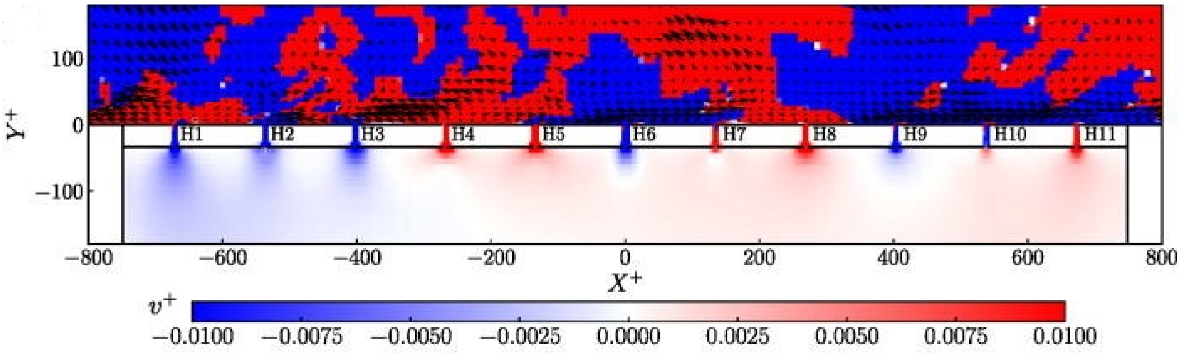

Figure 5.2: Wall-normal interactions between pores and the turbulent boundary layer (Bhat et al., 2021)

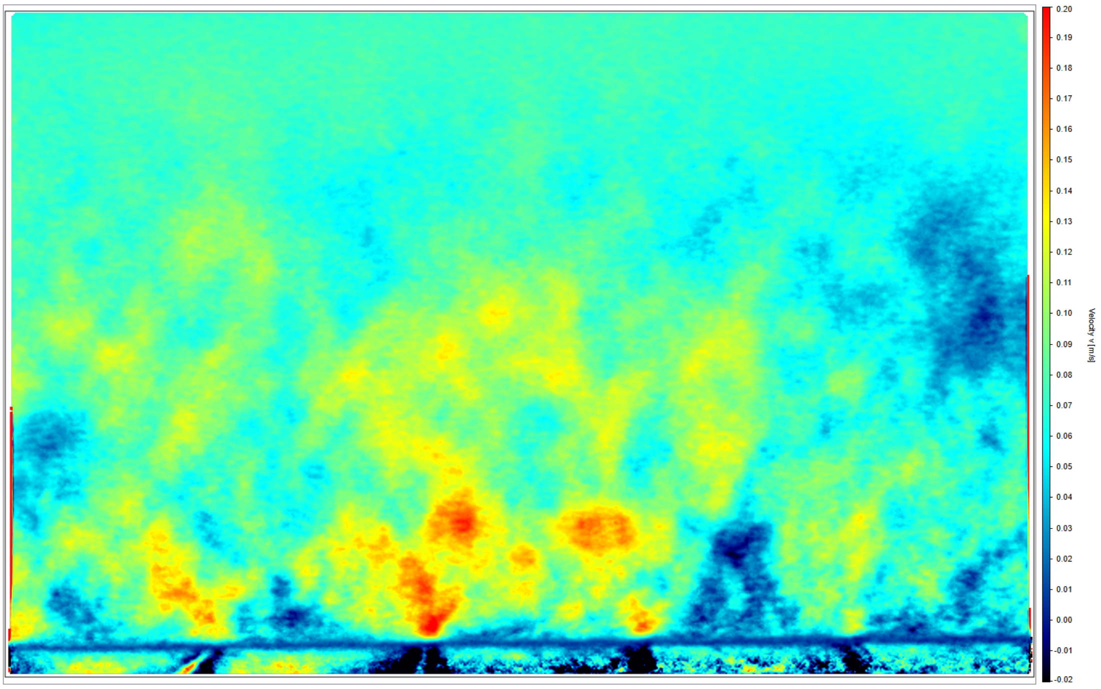

Figure 5.3: Averaged wall-normal velocity field of PN-B design; flow is from left to right

In conclusion, experimental results show that some designs of pores and grooves are capable of reducing the turbulence energy in the boundary layer similar to the results found in literature. However, the overall drag of these designs are higher than a smooth reference. The drag increase has been argued to be a contribution of pressure drag which has not been investigated by any of the research groups working with wall-normal pores.

6

Conclusions and recommendations for further research

6.1. Conclusions

Ongoing research by the research groups of Silvestri et al and Gowree et al on perforated plates showed that certain designs of micro-cavity arrays were able to reduce skin friction drag. While Bhat et al. (2020) in a DNS study computed a 5.6% reduction in skin friction drag, Gowree et al. (2019) reported up to 10% reduction through hotwire measurements. However, these research groups overlooked the contribution of pressure drag in their designs. In this thesis, several designs from literature were replicated to investigate their total drag performance and determine the flow mechanism in the presence of pores. The general observation was that none of the test plates with pores and grooves showed a drag-reducing performance. It has been argued that the pressure forces acting inside pores and grooves cause an overall drag increase which overtakes any minor reductions in skin friction drag. Flow field measurements in certain cases showed reductions in turbulence intensities, however, this did not correlate with the estimated skin friction. The VITA technique was implemented for the detection of turbulence events, which showed that the turbulence intensities correlated with the occurrence of bursts in most cases. Although the pores interact with the turbulent flow and reduce their energy, it does not signify a drag-reducing mechanism. The research questions posed at the beginning of the thesis are answered below,

RQ1:How does the performance of reproduced micro-perforated plates compare with existing results?
The skin friction drag reductions reported in existing literature were not observed in the current work. All designs experienced a larger drag with respect to the smooth reference plate. Flow field measurements using PIV and HWA showed a reduction in streamwise turbulence intensities which was similar to the results from literature but skin friction values computed from friction velocity showed a drag increase.

RQ2:How do the design parameters of the micro-perforated arrays and backing cavities affect their performance?
Pressure drag has been identified as a significant contributor to overall drag in micro-perforated plates. The most common trend observed in the direct force measurements is the increase in drag with increasing porosity. The design parameters governing the porosity of a perforated array are pore diameter and spacings. It has been observed that drag increases with increasing pore diameter and decreasing spacing. The drag performance of backing cavities correlated with the volume of cavities. Backing cavities with a larger volume were observed to produce higher drag. This is caused by the injection of fluid into the boundary layer. The backing cavity receives and redistributes fluid through the pores causing a destabilising wall-blowing action. This mechanism contradicts Bhat et al. (2020) theory that wall-normal interactions damp the turbulence energy in the boundary layer resulting in skin friction reduction.

RQ3:Can the drag-reducing potential of spanwise grooves with square cross-sections be validated?
PIV experiments have shown that the G-M design reduces turbulent energy in the boundary layer. The peak of the Reynolds stress profile was significantly lower than the reference. The estimated skin friction coeffi-

cient was however higher than the reference by 1%. Moreover, the overall drag of all the groove designs over also higher than the reference. The downstream wall of the grooves is exposed to the flow and is acted upon by pressure forces. With an increasing area of the downstream wall, the drag was also observed to increase. Therefore, the turbulence energy reduction of the grooves is minor with respect to pressure drag increase.

RQ4:Are the current flow characterisation techniques sufficient for determining the mechanism behind drag behaviour?
Characteristics of the turbulent boundary layer were studied using boundary layer profiles of mean velocities, streamwise and wall-normal velocity fluctuations, Reynolds stress and burst profiles. The changes in turbulent energy caused by the occurrences of sweeps and ejections were analysed. This provided some insight into the influence of the pores and grooves on the turbulent activity. As the detection of events using VITA is sensitive to the size of the averaging window and detection threshold, further investigation is required to support the current analysis. The pressure drag hypothesis could not be verified with the PIV or hotwire data. To test this hypothesis, the flow field inside the pores and grooves needs to be analysed.

6.2. Recommendations

Based on the experiences and results derived from the current thesis, the following recommendations are suggested for future research on wall-normal pores.

- **Improvements in test plates and experimental setup**
  In this research, the test plates were reflective as they were black acrylics which reduced the accuracy of the near-wall data in PIV measurements. For further research, it is recommended to make test plates with a non-reflective material. The PIV plate mount (PHill) had a hollow cavity beneath the test plates which affected the measurement of certain plates. An airtight mount which allows the test plate to be flush with the leading edge mount would be a preferred option.

- **Perform VITA on Reynolds stress**
  The detection of turbulence events in this work was performed by applying VITA to streamwise velocity fluctuations in the spatial domain. To further analyse the modification of turbulent coherent structures, applying VITA to the normalised Reynolds stress signal $-\overline{uv}^+$ is recommended. The influence of Reynolds stress on the burst cycle can be studied with this technique.

- **Investigation into the pressure drag hypothesis**
  This research has presented the hypothesis that the drag-increasing component of porous plates is the pressure forces acting inside pores. To test this hypothesis, it is crucial to analyse the flow mechanism inside pores. The phenomenon of shear layer entrainment and impingement on the inner porous walls needs to be further studied.

- **Testing of wall-normal pores in adverse and favourable pressure conditions**
  Du et al. (2022) performed an experimental investigation on 10 pores-per-inch porous media placed in a TBL with nonzero pressure gradient and reported high amounts of drag reduction in both adverse and favourable pressure gradients. As a next step, it would be interesting to investigate the drag performance of wall-normal pores in similar test conditions.

Bibliography

A. Hooshmand, J. M. W., R. A. Youngs, & Balint, J. (1982). An experimental study of changes in the structure of a turbulent boundary layer due to surface geometry changes. *AIIA paper, 83-0230*. https://doi.org/10.2514/6.1983-230

Adrian, R. J. (2007). Hairpin vortex organization in wall turbulence. *Physics of Fluids*, *19*(4), 041301. https://doi.org/10.1063/1.2717527

Airbus. (2019). *Global market forecast cities, airports aircraft 2019-2038* (Report).

Alhamdi, S. (2018). *Intermittency effects on the universality of local dissipation scales in turbulent boundary layer flows with and without free-stream turbulence* (Doctoral dissertation).

Allen, P. A. (2009). *Earth surface processes*. John Wiley & Sons.

Anders, S., III, W. S., & Washburn, A. (2004). Active flow control activities at NASA langley. *2nd AIAA Flow Control Conference*. https://doi.org/10.2514/6.2004-2623

Ashill, P. R., & Smith, P. D. (1985). An integral method for calculating the effects on turbulent boundary-layer development of sweep and taper. *The Aeronautical Journal (1968)*, *89*(882), 43–54. https://doi.org/10.1017/S0001924000017693

Benedict, L. H., & Gould, R. D. (1996). Towards better uncertainty estimates for turbulence statistics. *Experiments in Fluids*, *22*, 129–136.

Bhat, S. S., Silvestri, A., Cazzolato, B. S., & Arjomandi, M. (2021). Mechanism of control of the near-wall turbulence using a micro-cavity array. *Physics of Fluids*, *33*(7), 075114. https://doi.org/10.1063/5.0051375

Bhat, S., Silvestri, A., Cazzolato, B., & Arjomandi, M. (2020). Reduction in the turbulent instabilities in a boundary layer using micro-cavities. *Proceedings of the 22nd Australasian Fluid Mechanics Conference AFMC2020*. https://doi.org/10.14264/bb0925e

Blackwelder, R. F., & Kaplan, R. E. (1976). On the wall structure of the turbulent boundary layer. *Journal of Fluid Mechanics*, *76*(1), 89–112. https://doi.org/10.1017/S0022112076003145

Blackwelder, R. F., & Eckelmann, H. (1979). Streamwise vortices associated with the bursting phenomenon. *Journal of Fluid Mechanics*, *94*(3), 577–594. https://doi.org/10.1017/s0022112079001191

Boldman, D. R., & Brinich, P. F. (1976). Skin friction on a flat perforated acoustic liner. *14*(11), 1656–1659. https://doi.org/10.2514/3.7273

Buck, A. L. (1981). New Equations for Computing Vapor Pressure and Enhancement Factor. *Journal of Applied Meteorology and Climatology*, *20*(12), 1527–1532. https://doi.org/10.1175/1520-0450(1981)020<1527:Nefcvp>2.0.Co;2

Burden, H. W. (1969). The effect of wall porosity on the stability of parallel flows over compliant boundaries.

Choi, H., Moin, P., & Kim, J. (1994). Active turbulence control for drag reduction in wall-bounded flows. *Journal of Fluid Mechanics*, *262*, 75–110. https://doi.org/10.1017/S0022112094000431

Choi, K.-S., & Fujisawa, N. (1993). Possibility of drag reduction using d-type roughness. In K. K. Prasad (Ed.), *Further developments in turbulence management* (pp. 315–324). Springer Netherlands. https://doi.org/10.1007/978-94-011-1701-2_8

Choi, K.-S. (1989). Near-wall structure of a turbulent boundary layer with riblets. *Journal of Fluid Mechanics*, *208*, 417–458. https://doi.org/10.1017/S0022112089002892

Clauser. (1954). Turbulent boundary layers in adverse pressure gradients. *Journal of the Aeronautical Sciences*, *21*(2), 91–108. https://doi.org/10.2514/8.2938

Clauser, F. H. (1956). The turbulent boundary layer. *Advances in applied mechanics*, *4*, 1–51.

Corino, E. R., & Brodkey, R. S. (1969). A visual investigation of the wall region in turbulent flow. *Journal of Fluid Mechanics*, *37*(1), 1–30. https://doi.org/10.1017/S0022112069000395

Coustols, E., & Savill, A. M. (1992). Turbulent skin-friction drag reduction by active and passive means; parts 1 and 2. special course on Skin-Friction drag reduction. *Agard Report*, *786*, 8-1 to 8–80.

Drouin, M., Gallman, J., & Olsen, R. (2006). Sound level effect on perforated panel boundary layer growth. *12th AIAA/CEAS Aeroacoustics Conference (27th AIAA Aeroacoustics Conference)*, 2411.

Du, H. (, Li, Q. (, Zhang, Q. (, Zhang, W. (, & Yang, L. ((2022). Experimental study on drag reduction of the turbulent boundary layer via porous media under nonzero pressure gradient. *Physics of Fluids*, *34*(2), 025110. https://doi.org/10.1063/5.0083143

Elavarasan, R., Ching, C. Y., & Antonia, R. A. (1995). Turbulent boundary layer over a smooth wall with widely separated transverse square cavities. *Applied Scientific Research*, *55*(3), 227–243.

Fukagata, K., Iwamoto, K., & Kasagi, N. (2002). Contribution of reynolds stress distribution to the skin friction in wall-bounded flows. *Physics of Fluids*, *14*(11), L73–L76. https://doi.org/10.1063/1.1516779

Gad-el-Hak, M. (2006). *Flow control: Passive, active, and reactive flow management*. Cambridge University Press. https://books.google.nl/books?id=1IiFetRXG3kC

Gallagher, J., & Thomas, A. (1984). Turbulent boundary layer characteristics over streamwise grooves. *2nd Applied aerodynamics conference*, 2185.

Gerhold, C. H., Brown, M., & Jasinski, C. (2016). Evaluation of skin friction drag for liner applications in aircraft. *54th AIAA Aerospace Sciences Meeting*, 1267.

Ghanadi, F., Arjomandi, M., Cazzolato, B., & Zander, A. (2014a). Interaction of a flow-excited helmholtz resonator with a grazing turbulent boundary layer. *Experimental thermal and fluid science*, *58*, 80–92.

Ghanadi, F., Arjomandi, M., Cazzolato, B. S., & Zander, A. C. (2015). Analysis of the turbulent boundary layer in the vicinity of a self-excited cylindrical helmholtz resonator. *Journal of Turbulence*, *16*(8), 705–728. https://doi.org/10.1080/14685248.2015.1024839

Ghanadi, F., Cazzolato, B., Arjomandi, M., & Zander, A. (2014b). Experimental investigation of the application of a self-excited cylindrical helmholtz resonator for turbulent drag reduction.

Gowree, E. R., Jagadeesh, C., & Atkin, C. J. (2019). Skin friction drag reduction over staggered three dimensional cavities. *Aerospace Science and Technology*, *84*, 520–529. https://doi.org/10.1016/j.ast.2018.11.001

Hartog, F. (2021). *Turbulent boundary layers over surfaces with streamwise-preferential permeability- experimental investigation into the drag and flow mechanics*. Delft University of Technology.

Haugen, R., & Dhanak, A. (1966). Momentum transfer in turbulent separated flow past a rectangular cavity.

Hoang, V., Jafari, A., Silvestri, A., Cazzolato, B., & Arjomandi, M. (2021). The effect of a micro-cavity array on burst events in a turbulent boundary layer.

Howerton, B. M., & Jones, M. G. (2015). Acoustic liner drag: A parametric study of conventional configurations. *21st AIAA/CEAS Aeroacoustics Conference*, 2230.

Hunt, J. (1987). Coherent structures: Comments on mechanisms.

Hussain, A. K. M. F. (1986). Coherent structures and turbulence. *Journal of Fluid Mechanics*, *173*, 303–356. https://doi.org/10.1017/S0022112086001192

IATA. (2013). *Aircraft technology roadmap to 2050* (Report).

IATA. (2021a). Fuel fact sheet.

IATA. (2021b). Global CO_2 emissions from commercial aviation 2004-2022.

Jasinski, C., & Corke, T. (2020). Mechanism for increased viscous drag over porous sheet acoustic liners. *AIAA Journal*, *58*(8), 3393–3404.

Kametani, Y., Fukagata, K., Örlü, R., & Schlatter, P. (2015). Effect of uniform blowing/suction in a turbulent boundary layer at moderate Reynolds number. *International Journal of Heat and Fluid Flow*, *55*, 132–142. https://doi.org/10.1016/j.ijheatfluidflow.2015.05.019

Kármán, T.-H. V. (1921). Über laminare und turbulente reibung. https://doi.org/10.1002/zamm.19210010401

Kim, H. T., Kline, S. J., & Reynolds, W. C. (1971). The production of turbulence near a smooth wall in a turbulent boundary layer. *Journal of Fluid Mechanics*, *50*(1), 133–160. https://doi.org/10.1017/s0022112071002490

Kline, S., Reynolds, W., Schraub, F., & Runstadler, P. (1967). The structure of turbulent boundary layers. *J. Fluid Mech*, *30*(4), 741–773.

Kong, F., & Schetz, J. (1982). Turbulent boundary layer over porous surfaces with different surface geometries. *20th Aerospace Sciences Meeting*, 30.

Lai, Y.-J. (2020). *Turbulent viscous drag reduction by means of passive flow control - focus on compliant surfaces* (Report).

Lai, Y.-J. (2021). *Turbulent Viscous Drag Reduction in Air by Compliant Surfaces* (Report).

Lee, D., Fahey, D., Skowron, A., Allen, M., Burkhardt, U., Chen, Q., Doherty, S., Freeman, S., Forster, P., Fuglestvedt, J., Gettelman, A., De León, R., Lim, L., Lund, M., Millar, R., Owen, B., Penner, J., Pitari, G., Prather, M., . . . Wilcox, L. (2021). The contribution of global aviation to anthropogenic climate forcing for 2000 to 2018. *Atmospheric Environment*, *244*, 117834. https://doi.org/https://doi.org/10.1016/j.atmosenv.2020.117834

Lockerby, D. (2021). Numerical simulation of boundary-layer control using mems actuation.

Lu, S. S., & Willmarth, W. W. (1973). Measurements of the structure of the reynolds stress in a turbulent boundary layer. *Journal of Fluid Mechanics*, *60*(3), 481–511. https://doi.org/10.1017/S0022112073000315

Martinez-Conde, A., Krenke, T., Frybort, S., & Müller, U. (2017). Review: Comparative analysis of co2 laser and conventional sawing for cutting of lumber and wood-based materials. *Wood Science and Technology*, *51*. https://doi.org/10.1007/s00226-017-0914-9

Nikuradse, J., et al. (1950). Laws of flow in rough pipes.

Oktay, T., & Kanat, Ö. (2017). A review of aerodynamic active flow control.

Panton, R. L., & Miller, J. M. (1975). Excitation of a helmholtz resonator by a turbulent boundary layer. *The Journal of the Acoustical Society of America*, *58*(4), 800–806.

Pearson, B. R., Elavarasan, R., & Antonia, R. A. (1997). The Response of a Turbulent Boundary Layer to a Square Groove. *Journal of Fluids Engineering*, *119*(2), 466–469. https://doi.org/10.1115/1.2819160

Prandtl, L. (1904). Über flussigkeitsbewegung bei sehr kleiner reibung. *Verhandl. III, Internat. Math.-Kong., Heidelberg, Teubner, Leipzig, 1904*, 484–491.

Raffel, M., Willert, C. E., & Kompenhans, J. (1998). *Particle Image Velocimetry: A Practical Guide*. Springer. https://books.google.nl/books?id=enOLTmfYVPQC

Robinson, S. K. (1991). Coherent motions in the turbulent boundary layer. *Annual Review of Fluid Mechanics*, *23*(1), 601–639.

Rodríguez-López, E., Bruce, P. J. K., & Buxton, O. R. H. (2015). A robust post-processing method to determine skin friction in turbulent boundary layers from the velocity profile. *Experiments in Fluids*, *56*. https://doi.org/10.1007/s00348-015-1935-5

Rubio Carpio, A., Avallone, F., Ragni, D., Snellen, M., & van der Zwaag, S. (2020). Quantitative criteria to design optimal permeable trailing edges for noise abatement. *Journal of Sound and Vibration*, *485*, 115596. https://doi.org/https://doi.org/10.1016/j.jsv.2020.115596

Scarano, F. (2013). *Experimental Aerodynamics* (tech. rep.). TU Delft. https://brightspace.tudelft.nl/d2l/le/content/278228/viewContent/1802256/View

Scarano, F., Gojon, R., & Gowree, E. R. (2021). On the development of a turbulent boundary layer over staggered three dimensional cavities. *55th 3AF International Conference on Applied Aerodynamics*, 0.

Scarano, F., Jacob, M. C., Carbonneau, X., & Gowree, E. R. (2022a). Characterisation of bursts in a turbulent boundary layer over circular cavities. *56th 3AF International Conference on Applied Aerodynamics*. https://oatao.univ-toulouse.fr/28991/

Scarano, F., Jacob, M. C., Gojon, R., Carbonneau, X., & Gowree, E. R. (2022b). Modification of a turbulent boundary layer by circular cavities. *Physics of Fluids*, *0*(ja), null. https://doi.org/10.1063/5.0091110

Schlatter, P., & Örlü, R. (2010). Assessment of direct numerical simulation data of turbulent boundary layers. *Journal of Fluid Mechanics*, *659*, 116–126. https://doi.org/10.1017/s0022112010003113

Schlichting, H., & Kestin, J. (1961). *Boundary layer theory* (Vol. 121). Springer.

Sciacchitano, A., & Wieneke, B. (2016). PIV uncertainty propagation. *Measurement Science and Technology*, *27*(8), 084006. https://doi.org/10.1088/0957-0233/27/8/084006

Severino, G. F., Silvestri, A., Cazzolato, B. S., & Arjomandi, M. (2022). Sensitivity analysis of orifice length of micro-cavity array for the purpose of turbulence attenuation. *Experiments in Fluids*, *63*(1), 24. https://doi.org/10.1007/s00348-021-03371-9

Silvestri, A. (2018). *The attenuation of sweep events within the turbulent boundary layer over a flat plate using a micro-cavity array* (Doctoral dissertation).

Silvestri, A., Ghanadi, F., Arjomandi, M., Cazzolato, B., & Zander, A. (2017a). Attenuation of sweep events in a turbulent boundary layer using micro-cavities. *Experiments in Fluids*, *58*(5). https://doi.org/10.1007/s00348-017-2345-7

Silvestri, A., Ghanadi, F., Arjomandi, M., Cazzolato, B., Zander, A., & Chin, R. (2018). Mechanism of sweep event attenuation using micro-cavities in a turbulent boundary layer. *Physics of Fluids*, *30*(5). https://doi.org/https://doi.org/10.1063/1.5026130

Silvestri, A., Ghanadi, F., Arjomandi, M., Chin, R., Cazzolato, B., & Zander, A. (2017b). Attenuation of turbulence by the passive control of sweep events in a turbulent boundary layer using micro-cavities. *Physics of Fluids*, *29*(11), 115102. https://doi.org/10.1063/1.4995466

Spangler, J. G. (1966). *Effects of periodic blowing through flush transverse slots on turbulent boundary layer skin friction* (tech. rep.).

Sutardi & Ching, C. (1999). Effect of a transverse square groove on a turbulent boundary layer. *Experimental Thermal and Fluid Science*, *20*(1), 1–10. https://doi.org/https://doi.org/10.1016/S0894-1777(99)00031-X

Tani, I., Munakata, H., Matsumoto, A., & Abe, K. (1988). Turbulence management by groove roughness. In H. W. Liepmann & R. Narasimha (Eds.), *Turbulence management and relaminarisation* (pp. 161–172). Springer Berlin Heidelberg.

Taylor, G. I. (1938). The spectrum of turbulence. *Proceedings of the Royal Society of London. Series A-Mathematical and Physical Sciences*, *164*(919), 476–490.

van Nesselrooij, M., Veldhuis, L., van Oudheusden, B., & Schrijer, F. (2016). Drag reduction by means of dimpled surfaces in turbulent boundary layers. *Experiments in Fluids: experimental methods and their applications to fluid flow*, *57*.

van Nesselrooij, M., van Campenhout, O. W. G., van Oudheusden, B. W., Schrijer, F. F. J., & Veldhuis, L. L. M. (2022). Development of an experimental apparatus for flat plate drag measurements and considerations for such measurements. *Measurement Science and Technology*, *33*(5), 055303. https://doi.org/10.1088/1361-6501/ac527f

Wahidi, R., Chakroun, W., & Al-Fahed, S. (2005). The behavior of the skin-friction coefficient of a turbulent boundary layer flow over a flat plate with differently configured transverse square grooves. *Experimental Thermal and Fluid Science*, *30*(2), 141–152. https://doi.org/https://doi.org/10.1016/j.expthermflusci.2005.03.022

Wallace, J. M., Eckelmann, H., & Brodkey, R. S. (1972). The wall region in turbulent shear flow. *Journal of Fluid Mechanics*, *54*(1), 39–48.

Whalley, R. D. (2011). *Turbulent boundary-layer control with dbd plasma actuators using spanwise travelling-wave technique* (Doctoral dissertation). University of Nottingham.

White, F. (2006). *Viscous fluid flow*. McGraw-Hill. https://books.google.nl/books?id=fl6wPwAACAAJ

Wilkinson, S. P. (1983). Influence of wall permeability on turbulent boundary-layer properties. *AlAA 21 st Aerospace Sciences Meeting*.

Wolter, J. (2005). Drag measurements of porous plate acoustic liners. *43rd AIAA Aerospace Sciences Meeting and Exhibit*, 803.

Appendices

A

Direct force measurements: Additional results

The data supporting the estimation of ΔC_D like drag coefficient values, null force and pressure drag corrections and uncertainty of ΔC_D in a measurement set are presented in this appendix.

New pore designs: Pore size and configuration

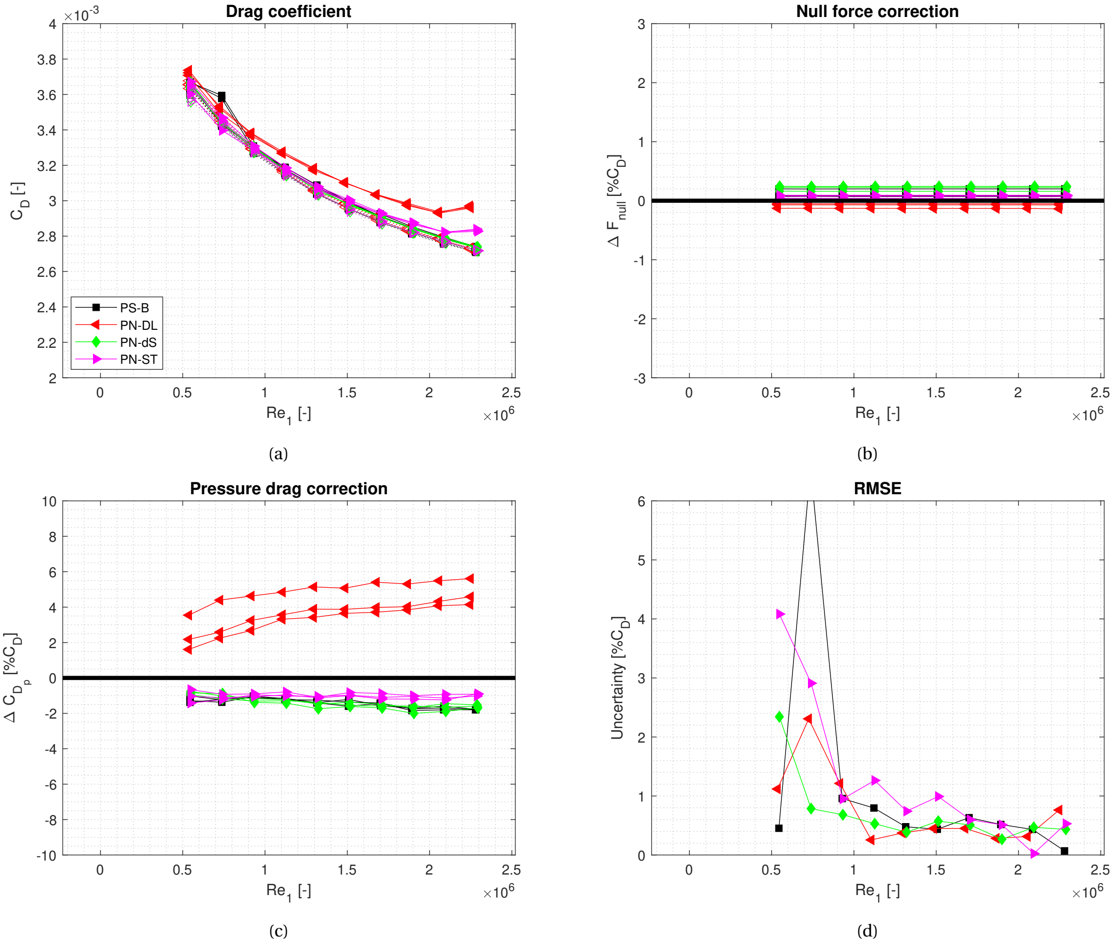

(a)

(b)

(c)

(d)

Figure A.1: Drag measurement results for the new pore designs, pore size and configuration (a) Drag coefficient, dotted lines: smooth reference plate (b) Null force shift corrections (c) Gap pressure drag corrections (d) Uncertainty of measurement set determined as RMSE

New pore designs: Pore spacing

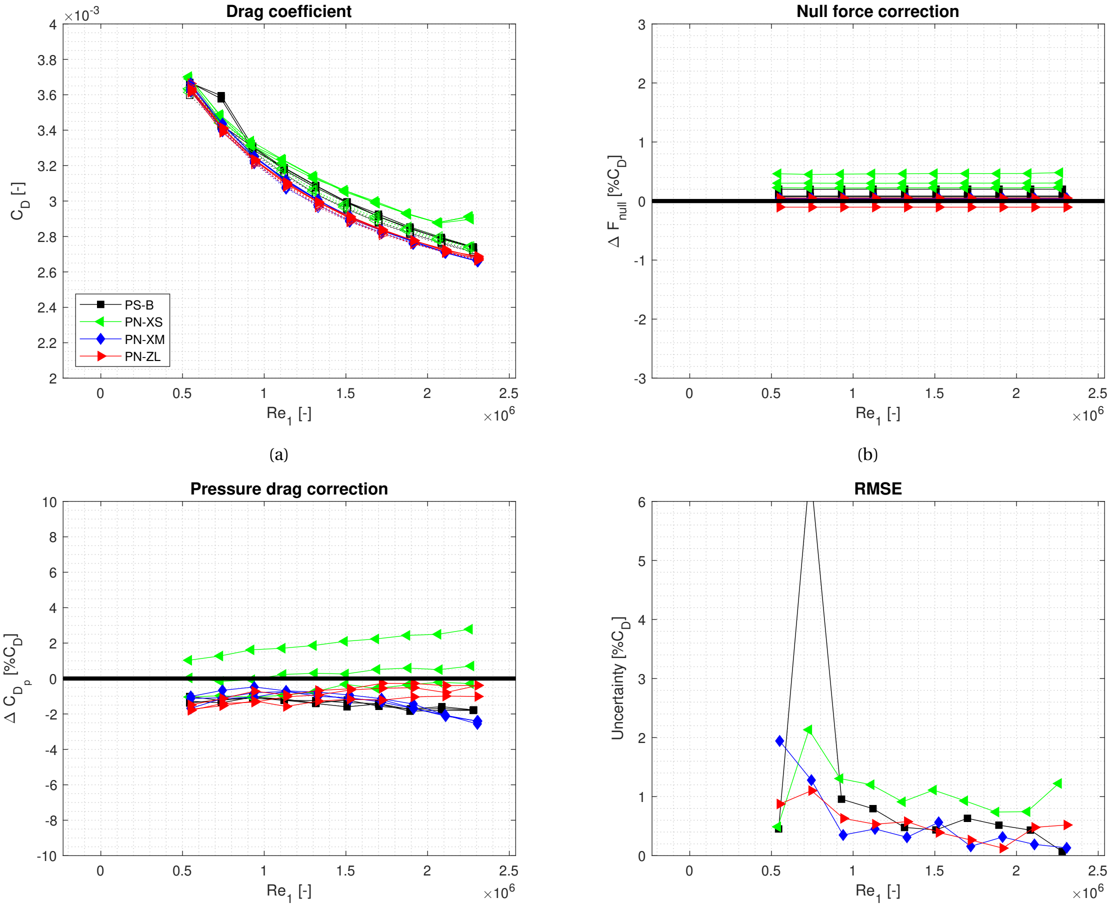

(a) (b)

(c) (d)

Figure A.2: Drag measurement results for the new pore designs, pore spacing (a) Drag coefficient, dotted lines: smooth reference plate (b) Null force shift corrections (c) Gap pressure drag corrections (d) Uncertainty of measurement set determined as RMSE

New backing cavity designs

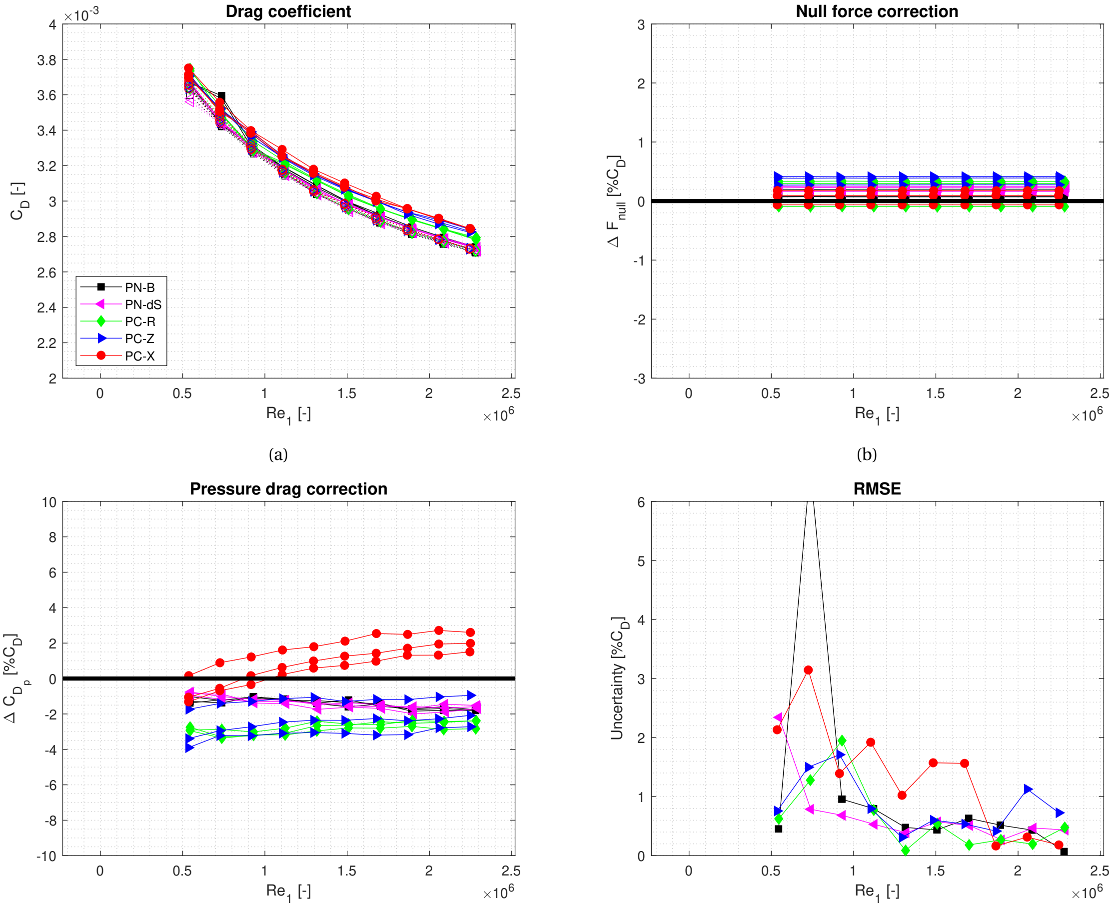

(a) (b)

(c) (d)

Figure A.3: Drag measurement results for the new backing cavity designs (a) Drag coefficient, dotted lines: smooth reference plate (b) Null force shift corrections (c) Gap pressure drag corrections (d) Uncertainty of measurement set determined as RMSE

Permeable trailing edge designs

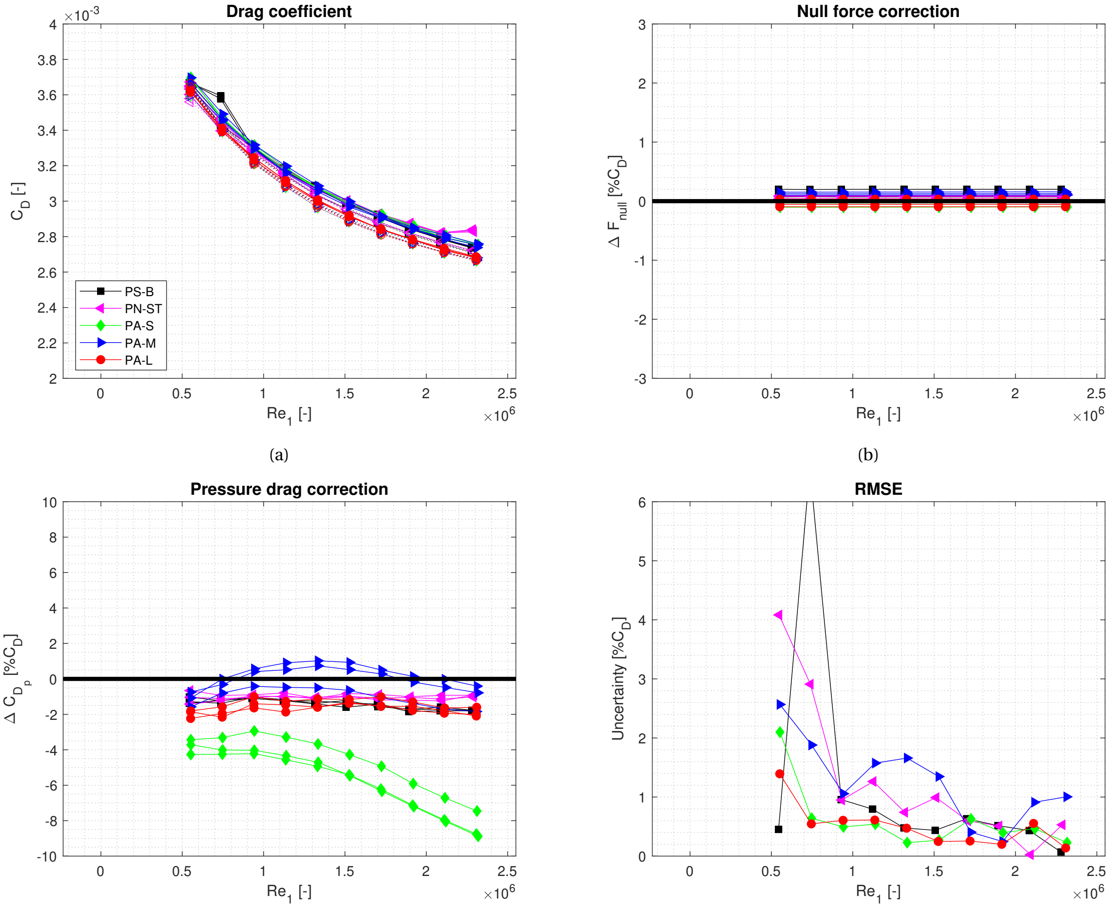

(a) (b)

(c) (d)

Figure A.4: Drag measurement results for the permeable trailing edge designs (a) Drag coefficient, dotted lines: smooth reference plate (b) Null force shift corrections (c) Gap pressure drag corrections (d) Uncertainty of measurement set determined as RMSE

New groove designs

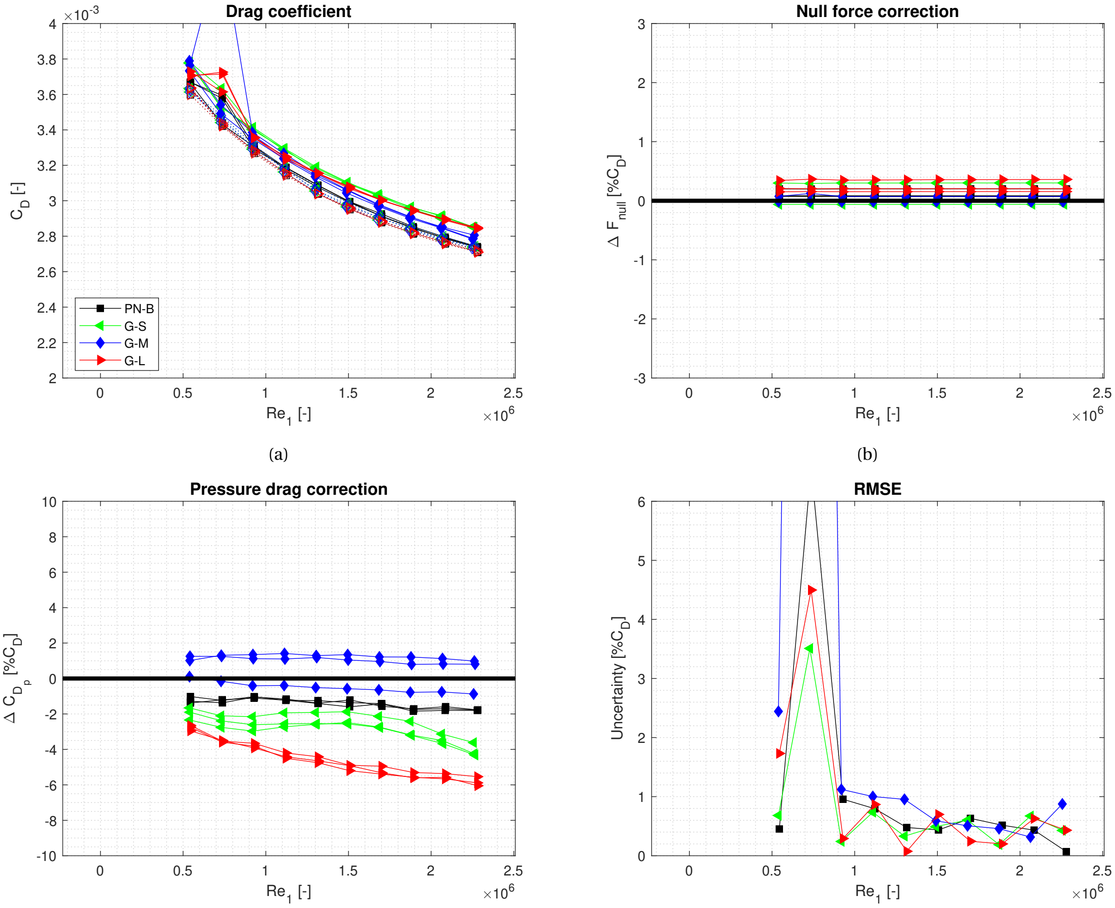

(a) (b)

(c) (d)

Figure A.5: Drag measurement results for the new groove designs (a) Drag coefficient, dotted lines: smooth reference plate (b) Null force shift corrections (c) Gap pressure drag corrections (d) Uncertainty of measurement set determined as RMSE

B

Cross-correlation analysis

This appendix presents the test cases and results of the PIV cross-correlation analysis. The interrogation window settings corresponding to each case are listed in Table B.1. It was observed that larger windows resulted in blurred velocity fields due to the low detail and smaller window sizes caused grainy images due to noise. The test case "a" was deemed the best and was used for processing all the measurement sets.

Table B.1: Interrogation window settings in the cross-correlation analysis

	Initial pass		**Final pass**	
Case	**Size** (pixels)	**Shape**	**Size** (pixels)	**Shape**
a	96 × 96	elliptical, 2:1	16 × 16	elliptical, 2:1
b	96 × 96	elliptical, 2:1	12 × 12	elliptical, 2:1
c	96 × 96	elliptical, 2:1	24 × 24	elliptical, 2:1
d	96 × 96	square	16 × 16	square
e	96 × 96	circle	16 × 16	circle

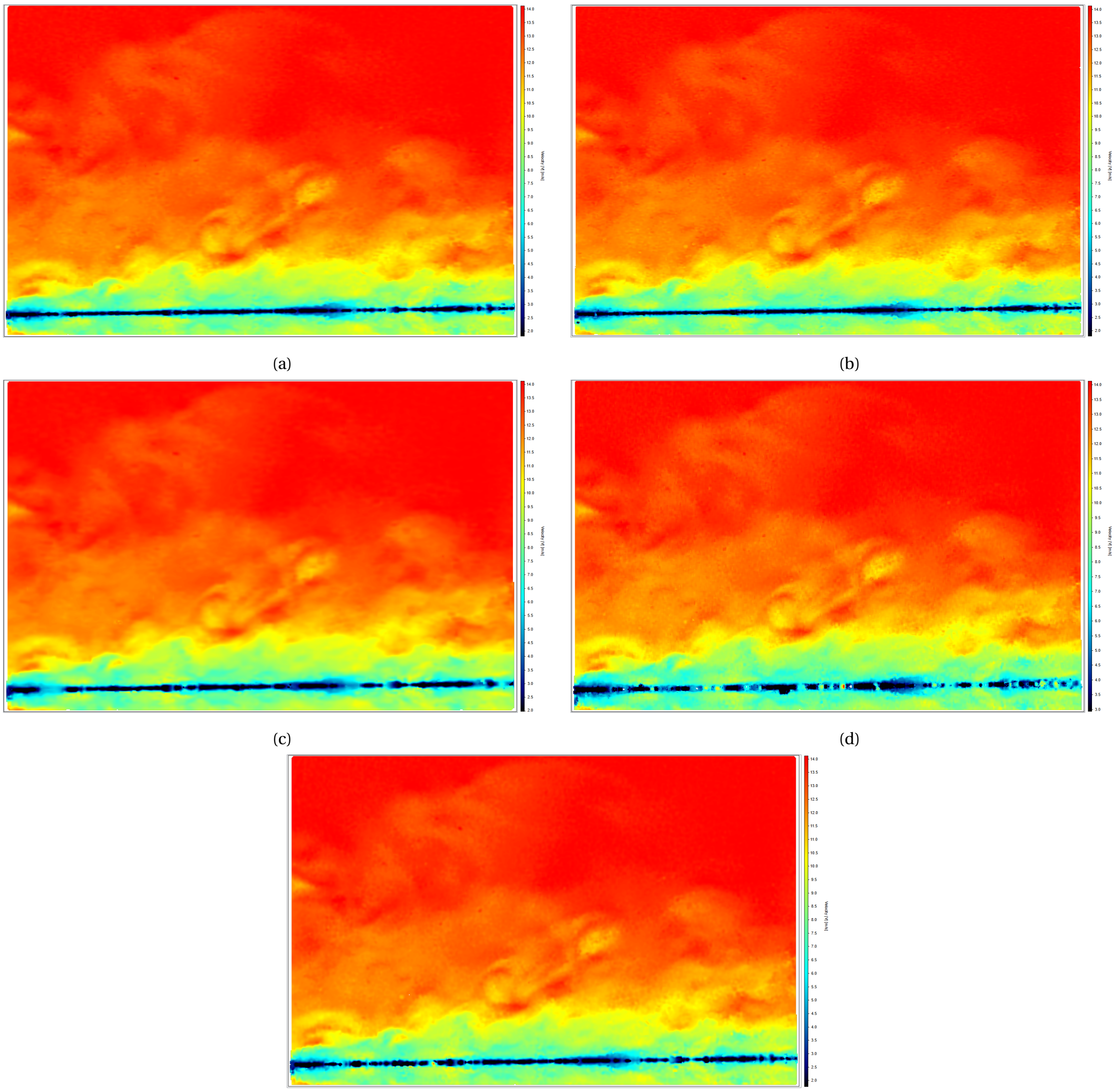

(a)

(b)

(c)

(d)

(e)

Figure B.1: Results of the cross-correlation analysis for the interrogation window settings listed in Table B.1, instantaneous velocity fields

C

PIV results

This appendix presents the PIV results of some designs. This includes the boundary layer profiles of mean velocity, streamwise and wall-normal fluctuations and Reynolds stress. The boundary layer profiles of each design are compared with the smooth reference and DNS data by Schlatter and Örlü (2010). The DNS data is included to validate the measured results.

PN-XS design

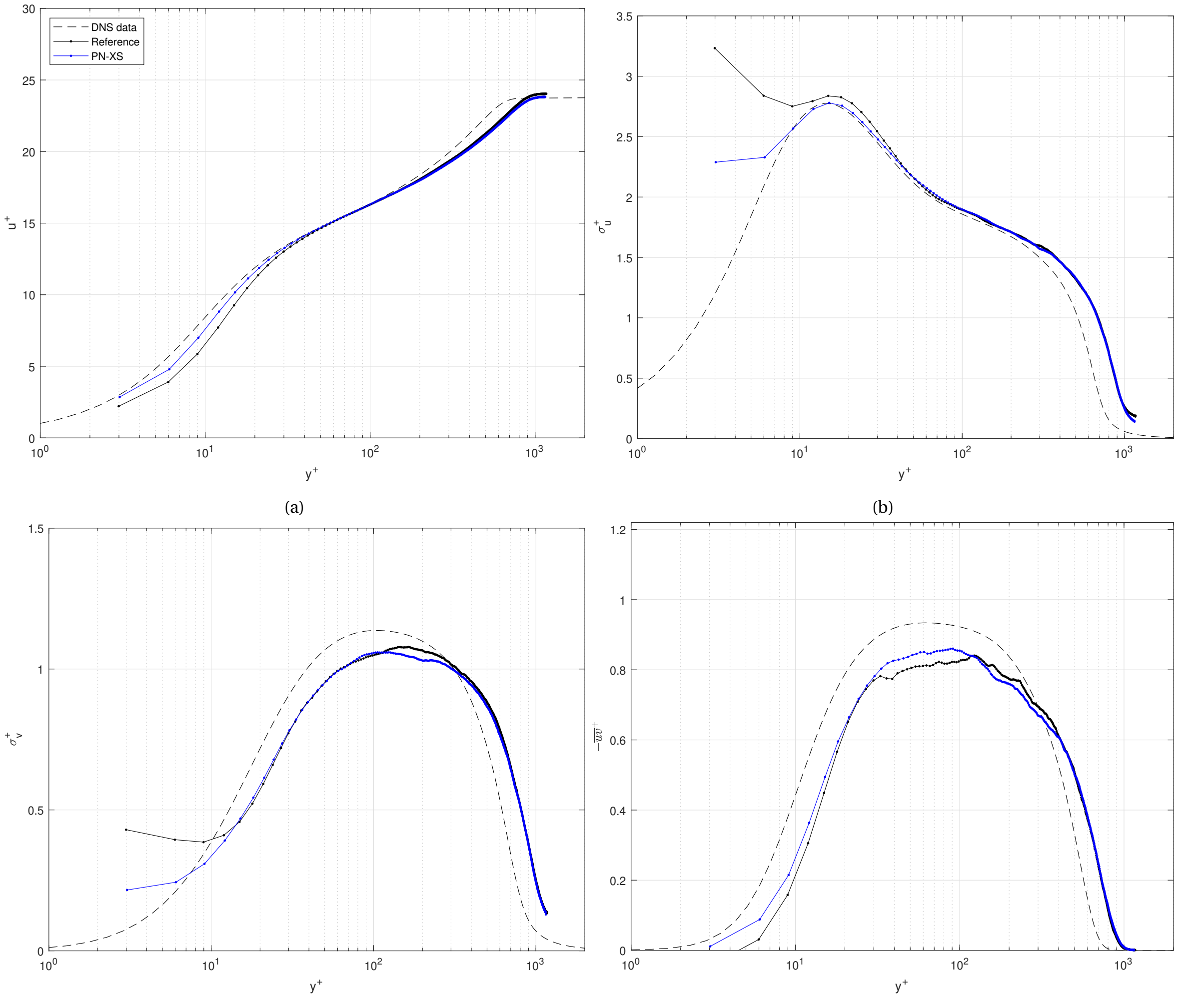

(a) (b) (c) (d)

Figure C.1: Boundary layer profiles of PN-XS design and smooth reference (a) Mean velocity (u^+). (b) Streamwise velocity fluctuations (σ_u^+). (c) Wall-normal velocity fluctuations (σ_v^+). (d) Reynolds stress ($-\overline{uv}^+$)

PN-DL design

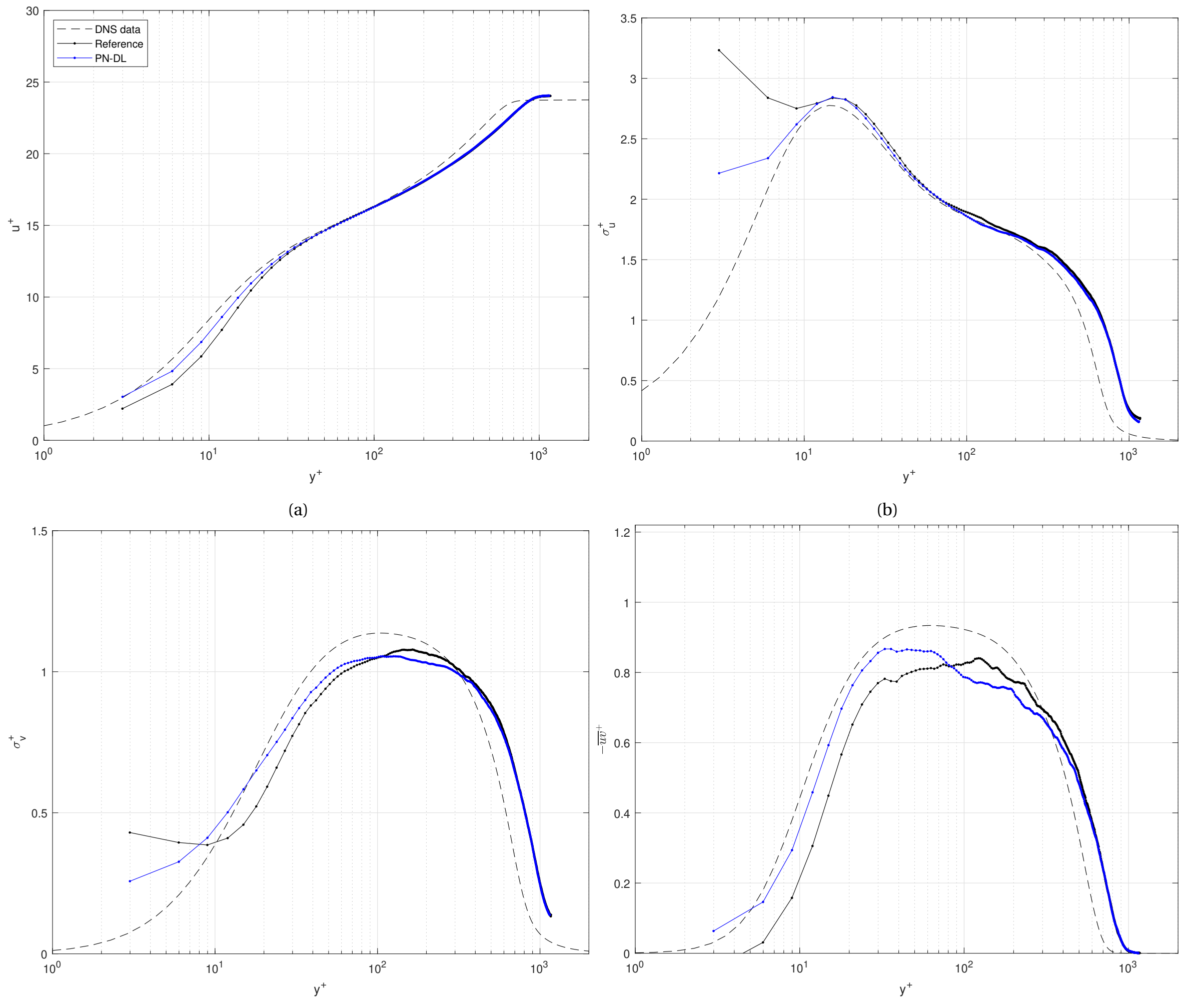

(a) (b)

(c) (d)

Figure C.2: Boundary layer profiles of PN-DL design and smooth reference (a) Mean velocity (u^+). (b) Streamwise velocity fluctuations (σ_u^+). (c) Wall-normal velocity fluctuations (σ_v^+). (d) Reynolds stress ($-\overline{uv}^+$)

G-S design

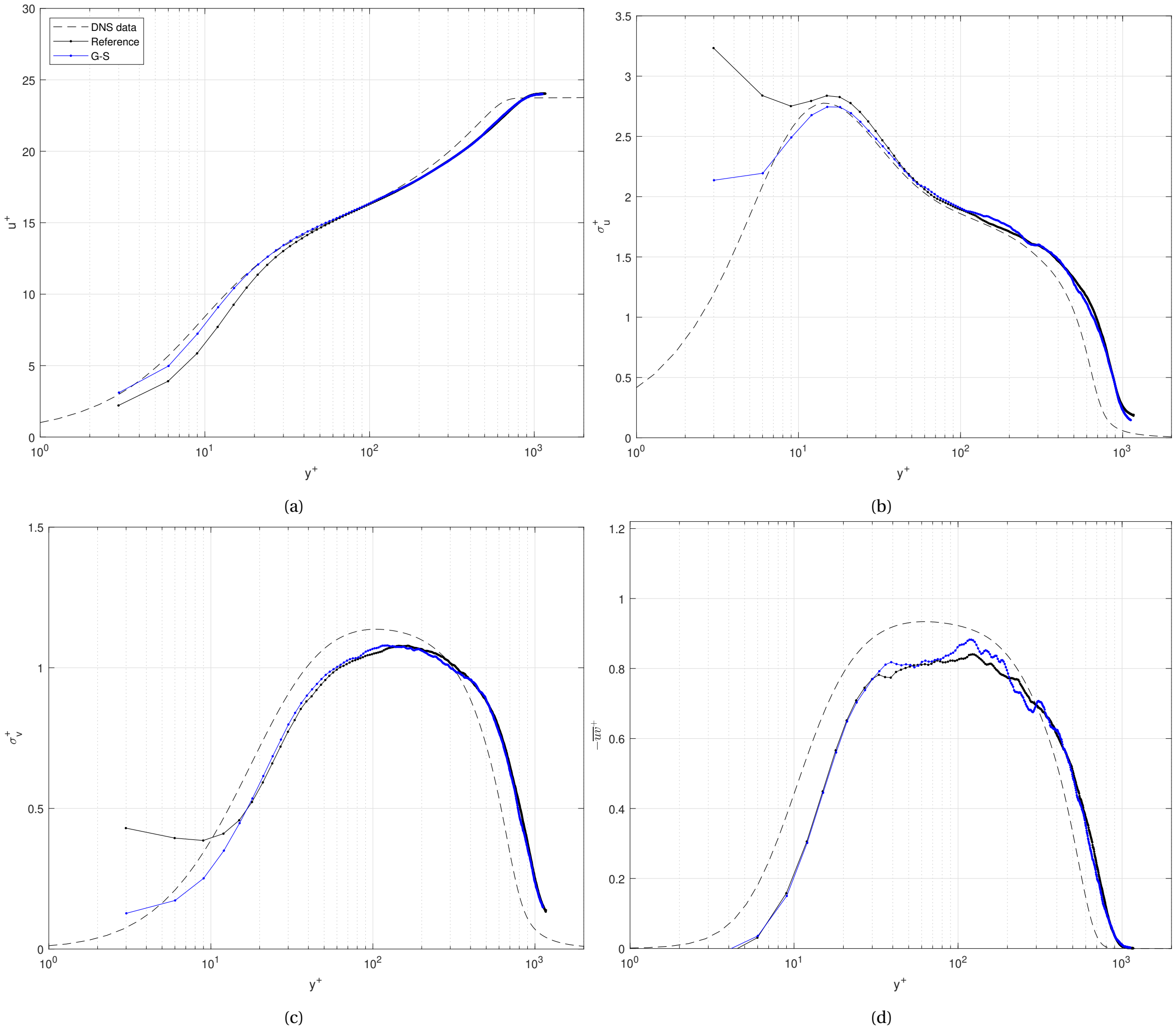

Figure C.3: Boundary layer profiles of G-S design and smooth reference (a) Mean velocity (u^+). (b) Streamwise velocity fluctuations (σ_u^+). (c) Wall-normal velocity fluctuations (σ_v^+). (d) Reynolds stress ($-\overline{uv}^+$)

TU Delft

DIMPLE